

Department of Physics and Astronomy

University of Heidelberg

Diploma thesis

in Physics

submitted by

Florian Lauer

born in Freudenstadt

February 2011



**Investigations**  
**of a fluorescent nuclear track detector**  
**for use in**  
**therapeutic ion beams**

This diploma thesis has been carried out by Florian Lauer

at the

German Cancer Research Center (DKFZ)

under the supervision of

Prof. Dr. rer. nat. Oliver Jäkel

and

Prof. Dr. rer. nat. Uwe Oelfke

## **Zusammenfassung:**

Mit Fluoreszenzkernspurdetektoren (FKSD) auf der Basis von  $\text{Al}_2\text{O}_3\text{:C,Mg}$ -Einkristallen steht der Hadronentherapie eine neuartige Technologie zur Verfügung, um hochaufgelöst Teilchenfluenz zu bestimmen und Aussagen über die Strahlqualität zu treffen. Fluoreszenz (750 nm) von Fehlstellenkomplexen, proportional zur lokalen Energiedosis, wird hierbei mittels konfokaler Laser-mikroskopie erfasst. Die Aufgabenstellung dieser Arbeit war die Integration von FKSD-Technologie in ein Medizinforschungsumfeld, weshalb erstmalig das Auslesen mittels eines kommerziellen Konfokal-Lasermikroskops (Zeiss LSM 710) – statt des speziell angefertigten Aufbaus der Herstellerfirma (Landauer, Inc., USA) – durchgeführt und standardisiert wurde. Auf Grund örtlicher Schwankungen (15–20 %) der Mikroskopempfindlichkeit wurde ein Korrekturprotokoll für die angestrebten quantitativen Messungen etabliert. Ein Sättigungseffekt konnte hierbei für Gammastrahlung bis 20 Gy in Wasser nicht beobachtet werden. Die Empfindlichkeit der Methode wurde bis hin zum Nachweis einzelner Sekundärelektronenspuren (270 MeV/u C-12) demonstriert. Zudem konnten Unterschiede im Projektilfragmentspektrum lateral einer 270 MeV/u Kohlenstoffion-Strahlachse aufgelöst werden. Messungen der radialen Bahnspur-Fluoreszenzverteilungen zeigten die durch Beugungsgrenze und Sättigungseffekte zu erwartenden Beschränkungen. Trotz der exzellenten Sensitivität ergaben Fluenzmessungen mit Hilfe automatischer Zählroutinen für Protonen und Kohlenstoffionen Abweichungen von bis zu 11.7 % vom Erwartungswert. Machbarkeitsstudien zur Messung der Strahlqualität wurden durchgeführt und der Einfluss unterschiedlicher Geometrien auf die Neutronenfluenz im Strahlhalo konnte festgestellt werden.

## **Abstract:**

Fluorescent nuclear track detectors (FNTD) based on  $\text{Al}_2\text{O}_3\text{:C,Mg}$  single crystals are a novel technology for high spatial resolution fluence determination and radiation quality monitoring in hadron therapy. 750 nm fluorescence from lattice defect clusters proportional to the absorbed dose is detected by confocal laser scanning microscopy. The task of this thesis was the integration of FNTD technology into a medical research environment. Therefore, the first step was to investigate FNTD readout—previously only reported for the manufacturer's (Landauer, Inc. USA) dedicated system—with a commercial confocal laser scanning microscope (Zeiss LSM 710). In order to enable quantitative measurements, a correction protocol was established to account for spatial variations of the microscope sensitivity (15–20 %). Using this, no saturation effects for 20 Gy gamma irradiation was observed. Sensitivity was demonstrated by even imaging single secondary electron tracks for 270 MeV/u C-12 and sufficient resolution of changes in the projectile fragment spectra lateral to the beam axis was shown. Boundary conditions imposed by diffraction and possible saturation effects were demonstrated for a radial track profile measurement. In spite of the excellent sensitivity, fluence measurements for protons and carbon ions using automatic track counting still yielded up to 11.7 % deviation from the expectation value. Feasibility studies on radiation quality monitoring were conducted and the influence of the setup geometry on neutron fluence in the beam halo could be detected.



*Da hat man was eigenes.*  
— EVELYN HAMANN (1942 – 2007)



# Contents

<b>1</b>	<b>Introduction</b>	<b>1</b>
<b>2</b>	<b>Theory</b>	<b>5</b>
2.1	Dosimetric concepts . . . . .	5
2.1.1	Radiation, particle radiation, ionizing radiation . . . . .	5
2.1.2	Fluence . . . . .	6
2.1.3	Physical dose . . . . .	6
2.1.4	Linear energy transfer - LET . . . . .	9
2.1.5	Fragmentation and neutron production . . . . .	10
2.1.6	Beam quality . . . . .	11
2.2	Confocal microscopy . . . . .	12
<b>3</b>	<b>Methods &amp; Materials</b>	<b>15</b>
3.1	Al <sub>2</sub> O <sub>3</sub> :C,Mg . . . . .	15
3.1.1	Crystal lattice structure of $\alpha$ -Al <sub>2</sub> O <sub>3</sub> :C,Mg . . . . .	15
3.1.2	The $F_2^{2+}(2\text{Mg})$ cluster defect . . . . .	16
3.1.3	Radiochromic transformation . . . . .	16
3.1.4	Excitation/emission spectra of Al <sub>2</sub> O <sub>3</sub> :C,Mg . . . . .	17
3.2	Irradiation . . . . .	20
3.2.1	Siemens Gammatron S . . . . .	20
3.2.2	Siemens Primus . . . . .	20
3.2.3	Sr/Y-90 source . . . . .	20
3.2.4	Am-241 source . . . . .	20
3.2.5	Heidelberg Ion-beam Therapy center (HIT) . . . . .	21
3.2.6	AD-4/ACE . . . . .	21
3.3	Microscopy . . . . .	22
3.3.1	Zeiss LSM 710 Confocor 3 . . . . .	22
3.3.2	Auxiliary tools . . . . .	22
3.4	Data processing . . . . .	23
<b>4</b>	<b>Experiments &amp; Results</b>	<b>25</b>
4.1	Microscope settings . . . . .	25
4.2	Sources of variation of the APD reading . . . . .	26
4.2.1	Photon shot noise . . . . .	26
4.2.2	Relative density of F-center clusters . . . . .	26
4.2.3	Ethanol bubbles in immersion oil . . . . .	28

4.2.4	Doping inhomogeneities . . . . .	28
4.2.5	Environmental radiation . . . . .	30
4.2.6	Fluorescent cleaning residues . . . . .	30
4.2.7	Dust . . . . .	30
4.2.8	Microscope sensitivity . . . . .	31
4.3	Background . . . . .	31
4.3.1	Nature of the background signal . . . . .	33
4.3.2	Behavior of the background signal . . . . .	34
4.3.3	Signal correction . . . . .	36
4.4	Response to gamma radiation . . . . .	43
4.4.1	Setup . . . . .	43
4.4.2	Results . . . . .	44
4.5	Imaging of particle tracks . . . . .	47
4.5.1	Beta particles . . . . .	47
4.5.2	Alpha particles . . . . .	47
4.5.3	Carbon ions . . . . .	49
4.5.4	Protons . . . . .	52
4.5.5	Antiprotons . . . . .	53
4.6	Lateral beam quality change . . . . .	55
4.6.1	Setup: lateral beam quality change . . . . .	55
4.6.2	Results: lateral beam quality change . . . . .	57
4.7	Radial track profile . . . . .	57
4.8	Fluence measurements . . . . .	60
4.8.1	Setup: fluence measurements . . . . .	60
4.8.2	Results: fluence measurements . . . . .	60
4.9	Beam quality measurement by fluorescence frequency distribution . . . . .	61
4.10	Neutron measurements . . . . .	63
4.10.1	Setup: neutron measurements . . . . .	66
4.10.2	Results: neutron measurements . . . . .	66
<b>5</b>	<b>Discussion &amp; Outlook</b>	<b>67</b>
5.1	Literature review . . . . .	67
5.2	Background . . . . .	68
5.2.1	Nature of the background signal . . . . .	68
5.2.2	Behavior of the background signal . . . . .	68
5.2.3	Signal correction . . . . .	68
5.3	Response to gamma radiation . . . . .	69
5.4	Imaging of particle tracks . . . . .	69
5.5	Lateral beam quality change . . . . .	70
5.6	Radial track profiles . . . . .	70
5.7	Fluence measurements . . . . .	70
5.8	Beam quality measurement by fluorescence frequency distribution . . . . .	71
5.9	Neutron measurements . . . . .	72
5.10	Summary and suggestions for further investigations . . . . .	72

<b>I</b>	<b>Appendix</b>	<b>75</b>
<b>A</b>	<b>List of Experiments</b>	<b>77</b>
<b>B</b>	<b>Lists</b>	<b>81</b>
	B.1 List of Figures . . . . .	81
	B.2 List of Tables . . . . .	83
<b>C</b>	<b>Bibliography</b>	<b>85</b>



# Chapter 1

## Introduction

Besides medical oncology and surgery, radiation oncology is one of the pillars of the treatment of cancer. Especially patients with located, inoperable tumors benefit from radiotherapy. The rationale behind radiotherapy is to use the energy deposition of ionizing radiation for the inactivation of tumor cells. This is primarily achieved when the genetic code in the cell nucleus is damaged beyond repair by the destruction of atomic bonds in ionizations.

Over the last decades, the benefits of external radiotherapy with heavy charged particles (HCPs) such as protons or carbon ions were explored. In contrast to photons commonly used, HCPs traversing matter continuously slow down due to momentum transfers. This yields a so-called *inverse dose profile* (Figure 1.1) as the energy deposition per unit length increases with decreasing velocity.

Besides the maximum energy deposition being at the end of the particle trajectory, the sharply defined range is an asset for hadron therapy. Thereby enabling superior dose conformation to the target volume and sparing of the surrounding healthy tissue, it is anticipated to be particularly suited for the treatment of deep-seated tumors in the vicinity of organs-at-risk.

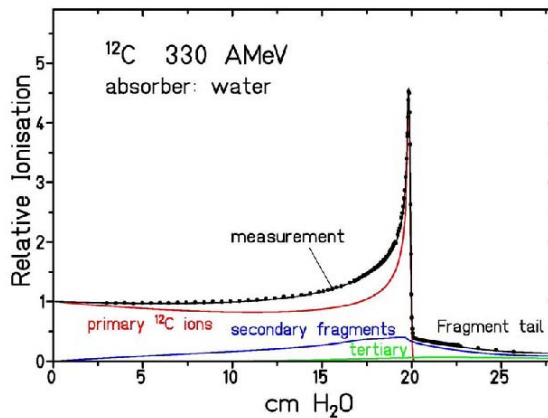


Figure 1.1: Depth dose curve of a 270 MeV/u carbon ion beam (black), relative to the entrance dose. Contribution of the primary HCP is red, respectively blue for secondary fragments (Schardt 2009)

However, when traversing matter, HCPs can undergo nuclear reactions (Figure 1.1). Two major issues caused hereof in therapy beams is the production of fast neutrons (Gunzert-Marx et al. 2004) and the accumulation of projectile fragments in the beam (Haettner 2006).

Even if the neutron contribution to the total energy deposition is small, it is unfavorable because neutrons are radiobiologically highly effective and are known to cause severe side effects. Unfortunately, neutron dosimetry is a challenge not manageable with ordinary ion dosimetry technology such as ionization chambers or diodes.

Projectile fragments, on the other hand, have a larger penetration depth than the primary HCPs and show an increase in lateral scattering. Thus, they can compromise dose conformity, especially as they tend to exhibit an enhanced radiobiological effectiveness as well. At the same time, fragmentation yields mixed particle fields whose composition has to be known in order to predict the radiobiological effect in treatment planning systems. It is, therefore, highly desirable to have an instrument to quantify the abundance of fragments and neutrons in clinical beams while allowing identification of different particle types.

Especially nuclear track detectors (Fleischer et al. 1965) made of plastics like CR-39 (Cartwright et al. 1978) and LR-115 (Benton 1968) have been used to estimate neutron dose. Track detectors (for neutrons equipped with radiators) do not measure dose, but detect the number of particle traversals per area, preferably with the additional ability to discriminate between tracks of different particle type, i.e. spectroscopy.

Even though plastic nuclear track detectors (PNTDs) combine fluence detection with spectroscopic capabilities (Fews and Henshaw 1982), their use in hadron therapy is hampered by the need for extensive etching and their non-reusability after the etching.

Therefore, the possible use of novel fluorescent nuclear track detector (FNTD) technology was investigated in this thesis.

Introduced as volumetric optical data storage medium in 2003 (Akselrod et al. 2003),  $\text{Al}_2\text{O}_3:\text{C,Mg}$  was soon proposed as track detector for HCPs (Akselrod et al. 2006a).

In contrast to optically stimulated luminescence (OSL) dosimetry where light is emitted in electron-hole recombinations, FNTD read-out technology is based on the fluorescence from the deexcitation of electrons in elevated intra-defect (i.e. non-continuum) energy levels. Recombination-free fluorescence allows for multiple read-outs without bleaching (Sykora et al. 2008b). Because the deexcitation after stimulation with 620 nm light takes  $75 \pm 5$  ns (Akselrod and Akselrod 2006)—in contrast to lifetimes in the order of  $10^{-2}$  s even in “prompt”, pulsed OSL (POSL, see Akselrod et al. (1998))—read-out can be performed using a confocal laser scanning microscope.

Up to now, processing of FNTDs was limited to a dedicated laser scanning system, available only to the FNTDs’ manufacturer. To enable a reasonable workflow



in a life science environment, the first task of this thesis was to investigate the reading capabilities of and to establish a read-out protocol for a commercial confocal laser scanning microscope allowing on-site measurements. With read-out parameter settings optimized (section 4.1), the detector reading had to be investigated and characterized (section 4.2). From this, a correction procedure for inhomogeneities and background was derived (section 4.3). Then, the response of FNTDs to gamma radiation was characterized (section 4.4).

Qualitative analysis of particle track imaging capabilities was conducted in first ion beam measurements, using grazing tracks of carbon ions and antiprotons (section 4.5). Subsequently, the resolution of the radiation quality change lateral from the beam axis was investigated (section 4.6). To show the limits imposed by diffraction and saturation, a carbon ion radial track profile was quantitatively evaluated in section 4.7. Fluence measurements were conducted in order to give an estimation of the track counting efficiency (section 4.8). In a first spectroscopic measurement, the signal distribution of particle radiation was investigated in section 4.9. The impact of setup geometry in off-beam neutron experiments was studied in section 4.10.

Fundamental concepts and quantities with relevance to the measurements conducted are described in section 2.1. Read-out of irradiated FNTDs is done by the application of confocal microscopy (section 2.2) to the radiation sensitive material  $\text{Al}_2\text{O}_3:\text{C,Mg}$  (section 3.1). Irradiated at different facilities (section 3.2) FNTDs were read-out using a Zeiss LSM 710 (section 3.3). After data acquisition, processing tools were applied (section 3.4). Experimental setups and the obtained results are given in chapter 4. Findings are summarized and discussed in chapter 5.



# Chapter 2

## Theory

This chapter explaining the theoretical background is divided into two major parts. Section 2.1 introduces concepts and notations in dosimetry relevant for this thesis. The role of section 2.2 is to introduce into the theoretical basis of confocal microscopy which is the technology necessary for FNTD read-out.

### 2.1 Dosimetric concepts

Dosimetry is the science of measuring (ancient greek: μέτρον) quantities transferred (ancient greek for donation, gift: δόσις) by radiation. This section explains what radiation is (subsection 2.1.1) and introduces fundamental dosimetric quantities: Fluence (subsection 2.1.2) is necessary to quantify the density of particle tracks, dose (subsection 2.1.3) is the fundamental measure of the absorbed energy. The concept of LET (subsection 2.1.4) is a measure for the local energy deposition of a particle, enabling differentiation of different beam qualities. With increasing penetration depth, HCP beams change their quality not only via LET but also via particle spectrum alterations due to fragmentations. Therefore, the problem of fragmentation is outlined in subsection 2.1.5. The fragmentation process of target nuclei hit by an antiproton is explained in an extra paragraph.

Of clinical importance is the radiobiological outcome of different beam qualities (subsection 2.1.6), usually quantified with the relative biological effectiveness (RBE). This concept is fundamental for the motivation to investigate detector response to radiation of different beam qualities.

#### 2.1.1 Radiation, particle radiation, ionizing radiation

In general, *radiation* is transport of energy and/or mass where the transport is not bound to a medium (as e.g. is the case for diffusion). Although in certain situations photon quanta may behave as particles, the terminology of this thesis reserves the term “particle” to corpuscular, i.e. massive, carriers of energy. Radiation that deposits locally enough energy to ionize traversed matter such as in radiotherapy, is called *ionizing radiation*.

In radiation therapy, tumor cell inactivation is primarily achieved by destruction of the deoxyribonucleic acid (DNA) in the cell nucleus, where the genetic information

is encoded. Breaking of atomic bonds is done directly by ionization of the DNA or indirectly by radiation-induced radicals. In particle therapy, direct ionization is outranking the indirect radiochemical process where radiolyzed water molecules oxidate the DNA.

### 2.1.2 Fluence

The International Commission on Radiation Units and Measurements (ICRU) defines the particle *fluence*  $\Phi$  at a point  $\vec{r}$  in (ICRU 1998) as the number  $dN$  of incident particles on an infinitesimal sphere around  $\vec{r}$  with cross-sectional area  $dA_{\perp}$ :

$$\Phi(\vec{r}) = \frac{dN}{dA_{\perp}} \left[ \frac{1}{\text{cm}^2} \right]$$

In hadron therapy, the fluence of a particle beam is simplified due to the unidirectionality of the beam particles. Under these conditions, fluence also denotes the mean fluence of particles penetrating a finite area and is usually given in  $\text{cm}^{-2}$ .

### 2.1.3 Physical dose

*Physical dose* or *absorbed dose* is defined (ICRU 1998) as the mean energy imparted  $d\bar{\epsilon}$  by ionizing radiation to a certain volume  $dV$  divided by the mass  $dm$  of the matter contained within the volume:

$$D = \frac{d\bar{\epsilon}}{dm} \left[ \frac{\text{J}}{\text{kg}} = \text{Gy} \right]$$

While the energy imparted  $\epsilon$  and the specific energy  $z = \frac{\epsilon}{m}$  are stochastic quantities,  $\bar{\epsilon}$  and  $D = \lim_{m \rightarrow 0} \frac{\bar{\epsilon}}{m} = \frac{d\bar{\epsilon}}{dm}$  are not. Originally, taking the mean of  $\epsilon$  or  $z$  was meant to be in the probability distribution domain for a certain macroscopic absorbed dose. To avoid this circular definition, one can also comprehend the averaging in the spatial domain: this way, one can have volume elements that are large enough to speak usefully of a medium i.e. neglecting structures of subatomic, atomic or molecular lengthscale.

In particular, the concept of dose as used in clinical contexts comprises a typical volume such that one can reasonably speak of secondary electron equilibrium or in-equilibrium (about  $1 \text{ mm}^3$ ). On the contrary, the typical volume of microdosimetry is  $1 \text{ }\mu\text{m}^3$ . FNTD read-out is diffraction-limited (discussed *en détail* in section 2.2), hence allowing for sub-micrometer resolved dose-effect detection.

### Dose deposition of particle radiation

Directly ionizing heavy charged particle radiation of clinical energies (from 30 MeV for protons in eye cancer treatment up to 430 MeV per nucleon carbon ions for deep

seated tumors) imparts energy to the irradiated medium by exciting and ionizing the medium's atoms. Several mechanisms play a role in the energy transfer, inelastic collisions with electrons being the most important one. Charged particles traversing a medium exert Coulomb forces to the electrons, thus releasing kinetic energy. This energy transfer is at the cost of the primary particle which slows down in consequence.

A charged particle's slowing down due to collisions with electrons is described by the Bethe formula (Bethe 1930, 1932). It calculates quantum mechanically the electronic stopping power  $S(E)^{electr.} = -\frac{dE}{dx}$  in a homogeneous medium in first-order Born approximation. While the electron density of the medium enters the equation linearly, the relative velocity  $\beta = v/c$  enters  $\approx \beta^{-2}$  which means an increasing energy loss during slowing down named Bragg curve (see Figure 1.1). Its maximum is called the Bragg peak. The primary particle's charge enters in a squared fashion as well. Neglecting effects of mass defect, particles with the same kinetic energy per nucleon exhibit the same velocity. This means that fragments with different  $Z^2/A$  ratios exhibit another stopping power function than the primary particle and hence a change of range, which can be easily seen from the integral

$$R_{CSDA} = \int_{E_0}^0 S(E)^{-1} dE = \int_0^{E_0} \left( \frac{dE}{dx} \right)^{-1} dE.$$

Here,  $E$  is the kinetic energy. The integration implies the so-called continuous-slowing-down-approximation (CSDA) which neglects the stochasticity of the energy transfer while not projecting the zigzag path of the projectile on the trajectorial axis. For a 100 MeV proton in liquid water, the difference between CSDA and projected range is  $\approx .1$  mm (Berger et al.). Because the stopping power enters the range inversely and  $S(E) \propto Z^2/A$  for the Bethe equation without terms of higher order, range for non-proton ions as a function of kinetic energy per nucleon can be estimated by scaling the proton range with  $A/Z^2$ . For protons in water, the range-energy relation is well described by a power law (Bortfeld 1997) with

$$R = \alpha E^p$$

where  $\alpha = 0.0022$  and  $p = 1.77$ .  $E$  is the initial kinetic energy of the proton in MeV and  $R$  is the range in cm.

The energy transferred by a heavy charged particle with kinetic energy less than its rest-mass energy to an electron is limited to  $\simeq 2m_e c^2 \beta^2 / (1 - \beta^2)$  by kinematics (Attix 1986; ICRU 1993), the average transferred energy is about 1 keV per electron. Angular deflections of the primary particle due to scattering on the electron's Coulomb potential are only small. Coulomb scattering on the atomic nuclei on the other hand contributes significantly to lateral beam spreadening, but this is only relevant for kinetic energies  $< 1$  MeV/u. The contribution of nuclear Coulomb

interactions to the total stopping power can be neglected throughout most of the depth: For protons, only at a kinetic energy of about 10 keV (corresponding to sub-mm residual range) is the impact of the nuclear stopping power comparable to the electronic one.

The energy transferred to an electron may be sufficiently large for the electron to ionize further atoms on its path. Long-range secondary electrons with a high energy transferred to and able to ionize further atoms are called  $\delta$ -electrons.

Nuclear reactions involving hadronic interaction are responsible for loss of primary particle fluence. Byproducts are fragments and neutrons.

For clinical energies, bremsstrahlung mechanisms and convoy electrons can be neglected. However, pick-up and stripping of electrons by the projectile leading to screening of the primary particle's charge can not be neglected and are essential near the bragg peak because just before coming to rest, the projectile charge is almost completely screened. This effect is empirically described by the Barkas formula (Barkas and Berger 1964)

$$z_{eff} = z \left[ 1 - e^{125\beta z^{-\frac{2}{3}}} \right]$$

When considering beams instead of single particles, the different angular deflections at the scatter events of the projectiles and the stochasticity of the ionization events lead to a broadening and a drop of the beam's Bragg peak due to small deviations from monoenergeticity known as "straggeling". Due to the random nature of the ionization events, the energy distribution of the primary particles is expected to be gaussian-shaped. In 1915, a formula for the distribution of the energy loss of an initially monoenergetic particle beam traversing a target with thickness  $\Delta x$ , density of atoms  $N$  and atomic number  $Z$  was found by Bohr (Bohr 1915); here, the relativistic formulation (Ahlen 1980) is presented:

$$f_{\Delta x}(\Delta E) = \frac{1}{\sqrt{2\pi}\sigma} \exp\left(-\frac{(\Delta E - \langle \Delta E \rangle)^2}{2\sigma^2}\right)$$

$$\sigma^2 = 4\pi z_{eff}^2 Z e^4 N \Delta x \frac{1 - \frac{\beta^2}{2}}{1 - \beta^2}.$$

Straggeling has to be kept in mind in FNTD spectroscopy experiments, because initially monoenergetic HCPs slowed down in matter do not have the same LET but are rather distributed around some expectation value.

Lateral scattering due to the momentum transfers result in a broadening of the particle beam. A very precise calculation can be done using Molière theory (Molière 1948). For thin targets, Highland's formula gives a good approximation. It gives the  $\sigma_\theta$  of the gaussian angular distribution:

$$\sigma_\theta = \frac{14.1\text{MeV}}{\beta pc} z_{eff} \sqrt{\frac{d}{L_{rad}}} \left( 1 + \frac{1}{9} \log_{10} \frac{d}{L_{rad}} \right)$$

where  $p$  is the momentum of the projectile,  $d$  the thickness of the scatterer and  $L_{rad}$  the radiation length of the scattering material, given in g/cm<sup>2</sup>.  $L_{rad}$  values are tabulated for many materials and can be found in (Tsai 1974).

In this thesis, however, a more convenient approximation for the rms lateral scattering radius  $\sigma$  for a pencil beam at the end of the penetration depth  $R$  is used for calculations. Chu et al. (1993) gives

$$\sigma = 0.00294 R^{0.896} Z^{-0.207} A^{-0.396}$$

where  $Z$  and  $A$  are the atomic and the mass number, respectively, of the projectile particle and both  $R$  and  $\sigma$  are in cm.

### 2.1.4 Linear energy transfer - LET

#### Definition

In the context of radiooncology and track detectors, one is interested in the ionization density along the particle trajectory: In the former, because of DNA lesion clusterings, in the latter because of track formation along the particle path. High-energetic  $\delta$ -electrons carry a significant amount of energy away from the trajectory of the primary particle. To account only for the energy transfers contributing to the ionization density in the core of the HCP track, the linear energy transfer  $LET_{\Delta}$  was introduced (ICRU 1970). Here, the “collision” stopping power  $S^{coll} = S^{electr.} + S^{nuclear,Coulomb}$  of the energy transferred to secondary particles is taken into account only up to a certain upper limit  $\Delta$  of transferred energy in a single ionization event. For example,  $LET_{100\text{eV}}$  is the collision stopping power excluding all energy transfers exceeding 100 eV in a single event. In general,  $LET_{\Delta} \leq S(E)^{coll}$  and  $LET_{\infty} = S(E)^{coll}$ .

*Cum grano salis*, the energy cut-off can be regarded as a pipe around the particle track, and only energy transferred to secondary particles not leaving the pipe is taken into account. As usual, LET without a subscript refers to the  $LET_{\infty}$ .

#### Limitations of the LET concept

Particles with different charge and velocity can exhibit the same LET. Yet, the energy distribution of the  $\delta$ -electrons primarily depends on the velocity of the particle. Also, the LET concept neglects the stochasticity of the energy transfer. In addition, arbitrary cut-off energies may not be useful: If the LET changes significantly within the reference volume or a large amount of energy transfer is carried out by  $\delta$ -electrons exceeding the cut-off, the applicability of the LET concept is questionable. For a deeper discussion on the regimes of applicability, the interested reader is referred to (Schlegel and Bille 2002).

### 2.1.5 Fragmentation and neutron production

When traversing a medium, heavy charged particles may interact with the nuclei of the medium hadronically. Since hadronic interactions involve momentum transfer to the nucleonic substructure, they are inelastic and lead to a decrease in fluence along the central beam axis. In general, a target nucleus is in an elevated excitation state after being hit by a hadronic projectile. Deexcitation may happen via gamma, nucleon or alpha particle emission from the possibly unstable compound nucleus. More frequent than a full-on hit of a projectile particle with a target nucleus is a partial, peripheral hit. A simple model of what happens at such a partial hit is the abrasion-ablation model (Bowman *et al.* 1973). In its simplest form, projectile and target are considered sharp spheres; with an impact parameter smaller than the sum of the radii, there is a region of geometrical overlapping. The collision takes only about  $10^{-23}$  s which is about the time the projectile needs for passing the target nucleus. Because the projectile energy is much larger than the Fermi energy of the nucleons in the target nucleus, one can assume that only nucleons from the overlap zone contribute to the reaction (Gunzert-Marx 2004). In the first step, the projectile particle is considered to be abraded where the overlap zone is. This means the remaining, not abraded projectile part continues to propagate with the same kinetic energy per nucleon as the whole projectile did before the hit. In the second step, ablation is taken into account: As Bowman *et al.* pointed out the “nucleus after the abrasion looks very funny, with a concave cylindrical surface where used to be a convex spherical surface. Its surface energy is not what a healthy ground-state configuration ... would like, but quite a few MeV higher.” Again, deexcitation may happen by gamma, nucleon or alpha particle emission. While the deexcitation of the target nuclei happens in an isotropic manner, projectile fragments have a highly anisotropic momentum distribution, namely being forward scattered, i.e. in direction of the primary particle beam.

#### Antiproton annihilation

Fast antiprotons traversing matter feature the same stopping power as protons because the electromagnetic interaction with the electrons transfers the same amount of energy for both attracting and repulsing projectiles as indicated by the squared charge of the projectile in the Bethe formula (there is, however, a higher-order correction term  $\propto z^3$  — the Barkas-Andersen correction). Fluence reduction of antiprotons along the beam axis is only slightly larger than for protons and is less than for carbon ions (Bassler *et al.* 2005). In the Bragg peak region, however, antiprotons are captured by atomic nuclei, preferably to high-Z nuclei: In a polystyrene target, 99 % of the antiprotons annihilate on carbon nuclei (Ponomarev 1973). When reaching the surface of the nucleus, antiprotons annihilate by emission of on average 4 or 5 pions (Agnew *et al.* 1960; Mitio 1989).  $\pi^0$  particles are highly unstable ( $\tau$  in the order of  $10^{-16}$  s (Nakamura K. *et al.* (Particle Data Group) 2010)) and decay into high energy gamma rays with roughly 70–300 MeV (Agnew *et al.* 1960). Because



of the solid angle covered by it, 1 or 2 of the charged pions are likely to penetrate the nucleus, inducing an intra-nuclear cascade that causes the nucleus to break into fragments (Markiel et al. 1988; Cugnon et al. 2001; Polster et al. 1995). Charged fragments have only little kinetic energy and thus a short range but a high LET. Only  $\approx 30$  MeV is deposited in the last  $.5 \frac{\text{g}}{\text{cm}^2}$  (Gray and Kalogeropoulos 1984; Sullivan 1985) but this is still an increase of dose in the peak of a factor of 2 in comparison to protons.

Readers interested in antiproton radiobiology which is beyond the scope of this thesis are referred to (Holzscheiter et al. 2009).

### 2.1.6 Beam quality

For different radiation types, the local ionization density is different. Gamma radiation ionization density in an arbitrary medium is considered spatially homogeneous when applying clinical doses. In contrast, the local ionization density of particle radiation is highly heterogeneous: Each particle traversing the medium leaves a track with a highly ionized core and a penumbra of decreasing ionization density with increasing distance to the track central axis. Track structure measurements give an upper limit of 0.3 nm for the core radius of 2.57 MeV/u oxygen ion tracks (Varma et al. 1977). This magnitude has to be set in a relation to the size of the DNA double strand with a diameter of about 2 nm. Nucleosomes, the basic packaging unit of the DNA have a diameter of approx. 10 nm and chromatin fibers in which the DNA is condensed have a typical diameter of approx. 25 nm. Hence it is self-evident that different radiation types yield different cell kill fractions when applying the same dose. To quantify and compare this radiation dependent killing potential, the quantity of relative biological effectiveness (RBE) was introduced (Lea (1946), see also IAEA (2008)).

$$RBE_{effect} = \frac{D_{ref}}{D}$$

The RBE is defined as the quotient of the amount of dose of some well-defined reference radiation necessary to achieve a certain, well-defined effect and the dose of the radiation under respect necessary to achieve the same effect. Predominant reference radiation is the gamma radiation of the Co-60 decay into Ni-60. As isoeffect, often a cell survival fraction of 10 % is used, but other numbers (1 %, 50%, ...) are used as well. Also, a certain amount of chromosome aberrations or quantities like certain tumor control probability (TCP) or normal tissue complication probability (NTCP) values are used, especially in animal experiments. In respect to different endpoints, the RBE of the same radiation is generally also different.

The RBE-weighted dose  $D_{RBE}$  is defined as the product of absorbed dose times the RBE. By definition the RBE is a dimensionless pure number, thus the unit of the RBE-weighted dose is also gray (Gy). To account for the possible confusion, it is recommended to express  $D_{RBE}$  in Gy followed by a space and the parenthetical

descriptor “(RBE)” (ICRU 2007).

The variation of RBE due to differences in the ionization density is an expression of different beam quality. For the same delivered dose, beam quality is dependent on LET and particle species: Both quantities shape the radial dose profile of a particle track, the LET gives the energy transferred while the range of the  $\delta$ -electrons depends only on the kinetic energy per nucleon of the projectile. A common parameterization of the size of the track penumbra is

$$r = 61.6 \left( \frac{E}{m} \right)^{1.7}$$

,where  $r$  is given in nm and  $E/m$  is the kinetic energy divided by the ion mass in atomic mass units (Kiefer and Straaten 1986). For a 270 MeV/u carbon ion this means a maximum secondary electron range of 840  $\mu\text{m}$ .

## 2.2 Confocal microscopy

A schematic of the light path in confocal microscopy is shown in Figure 2.1.

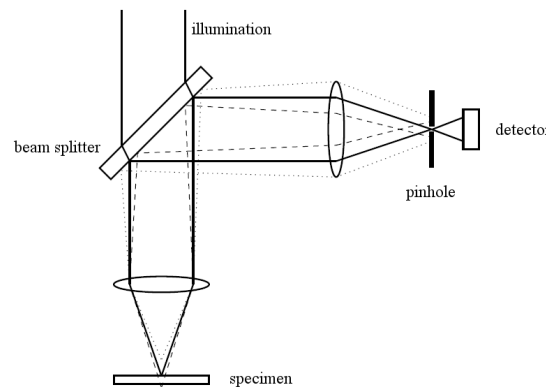


Figure 2.1: Confocal setup after (Fischer 1996)

The essence of confocal laser scanning microscopy is point illumination and point detection. In contrast to ordinary (widefield) microscopy, this allows for diffraction-limited resolution. Fluorescence inducing stimulation light from a laser source is reflected from a beamsplitter through the objective lens, focused in the specimen. Although fluorescence is stimulated not only in the focal spot, but also the light cone in front of and behind the focal plane, this is called point illumination because in contrast to ordinary widefield microscopy, illumination is not homogeneous on the whole specimen but on the contrary highly focused.

Fluorescence light passing through the objective lense and the beamsplitter is then detected. So stimulation and fluorescence light use temporarily the same lightpath. After the beamsplitter, the fluorescence light is focused again by the tube lense. A

circular aperture (commonly referred to as the pinhole) positioned at the focus of the tube lense and thus at optically conjugate point to the focus in the specimen obstructing all light rays off focus effectively limits the volume of detection in axial direction. This way, depth resolution is achieved. Attached to piezo crystals, scanning mirrors in the lightpath deflect the stimulation/detection focus in lateral dimension. In combination with a motor enabling movements of the specimen in z-direction (i.e. axially), three-dimensional imaging is realized.

The signal of a delta-distributed region, commonly referred to as point spread function ( $PSF$ ), is the product of the point spread illumination function ( $PSF_{\text{ill}}$ ) and the point spread detection ( $PSF_{\text{dect}}$ ).

$$PSF = PSF_{\text{ill}} \cdot PSF_{\text{dect}}$$

It has to be kept in mind that the point spread illumination is not the illumination of a fluorescent delta-distribution, but the illumination of a fluorescent medium when reading a delta-distribution.

In axial direction, both PSFs fall off with  $z^{-2}$  with increasing distance from the focal plane so the overall PSF falls off with  $z^{-4}$  with increasing distance from the focal plane. Laterally, spatial resolution is limited by diffraction. In contrast to ray-geometric optics, a monochromatic light beam of uniform intensity (a flat top beam) and sufficient coherence length transmitting a circular aperture does not result in a sharp circular spot but a diffraction pattern called Airy pattern yielded by the Fraunhofer approximated Fresnel diffraction integral and described by the Bessel function of the first kind of order one. The Fresnel diffraction integral is given by

$$E(x, y, z) = \frac{z}{i\lambda} \iint E(x', y', 0) \frac{e^{ikr}}{r^2} dx' dy'$$

where the integration takes place over the aperture plane and  $E(x', y', 0)$  is  $\neq 0$  for  $x', y'$  in the aperture.  $r$  is defined as  $\sqrt{(x - x')^2 + (y - y')^2 + z^2}$ . In the Fraunhofer approximation, the integral looks as follows:

$$E(x, y, z) = \frac{e^{ikz} e^{\frac{ik}{2z}(x^2+y^2)}}{i\lambda z} \iint_{-\infty}^{\infty} E(x', y', 0) e^{-i\frac{2\pi}{\lambda z}(x'x+y'y)} dx' dy'$$

Fraunhofer approximation is a far-field approximation valid e.g. for microscope-like optical setups. The diffraction pattern consists of a spot in the middle (the so-called Airy disc) together with concentric circles separated by minima of zero intensity.

The Airy pattern is given by

$$I(\theta) = I_0 \left( \frac{2J_1(ka \sin(\theta))}{ka \sin(\theta)} \right)^2$$

$$J_n(x) = \sum_{r=0}^{\infty} \frac{(-1)^r \left(\frac{x}{2}\right)^{2r+n}}{\Gamma(n+r+1)r!}$$

where  $k$  is the wave number  $\frac{\lambda}{2\pi}$ ,  $a$  the radius of the aperture and  $\theta$  the angle from the beam axis.  $J_1$  is the mentioned order one Bessel function of the first kind and  $I_0$  is the intensity in the maximum. In Figure 2.2,  $I(x)/I_0$  is plotted against  $ka \sin(\theta)$ .

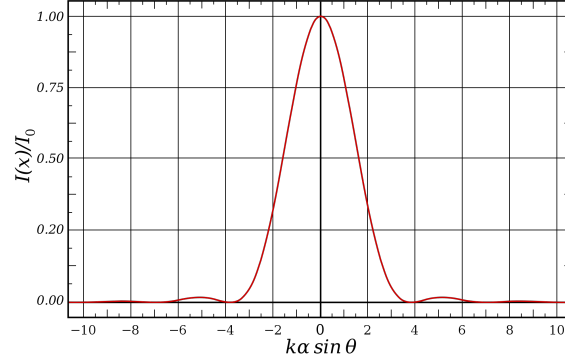


Figure 2.2: Airy pattern, ([Wikimedia Commons 2009](#))

The first minimum is located at  $\approx 3.8317$ . This leads to the angular radius of the Airy disc satisfying  $\sin(\theta) \approx 0.61 \frac{\lambda}{NA}$  or spatially  $r \approx 0.61 \frac{\lambda}{NA}$  in the focal plane of a microscope, where  $NA$  is the numerical aperture of the setup. According to the Rayleigh-criterion, two points can be considered resolved when their angular separation is equal to the Airy disc radius.

Due to the combination of  $PSF_{\text{ill}}$  and  $PSF_{\text{dect}}$ , the Rayleigh-criterion for diffraction-limited resolution is reduced about 30% to  $r \approx 0.4 \frac{\lambda}{NA}$ .

Under ordinary conditions, a pinhole size equal to the Airy disc is the optimal trade-off between depth resolution, lateral resolution and fluorescence photon shot noise due to reduced signal ([Car 2008](#)).

# Chapter 3

## Methods & Materials

In this chapter, firstly the properties of the detector material are addressed in section 3.1. The irradiation modalities and the read-out technique are explained in section 3.2 and 3.3. The last section 3.4 is about the techniques and technologies used for data processing.

### 3.1 $\text{Al}_2\text{O}_3\text{:C,Mg}$

Also known as sapphire or corund,  $\alpha\text{-Al}_2\text{O}_3$  comes with a Mohs-hardness of 9–9.5 and is the second hardest natural material. Its density is  $3.97 \frac{\text{g}}{\text{cm}^3}$  and the effective charge  $Z_{\text{eff}}$  is  $\approx 11$ .

Since it is a wide gap insulator ( $E_g = 9.5$  eV), the possibility is given to engineer deep and thermally stable electron and hole trapping centers. Doped with carbon,  $\text{Al}_2\text{O}_3\text{:C}$  is a material widely used in luminescence dosimetry for radiation protection (Bøtter-Jensen et al. 2003). There, stimulation with light induces radiative recombination of trapped secondary electrons released there by ionizing radiation. Additionally doped with Magnesium ( $\text{Al}_2\text{O}_3\text{:C,Mg}$ ), this material offers unique properties: In 2003, it has been introduced as optical data storage medium (Akselrod et al. 2003). Use as fluorescent nuclear track detector (FNTD, Figure 3.1) was proposed in 2006 (Akselrod et al. 2006a). A more detailed review over the literature is given in the discussion (section 5.1).

#### 3.1.1 Crystal lattice structure of $\alpha\text{-Al}_2\text{O}_3\text{:C,Mg}$

The structure of  $\text{Al}_2\text{O}_3\text{:C,Mg}$  is a rhombohedral lattice with a rigid, slightly distorted hexagonal-close-packed  $\text{O}^{2-}$  sublattice,  $\text{Al}^{3+}$  ions occupying two out of three octahedral interstices.

Crystals are grown from the melt using the Czochralski method (Arendt and Hullinger 1989) in a highly reducing atmosphere with a low partial pressure of oxygen in the presence of carbon which causes aggregation of oxygen vacancies in the crystal lattice. The additional presence of magnesium during the crystal growth process promotes the substitution of  $\text{Al}^{3+}$  with  $\text{Mg}^{2+}$ . After the growth process, FNTD chips are cut with the long side along to the c-axis—i.e. the body diagonal of the

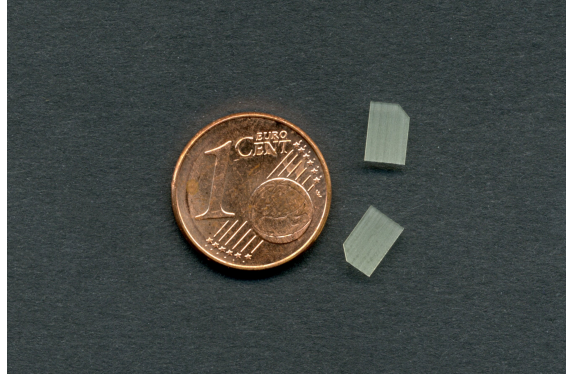


Figure 3.1: The FNTDs used in this thesis had dimensions of  $4 \times 6 \text{ mm}^2$  and a thickness of .5 mm

rhombohedral unit cell—because of anisotropies (Sanyal and Akselrod 2005) and afterwards polished on one side using diamond and silica suspensions.

### 3.1.2 The $F_2^{2+}(2\text{Mg})$ cluster defect

$F$ -centers, also known as farb-centers, are anion deficiencies in a crystal where electrons are captured in the potential well of the vacancy, causing otherwise colorless crystals to become colorful because of the visible excitation/emission spectra of the electrons in these potential wells. Crystal growth in a highly reducing atmosphere thus promotes aggregation of  $F$ -centers. Each  $\text{O}^{2-}$  ion in the crystal lattice is surrounded by four nearest-neighbor  $\text{Al}^{3+}$  ions. If two nearby  $F^+$ -centers ( $F$ -centers where the amount of charge of the electrons is one elementary charge below the respective anion, in this case the  $\text{O}^{2-}$ ) are accompanied by two  $\text{Mg}^{2+}$  ions that charge-compensate—then the  $F$ -centers can associate and build a neutral, stable cluster called  $F_2^{2+}(2\text{Mg})$ . An illustration can be seen in Figure 3.2. Association is realized by distributing the wave function of the two (quantum mechanically indistinguishable) affected electrons over both defects, hence leading to a lowering of the energy.

### 3.1.3 Radiochromic transformation

Secondary electrons released by ionizing radiation may get captured by cluster defects (see Figure 3.3 for competing electron avenues). In consequence, these clusters undergo a change called radiochromic transformation: the additional electron repels the other electrons while the neighboring lattice atoms feel enhanced attraction (anions) or repulsion (kations). Both effects lead to a (further) deformation of the crystal lattice and thus the electrostatic potential within the cluster in which the electrons are caught is altered. This, then, results in a change of the excitation states of the cluster and consequently in a change of the excitation and emission spectra—and hence, the “coloring” (ancient greek:  $\chi\rho\acute{o}\mu\alpha$ ). For read-out of FNTDs,

Table 3.1: Excitation/emission bands of  $\text{Al}_2\text{O}_3\text{:C,Mg}$ 

excitation wavelength	emission wavelength	crystal defect
255 nm	325 nm	$F^+(Mg)$
240 nm	325 nm	$F^+(Mg)$
300 nm	500 nm	$F_2$
435 nm	510 nm	$F_2^{2+}(2Mg)$
350 nm	385 nm	$F_2^+(Mg)$
620 nm	750 nm	$F_2^+(2Mg)$
335 nm	750 nm	$F_2^+(2Mg)$
260 nm	750 nm	$F_2^+(2Mg)$

the  $F_2^{2+}(2Mg)$  clusters radiochromically transformed to  $F_2^+(2Mg)$  are used.

As a rule of thumb, the average energy spent in an ionization event is 2–3 times the band gap  $E_g$ . For  $\text{Al}_2\text{O}_3\text{:C,Mg}$ , this adds up to about 24 eV per ionization event. The LET of a proton with a kinetic energy of 142 MeV in  $\text{Al}_2\text{O}_3\text{:C,Mg}$  is  $1.16 \text{ MeV} \frac{\text{cm}^2}{\text{g}}$  or  $1.82 \text{ keV}/\mu\text{m}$  (lib). A simple estimation how many ionizations per voxel occur uses the thickness of the illuminated section around the focal plane of the out-reading laser scanning microscope (1  $\mu\text{m}$ ):  $1.82 \frac{\text{keV}}{\mu\text{m}} \cdot 1 \mu\text{m} / 24 \text{ eV} \approx 76$ . The LET of a carbon ion with 270 MeV/u in  $\text{Al}_2\text{O}_3\text{:C,Mg}$  is  $45 \frac{\text{keV}}{\mu\text{m}}$  corresponding to 1900 ionizations. In the bragg peak, a carbon ion has an LET of  $2100 \frac{\text{keV}}{\mu\text{m}}$ , corresponding to 88500 ionizations or—under the assumption, the ionizations take place in a volume of  $1 \mu\text{m}^3$ —ionization of one atom out of  $1.3 \cdot 10^6$ . The concentration of Mg in the FNTD crystal has been determined by spectral analysis to be 27 ppm (Akselrod and Akselrod 2006).

### 3.1.4 Excitation/emission spectra of $\text{Al}_2\text{O}_3\text{:C,Mg}$

$\text{Al}_2\text{O}_3\text{:C,Mg}$ 's doping with Mg and crystal growth in a highly reducing atmosphere result in a variety of excitation/emission bands. Assignment of bands to crystal defects was done by Sykora and Akselrod (2010a) and is given in table 3.1. In Figure 3.4, the excitation/emission spectra of  $\text{Al}_2\text{O}_3\text{:C,Mg}$  can be seen after each step of a sequence of treatment steps: a) as-grown, b) thermally annealed for 17 h at 600 °C, c) optically bleached with 260 nm and 325 nm light and d) irradiated with 100 Gy of x-ray radiation. As the Mg impurities stimulate formation of  $F^+$  defects by charge-compensation, the as-grown photoluminescence (PL) spectrum shows a large concentration of  $F^+(Mg)$ . After annealing, the intensity of the  $F_2^{2+}(2Mg)$  emission is increased by a factor of 1.8. At the same time, the intensity of the  $F^+(Mg)$  luminescence decreases by 10 %. Optical bleaching even more decreases the concentration of  $F^+(Mg)$ . The irradiation with x-rays leads to a decrease in the  $F_2^{2+}(2Mg)$  luminescence accompanied by an increase in  $F_2^+(2Mg)$  luminescence.

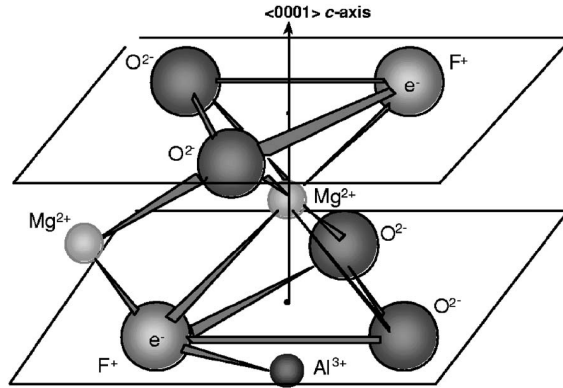


Figure 3.2: Illustration of the  $F_2^{2+}(2Mg)$  defect, (Sanyal and Akselrod 2005)

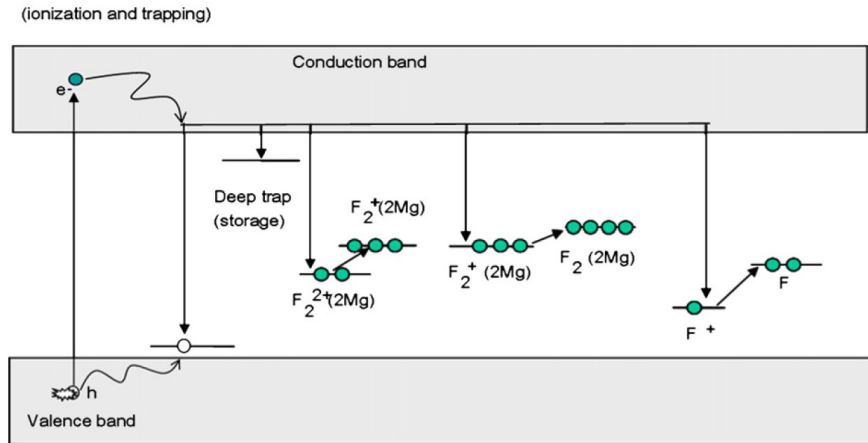


Figure 3.3: Electron avenues in  $Al_2O_3:C,Mg$ : Electrons can recombine with electron-holes, get captured by deep traps,  $F_2^{2+}(2Mg)$ ,  $F_2^{+}(2Mg)$  or  $F^{+}$  defects (from the left to the right), (Sykora and Akselrod 2010a)



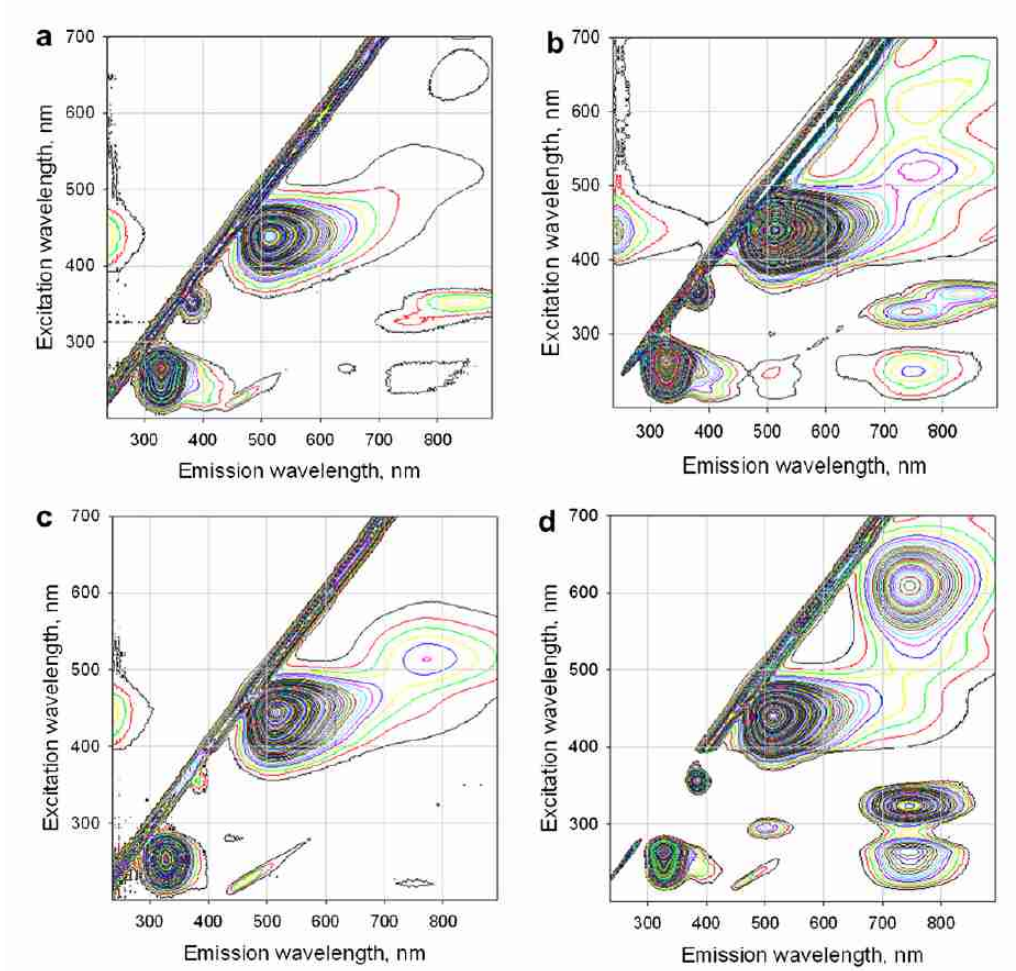


Figure 3.4: Photoluminescence emission / excitation spectra of the same  $\text{Al}_2\text{O}_3:\text{C},\text{Mg}$  crystal a) as-grown, b) thermally annealed for 17 h at 600 °C, c) optically bleached with 260 nm and 325 nm light and d) irradiated with 100 Gy of x-ray radiation, (Sykora and Akselrod 2010a)

## 3.2 Irradiation

In this chapter, the irradiation facilities used in this thesis and their relevant specifications are described.

### 3.2.1 Siemens Gammatron S

The Siemens Gammatron S is the DKFZ in-house Co-60 gamma radiation device. Its source is a rod of the size in the magnitude of some cubic centimeters. The isotope of cobalt with mass number 60 (Co-60) in the source is instable and decays by beta emission to Ni-60 with a halflife of 5.27 years. This is the reason for the sequential emission of two gamma photons—one with an energy of 1.17 MeV and the other one with 1.33 MeV. Only the photons are used in irradiations. The source is shielded with tungsten inside the gantry. For irradiation, the radioactive material is moved from the heavily shielded rest position to the beam window position, where collimators shape the beam to a rectangular field of desired dimensions.

### 3.2.2 Siemens Primus

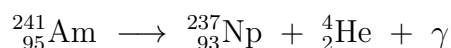
The Siemens Primus is a linear accelerator for electrons, designed for clinical use in radiation oncology. In photon mode, the acceleration voltage is 6 MV. Under reference conditions, the dose-rate is about 2 Gy/min. On the principle of operation, the reader is referred to (Schlegel and Bille 2002, pages 373–393)

### 3.2.3 Sr/Y-90 source

Sr-90 has a half-life of 28.8 a and decays by  $\beta^-$ -emission with a decay energy of 0.546 MeV into the radioactive yttrium isotope Y-90. This, in turn,  $\beta^-$ -decays with a half-life of 64 h and a decay energy of 2.28 MeV into Zr-90, which is stable. According to (ICRU 1970), the LET of 0.5 MeV electrons is 0.206 keV/ $\mu$ m and 0.186 keV/ $\mu$ m for 2 MeV electrons. The Sr/Y-90 beta source used in the thesis was located at the luminescence lab of the University of Heidelberg at the department of geography.

### 3.2.4 Am-241 source

A source of alpha-radiation was accessible at the luminescence laboratory of the department of geography at the University of Heidelberg. The source was made of AmO<sub>2</sub>, where the radioactive Americium-241 decays via alpha emission to Neptunium:



The kinetic energy of alpha particles ( ${}^4_2\text{He}$ ) emitted from Am-241 is about 5.11 MeV = 1.28 MeV/u.

Am-241 has a halflife of 241 a, doserate of the source was  $\approx .70$  mGy/s. Irradiation

was done moving the radioactive material mechanically to the detectors. Prior to irradiation, the device where the detectors were placed was evacuated so that the short-range alpha particles can reach the detector.

### 3.2.5 Heidelberg Ion-beam Therapy center (HIT)

The Heidelberg Ion-beam Therapy Center (HIT) is the first radiotherapy treatment facility dedicated to carbon ions in Europe and the first dedicated facility worldwide to apply the rasterscanning approach (Haberer et al. 1993) of dose delivery to carbon ions in combination with active energy variation. To achieve this, a synchrotron is used for acceleration. Particle species used at HIT for radiotherapy are protons and carbon ions. Beam spots have an approximately gaussian-shaped lateral profile. The beam is deflected by dipole magnets to cover an area of  $20 \times 20 \text{ cm}^2$  by scanning the spot on a 2 mm grid. Available ranges cover the depth in water from 2 cm up to 31 cm in 255 steps for all particles, corresponding to the energy range from 48 to 221 MeV for protons and 89 to 430 MeV/u for carbon ions. In the carbon ion beam, a thin polymethylmethacrylate (PMMA) plate with a ripple structure can be inserted in the beamline in order to spread the very narrow Bragg peak of carbon ions to  $\approx 3 \text{ mm}$  (Weber 1996). Traversal of the ripple structure means a different residual penetration depth while scattering causes to smear out the range differences. In radiotherapy treatments, the ripple filter is inserted in the beam in order to reduce the number of beam spots necessary to cover the tumor volume and, hence, the irradiation time for the patient, but also the calculation time for the treatment plan optimization.

### 3.2.6 AD-4/ACE

The AD-4/antiproton cell experiment examines the effects of antiproton irradiation to cells, investigating the potential for a future antiproton radiotherapy. Being located at CERN, it is the smallest experiment at the antiproton decelerator (AD) (Baird et al. 1997).

The AD is run parasitically to the large hadron collider (LHC). Protons from the proton synchrotron are extracted every 90 s at a momentum of 26 GeV/c, then being directed onto an iridium target where kinetic energy is used for antiproton production. The antiprotons created have a broad momentum spread, whereas the peak of the production yield is for antiprotons with a momentum of 3.2 GeV/c. Decelerated by the AD, the antiprotons are bunched in pulses of 500 ns with each bunch having about  $2\text{--}3 \cdot 10^7$  particles, the momentum being 502 MeV/c corresponding to 127 MeV of kinetic energy or a Bragg peak position at 103.5 mm depth in water. Exiting the beamline through a thin titanium window, the spill fluctuations are monitored by an advanced Roos ion chamber connected to a PTW UNIDOS electrometer.

The beam profile was approximately 2D-gaussian shaped with a  $\sigma$  of about 6–7 mm. Supportive for positioning in z-direction, a calliper was attached to the water phantom. To the coordinate of the calliper, however, a length of 4.675 mm has to

be added due to the geometry of the phantom.

In relation to the middle axis of the phantom, the beam was slightly displaced. In direction of the beam, the displacement added up to 1.5 to 1.7 mm to the right. Because the last dipole magnet was 5 m upstream, angular deflection was negligible.

### 3.3 Microscopy

Confocal laser scanning microscopes are a common tool for cell imaging in biology. One exemplary application in radiobiology is the imaging of DNA double strand breaks by immunofluorescence.

For this thesis, confocal laser scanning microscopy was used as read-out technique of fluorescent nuclear track detectors. Radiation induced increase in the local density of certain fluorescence centers allows for detection of single particle tracks. The underlying theoretical foundations of confocal microscopy have been discussed in section 2.2, the necessary material properties in section 3.1. Now, abilities and limitations of the actually used microscope are addressed in subsection 3.3.1. Tools necessary for the read-out are discussed in subsection 3.3.2.

#### 3.3.1 Zeiss LSM 710 Confocor 3

The microscope used for this thesis is a Zeiss LSM 710 Confocor 3 (Car 2008) provided by the light microscopy facility (LMF) of the DKFZ. Among others, it offers a 633 nm from a Helium-Neon laser line. The objective offering the largest numerical aperture (NA) is a  $63\times / 1.4$  Oil DIC III objective. A large NA is favorable, because of the comparable small numbers of fluorescence photons emitted during FNTD read-out. Plane-apochromatic design of the lenses corrects for chromatic aberrations and distortions in the border region of images. There are two transmission photomultipliers and one reflection photomultiplier, also two avalanche photodiodes (APDs) are included. These APDs are operated at a sampling rate of 20 MHz, yet the software limits the maximum counts to 4 MHz—at a higher exposure level, shutters cut off the light and the detector voltage is shut off to protect the APD from destruction.

11 scanning speeds corresponding to different pixel dwell times are available, ranging from 1 to 177.32  $\mu$ s. Acquisition of images can be done in 8, 12 or 16 bit color depth.

#### 3.3.2 Auxiliary tools

Advantageous for biological cell experiments, the LSM 710 is a realization of an inverted setup which means that the stimulation/detection lightpath is penetrating the specimen from below and not—as usual—from above. This required the detectors to be glued to microscope slides. Slides used were standard ones as used by biologists ( $76 \times 26$  mm<sup>2</sup> with frosted end and cut edges by R. Langenbrink, D-79312, Emmingen); as glue, *Fluoromount G*<sup>TM</sup> by SouthernBiotech was used. This

clear liquidous glue is optimized for fluorescence microscopy by virtue of its reduced autofluorescence. A small drop creating a puddle of 3–4 mm diameter on the slide is sufficient. Air bubbles in the glue can be avoided if the detector is placed carefully with tweezers. Gentle tocking with the tweezers on the middle of the detector right after glueing before the hardening takes place, spreads the glue under the detector so that the surface is even. Hardening takes about 5 minutes.

As immersion medium, *Zeiss immersol 518F<sup>TM</sup>* was used. Air bubbles in the immersion medium are created by wiping off spilled oil from the objective. Wiping off oil may be indicated when changing slides. Because some oil stays on the slide, additional immersion has to be applied to the objective when slides are changed. After read-out of the detectors, cleaning of the objective is done by tissues of lense paper soaked with ethanol.

### 3.4 Data processing

Microscope control and data acquisition was carried out using the microscope software *ZEN 2009* developed by Zeiss. Images were processed using *ImageJ*, a public domain Java program developed by Wayne Rasband ([Rasband 1997-2009](#); [Abramoff et al. 2004](#)). The version used in this thesis is 1.43u.

*ImageJ* was equipped with the plugin *LSM toolbox*, version 4.0g in order to be capable of reading .lsm files, the output format of ZEN. *LSM toolbox* can convert .lsm files to other formats. This feature was used to convert obtained images to .tiff files. *ImageJ* is able to save .tiff files as .txt files. In these text files, images are represented as matrices, whereas one pixel of the image is corresponding to one matrix entry. Converted text image files were analyzed using *R* ([R Development Core Team 2010](#)), a free software program for statistical computation. *R* versions used in this thesis were 2.8 and later. The *R* add-on package *lattice* ([Sarkar 2008](#)) was used for visualization and creation of plots.



# Chapter 4

## Experiments & Results

Prior to data acquisition and processing, the microscope parameters had to be adjusted. The demands to the settings of the microscope are different for FNTD read-out in comparison to ordinary life science use. Optimized parameters are presented in section 4.1. Even with optimized settings, local variations of the APD reading can be observed and are analyzed in section 4.2. The background signal is studied in section 4.3. The background-subtracted signal of a gamma irradiated detector is presented in section 4.4. After this, the results of exposing the detectors to particle radiation are given, beginning with a qualitative look at particle track images (section 4.5) ongoing to an investigation concerning the feasibility of radiation quality measurements in the beam penumbra (section 4.6). Quantitative measurements of single tracks (section 4.7) and track ensembles are presented in section 4.8 (fluence) and 4.9 (fluorescence frequency distribution). At last, an experiment regarding the detection of neutrons is described in section 4.10.

### 4.1 Microscope settings

In comparison to biological specimens, FNTDs emit only little fluorescence. Thus, reasonable signal strength can only be attained by the use of avalanche photo diodes (APDs) which have a greater quantum efficiency than ordinary photomultiplier tubes (PMTs). To exploit the superior spatial resolution of the FNTDs in comparison to PMTs, read-out is required to be performed under conditions of diffraction-limitedness in the red to near-IR regime. While this means a small pixel size, the imaged detail must be sufficiently large so that the number of particle tracks is high enough to have a reliable dataset. The number of particle tracks is chosen so that there is no overlap (see section 4.8.1). Concerning pixel dwell time, there a trade-off has to be made for the tests conducted in this thesis between a high enough signal and a reduction of the photon noise (see subsection 4.2.1) on one side and a reasonable over-all read-out time, especially when acquiring image stacks (i.e. subsequent image acquisition at varying depth) on the other side. Also, limitations to the access of the microscope have to be taken into account. The resolution of  $512 \times 512$  pixels displaying an area of about  $100 \times 100 \mu\text{m}^2$  was chosen to be at the physical limit—i.e. a pixel size smaller than the focal spot size. The exact edgelenhth of the square imaged was  $103.81 \mu\text{m}$  due to discrete steps of the zoom factor. The

laser line of the 633 nm HeNe laser was used at 100 % power corresponding to 5 mW in order to maximize the fluorescence yield. Dwell time of each pixel was set to 50.42  $\mu$ s. A longpass 655 nm filter was placed before the APD in order to filter out light of too short wavelengths. Obtained signal was stored in 16 bit because 8 bit was checked to be cutting off the dynamic range of the measured signal and 12 bit were regarded to be unfavorable due to known issues with some image processing programs. Pinhole size was set to 1 Airy unit (AU) corresponding to a diameter of 45  $\mu$ m. 1 AU is defined as the diameter of the Airy disc in the focal plane which is the position of the pinhole aperture. A pinhole of 1 AU diameter yields an optimal trade-off between resolution and signal. Smaller pinhole diameters lead to improved resolution but a sharp loss in signal intensity.

Amplifier gain and offset are parameters that operate purely in the software domain and do not have an impact on the physical content of acquired datasets. Default values of zero offset and 0.2 amplifier gain were used.

## 4.2 Sources of variation of the APD reading

The APD reading can vary from pixel to pixel for the same microscopic dose and from read-out to read-out for the same pixel. APD reading includes both signal due to exposure of the FNTD to radiation and the fluorescence background independent from any irradiation. There are several contributions to the variation of the APD reading. An overview over the different sources is given in Table 4.1.

### 4.2.1 Photon shot noise

The fluorescence photon noise obeys the poisson distribution and averaging  $N$  images reduces the relative error  $\Delta\mu/\mu$  by a factor of  $1/\sqrt{N}$ .

Taking into account the temporal stability shown in subsection 4.3.2, i.e. particularly the capability of the FNTDs to be read-out multiple times, one can use the measurement of the time series as independent measurements and thus show the photon noise by paying attention to single pixels only. Photon noise will be shown in Figure 4.17 and quantified in Figure 4.16.

### 4.2.2 Relative density of F-center clusters

Structures of the order of 1  $\mu$ m are visible in the APD reading (Figure 4.1). Origin of these structures was suspected either in variations in the relative density  $\varrho(F_2^+(2\text{Mg}))/\varrho(F_2^{2+}(2\text{Mg}))$  prior to any irradiation or in variations due to doping inhomogeneities. The structures are still visible both after the FNTD is thermally annealed for 10-15 min at 680°C (Figure 4.2) and additional treatment with 405 nm laser irradiation that causes photochromic transformation of  $F_2^{2+}(2\text{Mg})$  (Figure 4.3a). This observation means that the structures in the order of 1  $\mu$ m do not originate from fluctuations of the initial variation of the relative density of the involved



Table 4.1: Sources and relevance of signal variations

origin	lengthscale	effect size	subsection
photon shot noise	1 pixel	$\Delta = \sqrt{\mu}$	<a href="#">4.2.1</a>
relative density of F-center clusters	?	$< 1 \%$	<a href="#">4.2.2</a>
ethanol bubbles in immersion oil	$\approx 1 \mu\text{m}$	$< \text{limit of detection}$	<a href="#">4.2.3</a>
doping inhomogeneity	$1 \mu\text{m}$	$\Delta/\mu \approx 7 - 8\%$	<a href="#">4.2.4</a>
environmental radiation	pathlength $\times$ trackdiameter of $\delta$ -electrons from cosmic radiation	single tracks	<a href="#">4.2.5</a>
fluorescent cleaning residues on FNTD surface	$< 1 \mu - 10 \mu$	neglegibel for planes in $\geq 7 \mu\text{m}$ depth from the surface	<a href="#">4.2.6</a>
dust on FNTD surface	$10 - 20 \mu\text{m}$	significant attenuation of light up to full absorption	<a href="#">4.2.7</a>
air bubbles in immersion oil	$10 - 40 \mu\text{m}$	significant lensing of light, both focusing and defocusing	—
microscope sensitivity	$50 \mu\text{m}$	$\Delta/\mu \approx 15 \text{ to } > 20 \%$	<a href="#">4.2.8</a>

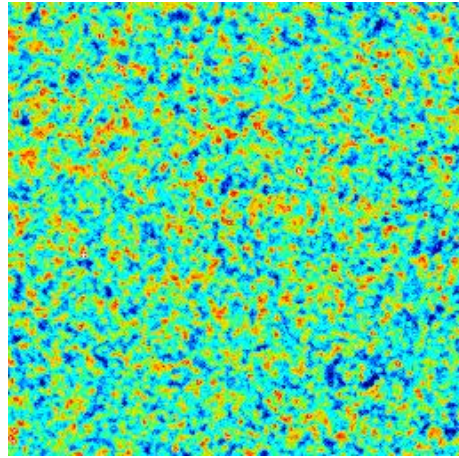
F-center clusters and that these fluctuations can be neglected in the presence of the structures dominating at lengthscales of  $1\text{ }\mu\text{m}$ . Otherwise, the variations would diminish in consequence of the thermal and optical treatment.

### 4.2.3 Ethanol bubbles in immersion oil

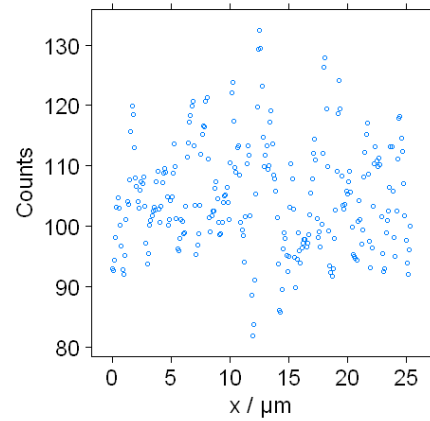
Cleaning of microscope lenses designed for use with immersion media is done with lense paper tissues soaked with ethanol. Subsequent application of immersion oil can result in ethanol bubbles in the immersion oil. Ethanol bubbles are in general smaller than air bubbles and have a negligible capability to distort light rays by lensing. Ethanol bubbles can only be seen through the ocular, when the focal plane is in the immersion medium. This is on the one hand true because ethanol is non-fluorescent and on the other hand because of the reduced optical density difference in comparison to air bubbles.

### 4.2.4 Doping inhomogeneities

Magnesium doping is responsible for the clustering of the F-centers (see section 3.1). The more Mg atoms, the more  $F_2^+(2\text{Mg})$ s (background signal) but also more  $F_2^{2+}(2\text{Mg})$ s (radiation sensitivity) are present. Inhomogeneities in the doping density therefore cause variations in the APD reading.



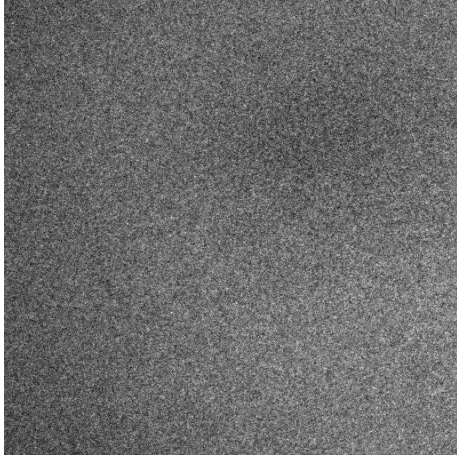
(a)  $25.4 \times 25.4\text{ }\mu\text{m}^2$ , mean pixel value  $= 105.9 \pm 10.4$ . The dimensions are chosen so that illumination variations can be neglected. To cancel out variations due to photon shot noise, the average of 8 read-outs was taken.



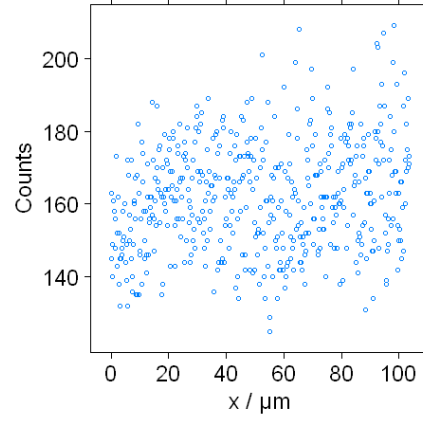
(b) A profile from left to right of Figure 4.1a.

Figure 4.1

## 4.2 Sources of variation of the APD reading

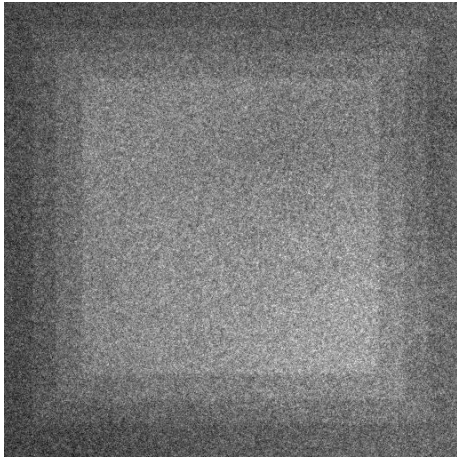


(a) FNTD annealed for 10–15 min at 680 °C. Variations of the APD reading due to doping inhomogeneities are still visible.

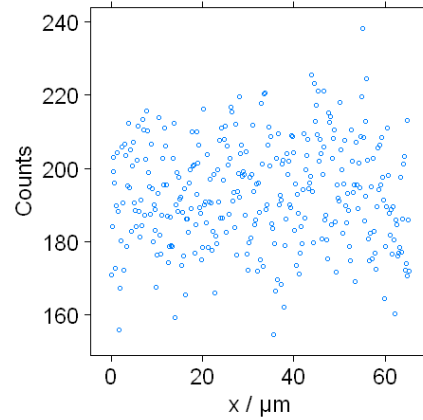


(b) A profile plot from left to right of Figure 4.2a

Figure 4.2



(a) FNTD annealed for 10–15 min at 680 °C, photochromic transformation successively induced by a 405 nm laser.



(b) A profile plot from left to right of the optically most treated square in the middle of Figure 4.3a. Although inhomogeneities due to local relative density fluctuations should be diminished, variations are still observable.

Figure 4.3

### 4.2.5 Environmental radiation

Radon daughter products, terrestrial radiation and cosmic rays make up the natural radiation background ([Bundesamt für Strahlenschutz 2009](#)). Exposed FNTDs record tracks of particles from this radiation background. Measurements concerning the benefits of FNTDs in environmental radiation dosimetry are not in the scope of this thesis. However, environmental particle tracks have to be taken into account when comparing dark images to FNTDs irradiated in ion beams. A fit to the fluorescence frequency histogram, for example, yields more reasonable values than the mean or—most distinctly—the maximal pixel value.

### 4.2.6 Fluorescent cleaning residues

After the removal of adhesives from experimental setups or spilled Fluoromount (see subsection [3.3.2](#)) or cleaning of dust contaminated immersion oil from FNTDs to be re-readout, fluorescent residues can remain. As any fluorescent signal, it is occluded by the pinhole if the microscope's focal plane is set sufficiently far away. Typical bright spots on the surface originating from cleaning residues can be seen in [Figure 4.4](#).

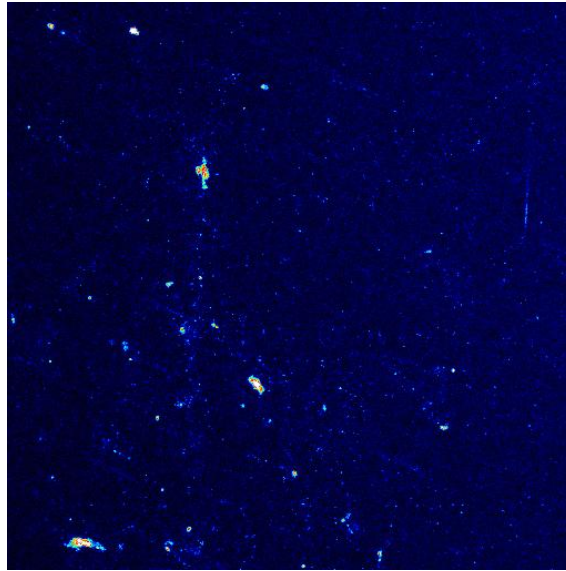


Figure 4.4: Fluorescent cleaning residues on the FNTD surface

### 4.2.7 Dust

Dust on the FNTD's surface in the read-out light path can attenuate both illumination and fluorescence light leading to a local decrease of the signal. An example can be seen in [Figure 4.5](#).

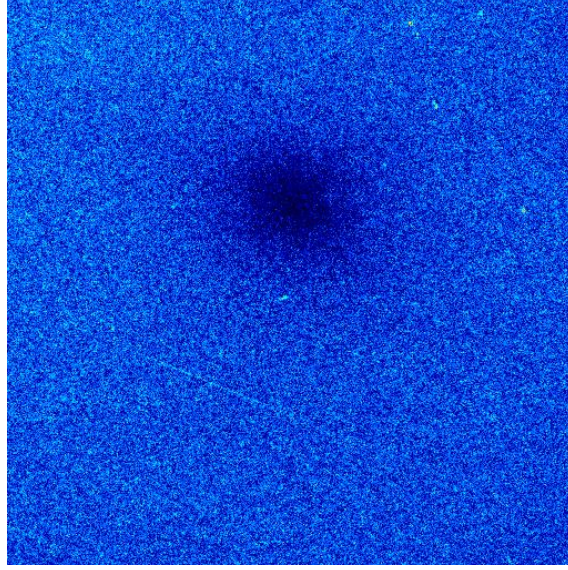


Figure 4.5: Dirt on the FNTD surface absorbs light

#### 4.2.8 Microscope sensitivity

In Figure 4.6, one can see a scan of  $4 \times 4$  tiles (each  $103.81 \times 103.81 \mu\text{m}^2$ ,  $512 \times 512$  pixels). Tile scans leave the optical coordinates of the detail images fixed while using the stage's motor to change the position of the slide. The discontinuity of the background signal and the correlation to the tile grid are visible and indicate thus a variation of the local sensitivity. Most of the area reachable by the scanning optics can be seen in Figure 4.7a. A profile plot along the diagonal of Figure 4.7a can be seen in Figure 4.7b. This way, the need for correction of the sensitivity change is evident as variation is larger than  $\pm 20\%$ . While fluctuations in the relative density are expected to be local, variations in the doping can be of large spatial frequency. However, both signal and background scale equally to doping density. Since illumination variations also scale both signal and background, these two effects can be corrected for with a combined pixelwise correction factor.

### 4.3 Background

The  $\text{Al}_2\text{O}_3:\text{C,Mg}$  FTNDs show a significant fluorescence which is independent from any irradiation. For quantitative analysis, this background has to be removed. This section describes the characteristics (subsection 4.3.1) and the constancy (subsection 4.3.2) of the background signal. From these findings, different correction procedures are presented in subsection 4.3.3.



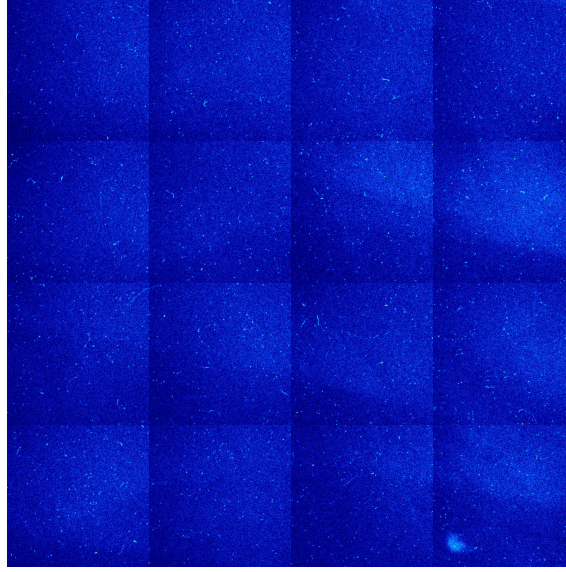
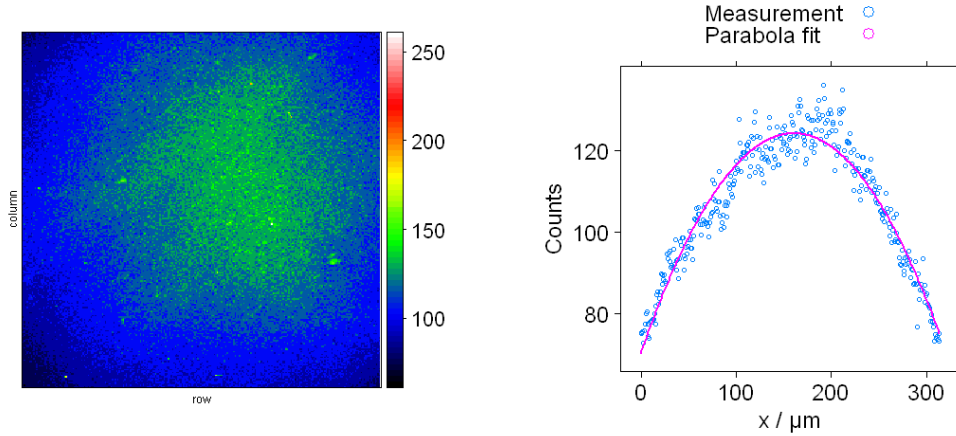


Figure 4.6: Proton irradiated FNTD;  $4 \times 4$  tiles, each with  $103.81 \times 103.81 \mu\text{m}^2$ ,  $512 \times 512$  pixels; the tile grid is visible in the discontinuous pattern which indicates a sensitivity variation of the microscope



(a) Average of 100 images obtained from an unirradiated FNTD;  $224 \times 224 \mu\text{m}^2$ ,  $256 \times 256$  pixels and  $50.42 \mu\text{s}$  dwell time

(b) Profile plot along the diagonal of Figure 4.7a

Figure 4.7

### 4.3.1 Nature of the background signal

The background signal is the APD reading of an unirradiated FNTD. Origin of the background signal is the distribution of  $F_2^+(2\text{Mg})$  prior to any irradiation. Variation of the background can generally be caused both by properties of the FNTD and by properties of the read-out process (see section 4.2).

In Figure 4.8, a typical background signal of a standard size image is shown. Photon noise is suspended by averaging over 35 images. The position was about the central optical axis.

A typical example of a non-averaged background signal including laser noise and deviations from counting statistics is shown in Figure 4.9. The mean signal of Figure 4.9 is 102.6 counts with a standard deviation of 13.9.

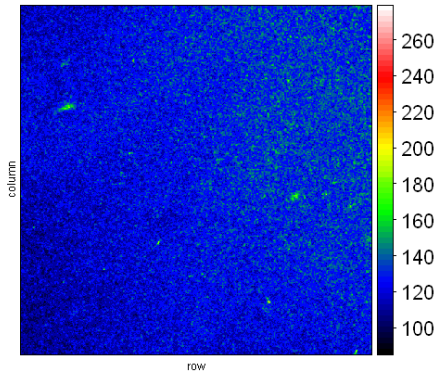


Figure 4.8: Average of 35 images obtained from an unirradiated FNTD;  $103.81 \times 103.81 \mu\text{m}^2$ ,  $512 \times 512$  pixels and 50.42  $\mu\text{s}$  dwell time

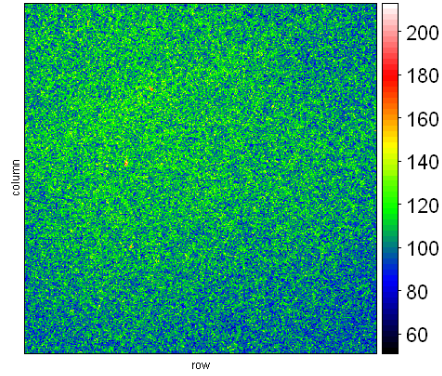


Figure 4.9: Typical “dark” image from an unirradiated FNTD;  $103.81 \times 103.81 \mu\text{m}^2$ ,  $512 \times 512$  pixels and 50.42  $\mu\text{s}$  dwell time. The mean value is  $102.6 \pm 13.9$ .

In Figure 4.10, the logarithmic fluorescence frequency distribution is displayed. The background can appropriately be described by a gaussian bell curve (Figure 4.11). Start value for the fit was the position of the maximum for the mean  $\mu$ , start value of  $\sigma$  was the square root of the position of the maximum. Found values are  $\mu = 101.7$  counts and  $\sigma = 13.8$  counts.

Inhomogeneities caused by the optics not only lead to a difference in the signal, but also to a difference in the fluorescence yield. To measure deviations in the fluorescence yield, the central  $20 \times 20 \mu\text{m}^2$  detail of a standard size image of  $10^7$  carbon ions per  $\text{cm}^2$  was moved on a  $20 \mu\text{m}$  grid while the optically scanned region was fixed. This way, a map of the fluorescence yield or efficiency was obtained. Normalized to the central tile, the map of the means  $\mu$  of gaussian fits to the

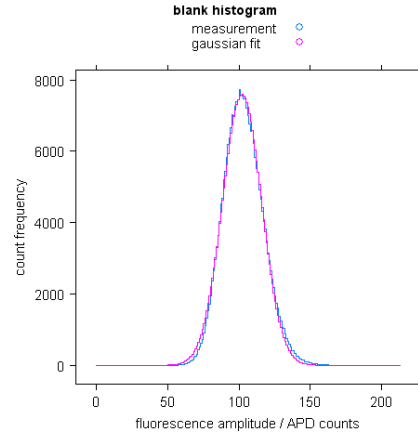
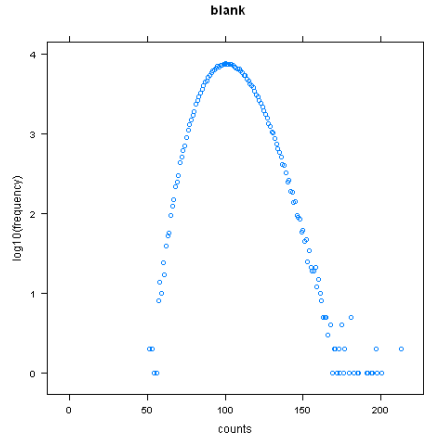


Figure 4.10: Fluorescence frequency distribution of Figure 4.9: how many pixels with a given signal are in the image

Figure 4.11: Fit of a gaussian bell curve to the background signal

histograms of the respective detail is shown in Figure 4.12. In comparison, Figure 4.13 shows the map for the relative fluorescence yield of the pixels with the upper 0.38 % pixel values corresponding to 39 pixels. This value was chosen because  $10^7 \text{ cm}^{-2}$  are  $1000/(100 \times 100 \text{ } \mu\text{m}^2)$  and 1000 divided by 25 tiles is 40.

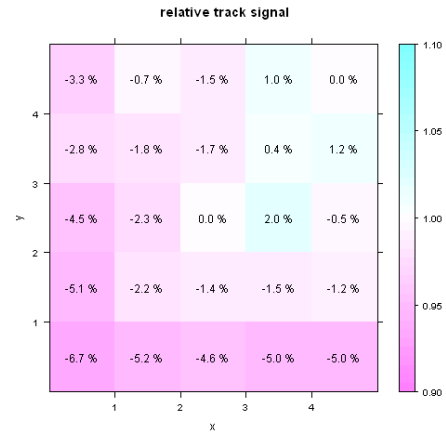
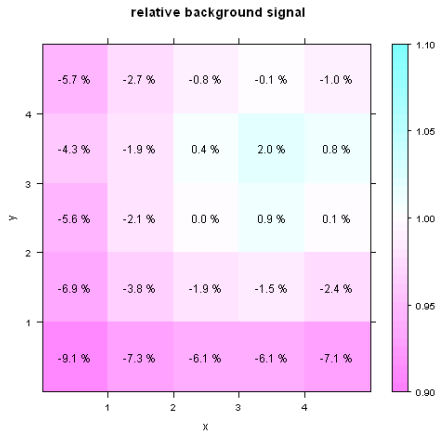


Figure 4.12: Map of the relative background fluorescence

Figure 4.13: Map of the relative track fluorescence

### 4.3.2 Behavior of the background signal

The background signal changes with depth. This is shown in Figure 4.14, where the background signal peak is plotted against depth. The left slope of the peak in Figure 4.14 is due to intrusion of the focal spot into the crystal, leading to an increase of the



illuminated and read-out volume. With increasing  $z$  corresponding to larger depth, a decrease of the signal can be observed. This is caused by the additional amount of material in the lightpath, which causes attenuation due to light scattering and fluorescence being emitted out of the original lightpath.

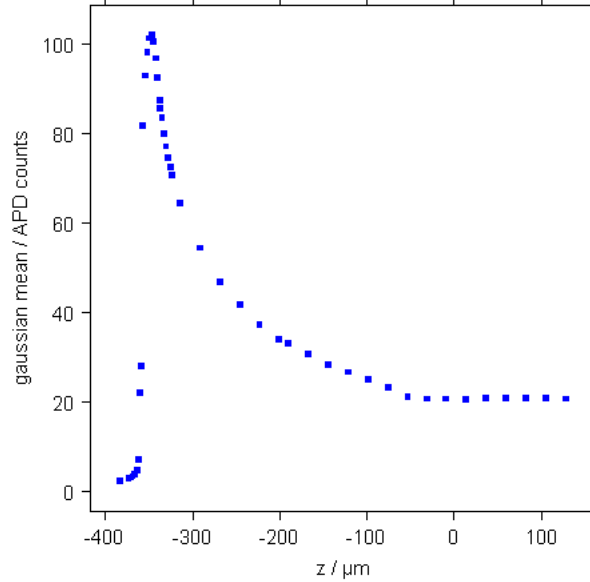
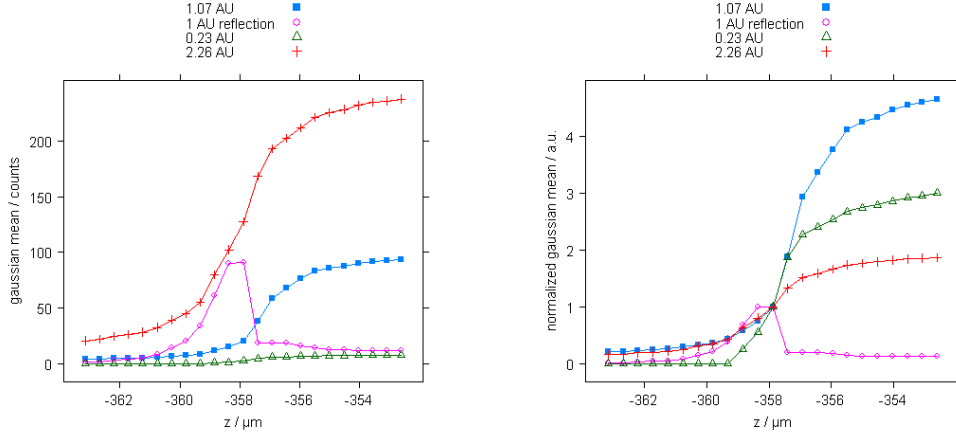


Figure 4.14: Background peak depth profile of an unirradiated FNTD

In Figure 4.15, the background signal near to the FNTD surface is plotted against depth for pinhole sizes of 0.23, 1.07 and 2.26 AU. Comparing the absolute with the relative numbers, one can see the increase in absolute signal for large pinholes but on the other hand an increase in depth resolution for smaller pinholes due to the smaller focus. In addition, the reflection of the stimulation light was detected. A sharp peak at the surface can be seen, enabling precise knowledge of the readout depth.

In order to study temporal stability, a times series of 120 subsequent images was taken. The series was taken with no delay between sequent images, revealing temporal stability and giving a measure of the fluctuations of the stimulation laser and the microscope in the time interval of  $\approx 4$  minutes. For the time series, only  $128 \times 128$  pixels were read-out while keeping the pixel size fixed, resulting in a  $25.46 \times 25.46 \mu\text{m}^2$  square. Figure 4.16 shows the impact of the photon shot noise in the upper two histograms. In contrast to the histogram of the average image (“sum image”) of the 120 images with a standard deviation of 9.4, the distribution of all pixel values of all images has a the standard deviation of 13.7 counts. In the lower two histograms one can see how much separated the distributions of the pixel with the minimal and the maximal mean pixel value are. A comparison of the pixels with the minimal and the maximal average pixel value is shown in Figure 4.17. The green and red



(a) Mean values of Gaussian fits to the background at different depth for several pinhole sizes. In addition, the reflection of the stimulation light from the FNTD surface is shown.

(b) Data from Figure 4.15a, normalized to the values at the depth where the reflection is maximal.

Figure 4.15: Depth profile at the FNTD surface for different pinhole sizes.

horizontal lines correspond to the average values and do not represent a linear fit. The difference of the mean values is about  $4.5 \sigma$ , which is to be considered significant ( $> 3\sigma$ ). Because of this, either a smaller detail has to be chosen so that the variations due to illumination become small or an illumination distribution has to be extracted and corrected for. The former method is used for gamma irradiations (section 4.4) because their relative homogeneity makes subtraction of the mean pixel value an unsuitable choice. The latter method is used for particle irradiations because the background signal between the particle tracks allows for subtraction after the sensitivity correction. Although the background for particle irradiations is merely calculated, it has some advantages, namely that no error due to environmental radiation tracks corrupts the correction procedure. For particle irradiations on the other hand, choosing a smaller detail is often not an option because this would mean a drawback in track statistics and an increase in relative track shot noise.

### 4.3.3 Signal correction

While signal from environmental radiation can be reduced by appropriate shielding, photon shot noise is reduced by averaging several images or increasing the pixel dwell time. Signal distortions by dust and bubbles can be avoided with sufficient care. Still, doping inhomogeneities and the change of the microscope sensitivity in the xy-plane remain. Doping inhomogeneities have a size of the same order as particle tracks, thus making a correction pixel-by-pixel impossible. However, statistical methods can be applied as will be done in section 4.7.

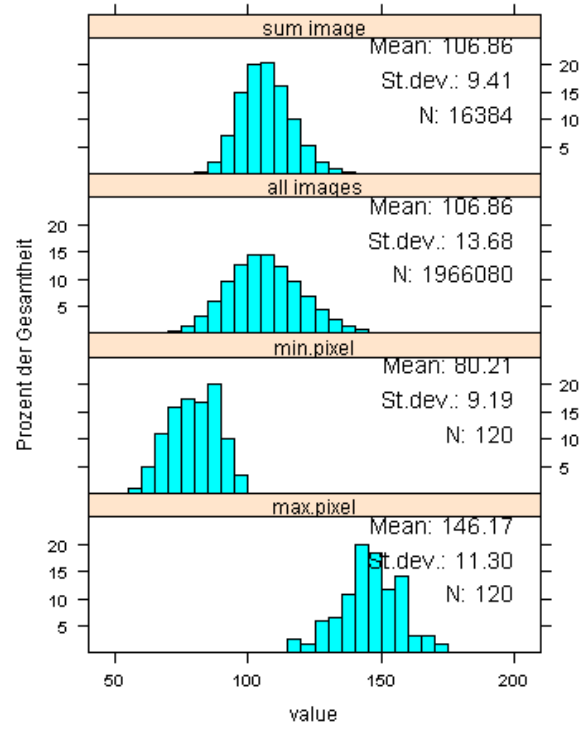


Figure 4.16: Histograms of a time series. From bottom to top: Histogram of the fluorescence of the pixel with the minimal average signal, histogram of the pixel with the maximal average signal, histogram of all images of the series and the histogram of the summed up and normalized image of the series

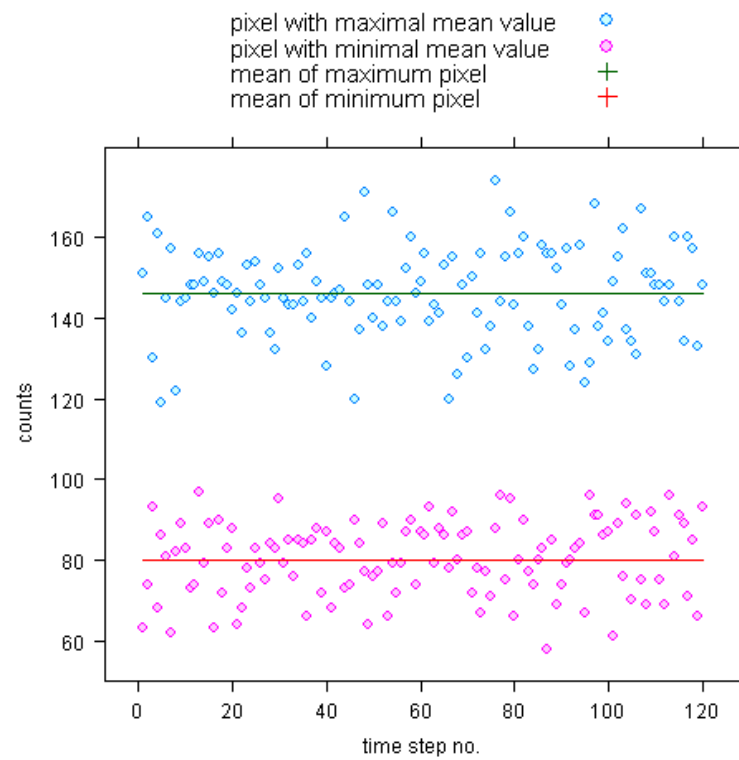


Figure 4.17: Development of the minimal and maximal pixels over time

### Rolling ball interpolation

To correct for the microscope sensitivity, the *subtract background* routine of *ImageJ* (Rasband 1997-2009; Abramoff et al. 2004) was applied using the *rolling ball* algorithm (Sternberg 1983). Here, a ball of defined radius is rolled underneath the surface obtained from understanding the pixel values as height. Prior to the rolling, the surface is automatically smoothed by averaging over  $3 \times 3$  pixels. The optimal ball radius of 1700 pixels was obtained by minimizing the root mean square pixel-wise difference of a normalized interpolated background and the normalized image of an unirradiated FNTD with the same microscope position (see Figure 4.18).

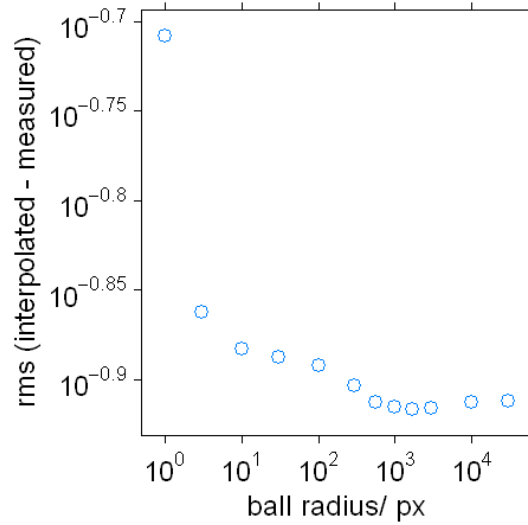


Figure 4.18: The root mean square pixel-wise difference of a standard carbon ion image and the interpolated background against the ball radius parameter in pixel

The rolling ball correction was applied to both proton and carbon ion images. To check the validity of this method, the residual variation in the sensitivity was investigated. To make sure that the reference background shows the same behavior than the images corrected for, images were taken at the border of the area reachable by the microscope optics. Thus, a clear sensitivity gradient was gained.

In Figures 4.19 and 4.20, the difference of the relative interpolated background to the relative measured background normalized pixel-wise to the relative measured background can be seen for protons and carbon ions, respectively. Because here only the large-scale background variations due to the microscope sensitivity are of interest, the two Figures were downsampled. It can be seen that there are still variations after the correction of up to 8 %. In conclusion, this approach fails to reliably extract the background from a given image of particle tracks.

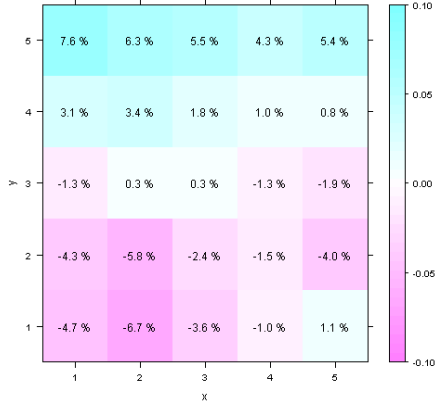


Figure 4.19: Downsampled relative difference of relative interpolated and relative measured background for protons

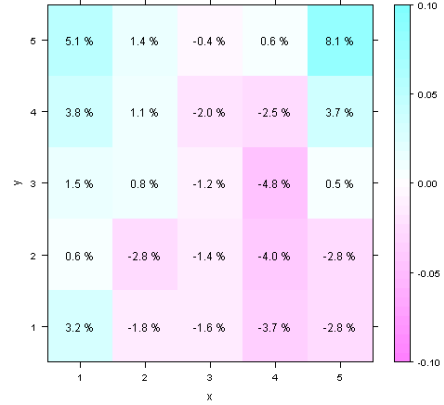


Figure 4.20: Downsampled relative difference of relative interpolated and relative measured background for carbon ions

### Fourier band pass filter

Another method to correct for the variation in the microscope sensitivity is to apply a band pass filter in Fourier space, suspending low spatial frequencies. The optimal value of to what size structures should be filtered was estimated as illustrated in Figure 4.21. On the one hand, if the cut-off value too large, distortions occur while on the other hand information gets lost for a cut-off value too small. A value between 200 and 300 pixels seems adequate which corresponds to the half edge length of a standard image.

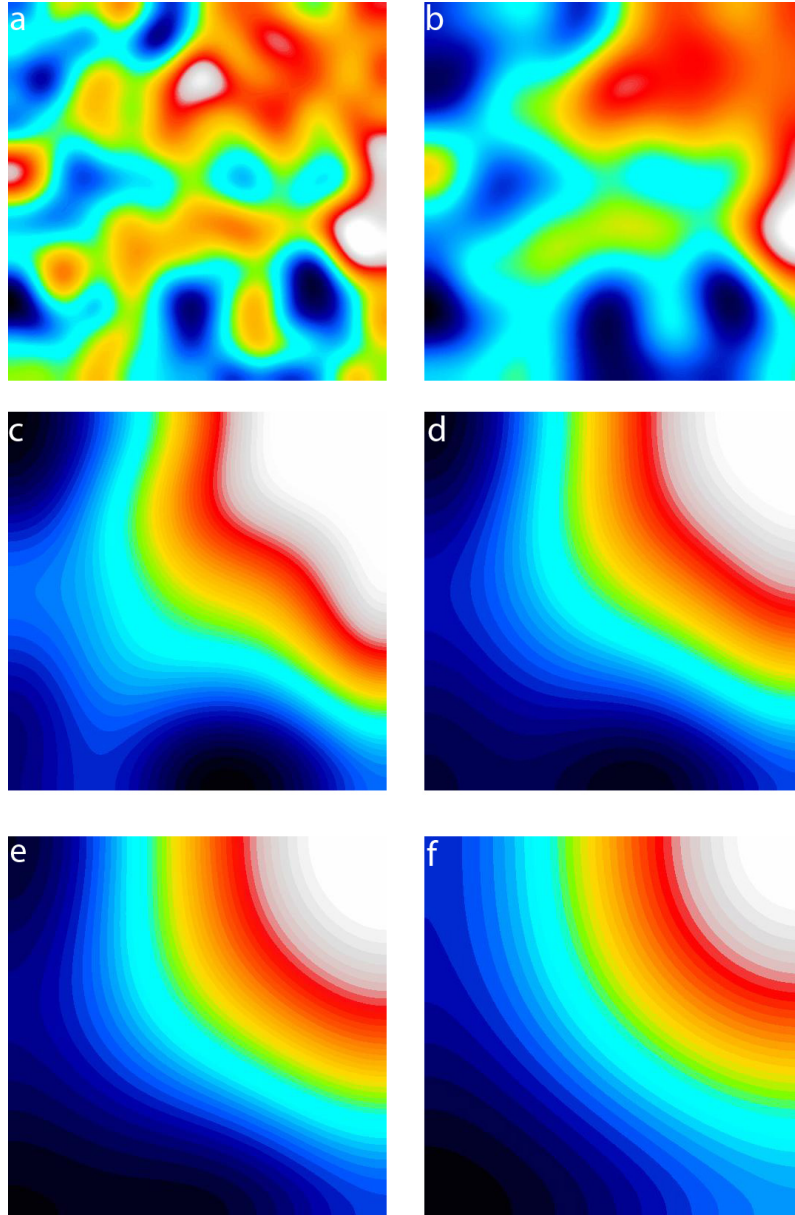


Figure 4.21: Relative background obtained from Fourier band pass filter with suspension of structures larger than a) 64 pixels, b) 100 pixels, c) 200 pixels, d) 256 pixels, e) 300 pixels or f) 400 pixels. Data is corresponding to Figure 4.12

### Local background assessment

The background has been shown to be appropriately described by a Gaussian curve in 4.11. This can be exploited for the assessment of the microscope sensitivity. The image to be corrected is dissected in subareas, then for each subarea a fluorescence frequency histogram is evaluated and subsequently, a Gaussian curve is fitted to the fluorescence frequency distribution. The mean  $\mu$  of the Gaussian is extracted and assigned to the subarea as local background signal. In Figure 4.22, the result of this method can be seen for subareas of  $20 \times 20 \mu\text{m}^2$ . Deviations from Figure 4.12 can be explained by the fact that here no microscope movements were involved. Because a fluence of  $10^7 \text{ cm}^{-2}$  was applied, an increase of the dissection resolution leads to an overestimation of the background.

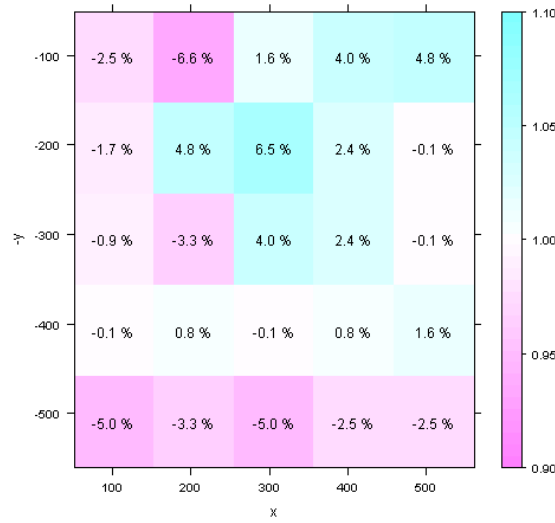


Figure 4.22: Map of the signal variation, obtained by local fits to Gaussian curves

### Conclusion and procedure

The *rolling ball algorithm* has been shown to fail to correct reliably for a FNTD background signal. Because it is easy to use, fast and reliable, the FFT band pass filter is proposed as correction method. When applied as correction, the free parameter is chosen to suspend structures larger than 256 pixels which is the edgelength images with standard settings. The local assessment of the background signal is yet instable for high resolutions as the fit routine has to converge for every detail while the data for the routine to fit to decreases with increasing resolution.

In order to correct for the variation of the fluorescence yield, the low spatial frequency parts are suspended from the original image by the filter. Then, the filtered image is subtracted from the original to get the low spatial frequency part alone. To this low frequency part, then, the mean of the original image is added. The



result is normalized and can then be used as a pixelwise correction to the original image. After the correction, the mean value is subtracted.

## 4.4 Response to gamma radiation

In order to quantify the response of FNTDs to ionizing radiation of different beam quality, first the response to a reference radiation has to be known. Therefore, measurements were conducted to investigate the response of FNTDs to gamma radiation. For low doses, a Co-60 source (subsection 3.2.1) was used. Because of the low dose rate, datapoints for the higher doses were acquired at a clinical linear accelerator (linac, subsection 3.2.2).

### 4.4.1 Setup

Irradiation at the Siemens Gammatron S with Co-60 gamma radiation was done with detectors being placed in a 0.5 mm deepening of a  $30 \times 30 \text{ cm}^2$  polymethylmethacrylate (PMMA) plate with 1 cm thickness. The plate was placed on top of a 4 cm high stack of  $30 \times 30 \text{ cm}^2$  plates from the PTW RW3 slab phantom 29672 as backscatter material and under 3 cm of RW3 as built-up material (see Figure 4.23). The irradiation field size was  $10 \times 10 \text{ cm}^2$ , the source-to-surface distance (SSD) was 80 cm. Irradiation times were calculated from a reference measurement under the same conditions except for the plate containing the ionization chamber not being made of PMMA but RW3.

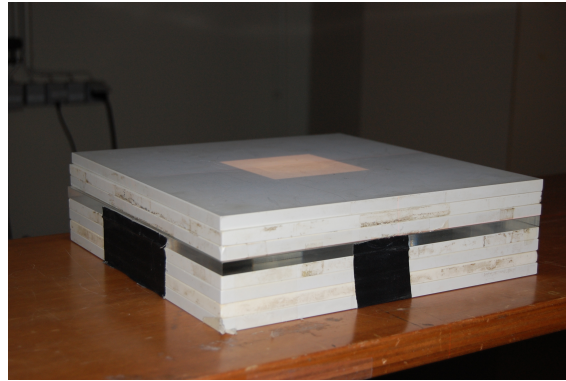


Figure 4.23: Setup of the irradiation at the Siemens Gammatron S

The irradiation at the linac Siemens Primus was conducted under reference conditions: As both build-up and back-scatter material, 10 cm of polystyrol was used. Lateral dimensions of the plates were  $30 \times 30 \text{ cm}^2$ , the irradiation field was  $10 \times 10 \text{ cm}^2$  and SSD was 100 cm. A photo of the setup can be seen in Figure 4.24.

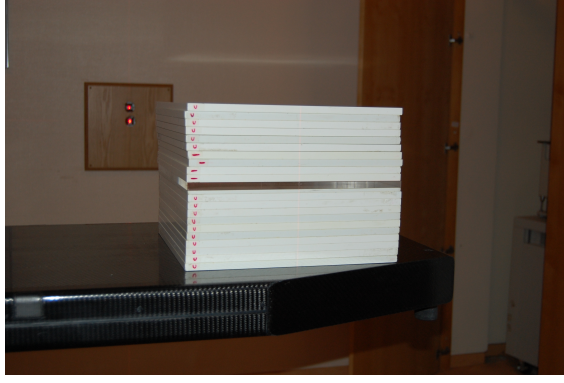


Figure 4.24: Setup of the irradiation at the Siemens Primus

#### 4.4.2 Results

In Figure 4.25, the background-corrected mean pixel value of the inner  $20 \times 20 \mu\text{m}^2$  detail of standard sized images is displayed as a function of absorbed gamma dose. This area was chosen in order to minimize the effect of different illumination intensities while at the same time providing sufficient data. Images were chosen from a stack around the peak background signal in regard to the highest mean signal. The same  $103.81 \times 103.81 \mu\text{m}^2$  lateral dimensions were used for every stack. For the whole data acquisition of this measurement, the pinhole size was set to .29 AU. This was done because of the APD shutdown when high-dose irradiated FNTDs were read out. Pixel dwell time was adjusted to get sufficient high counts to get a pronounced background peak yet inhibiting the APD from shutting down. For background correction, a “dark image” was taken with the same procedure and subtracted. In contrast to the situation when detecting non-overlapping HCP tracks, no background value can be extracted from images when detecting high gamma doses.

Figure 4.26 shows the corrected  $103.81 \times 103.81 \mu\text{m}^2$  images used for 4.25. Images a) – e) corresponding to 0.01 Gy – 1 Gy are from the irradiations conducted at the Gammatron (see 3.2.1), images f) to h) are from the irradiation at the Siemens Primus (see 3.2.2).

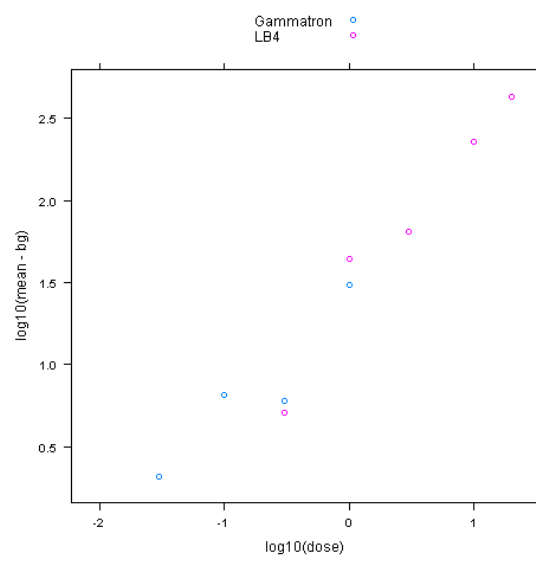


Figure 4.25: Gamma response corrected

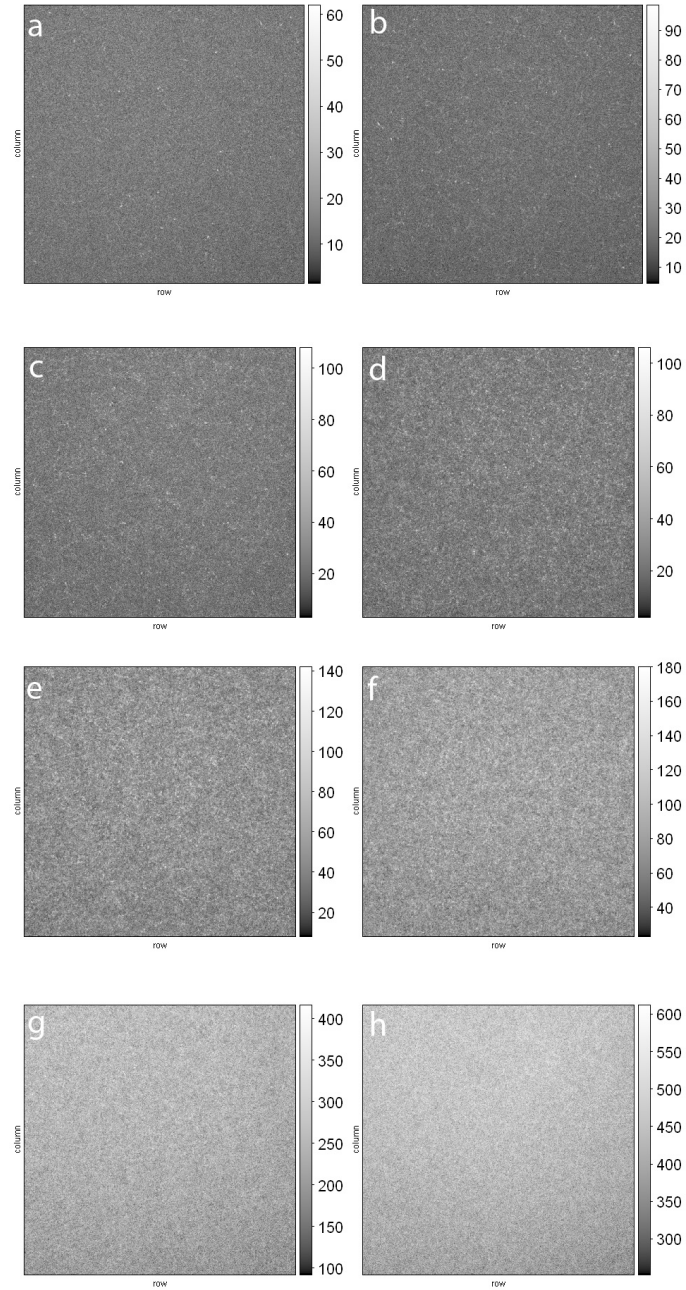


Figure 4.26: FNTD after gamma irradiation with a) 0.01 Gy, b) 0.03 Gy, c) 0.1 Gy, d) 0.3 Gy and e) 1 Gy from the Siemens Gammatron S and f) 3 Gy, g) 10 Gy and h) 20 Gy from the Siemens Primus

## 4.5 Imaging of particle tracks

### 4.5.1 Beta particles

FNTDs irradiated with HCPs show secondary particles emanating from the primary particle tracks (see section 4.5.3). Because of the morphology (low LET, curling trajectories), these secondary particles are believed to be  $\delta$ -electrons. To investigate this, a FNTD was irradiated with Beta-particles from a Sr/Y-90 source (see subsection 3.2.3). The fluence was in the order of  $7 \cdot 10^7 \text{ cm}^{-2}$ . An image of the Beta-irradiated FNTD with standard microscope settings can be seen in Figure 4.27. Primary electrons are hard to identify because they have a LET too low to leave distinct tracks and large angular deflections handicap the tracking of electrons through the FNTD. However, secondary electrons with a higher LET are clearly visible.

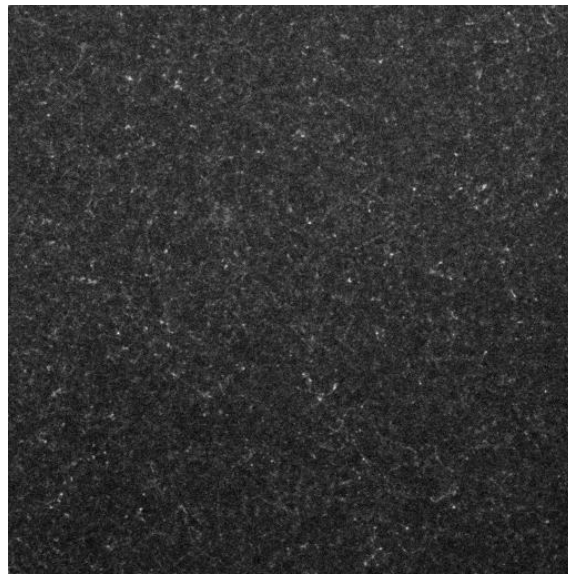


Figure 4.27: FNTD irradiated with Beta-particles from a Sr/Y-90 source. Though hard to track because of the low LET and the curling trajectories, single electron pathways can be seen.

### 4.5.2 Alpha particles

Alpha particles emitted from a Americium-241 source (see subsection 3.2.4) can be seen in Figure 4.28. Because the dimensions of the source are finite, the alpha tracks exhibit an angular spread and are not colinear. Although the space between source and FNTD was evacuated, the geometry of source size, FNTD size and the distance between did not allow for collimation. Non-colinearity causes the tracks to look ellipsoidal due to the non-pointlike focal spot of the microscope (see section 2.2). The divergence is made evident in Figure 4.29, where a 3D view of an image stack is presented.

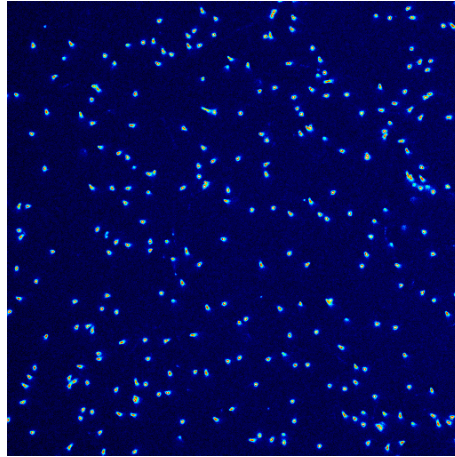


Figure 4.28: Alpha particles. Ellipsiodity of the tracks is due to the divergence of the particles.

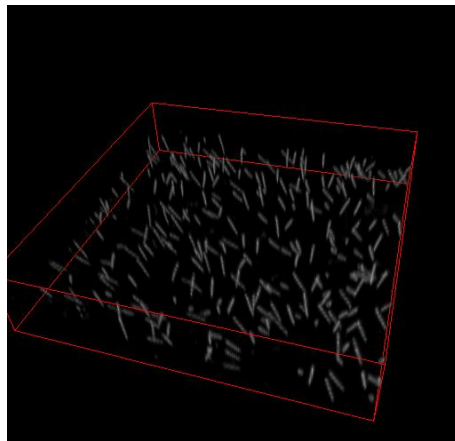


Figure 4.29: Non-collinearity of alpha particles emitted from a finite source in 3d view of an image stack

### 4.5.3 Carbon ions

#### Setup: grazing carbon ion tracks

To produce grazing tracks of carbon ions, FNTDs were lied flat on a PMMA plate of .5 cm thickness. One detector was placed in the entrance channel, another one behind 12 cm of PMMA (density:  $\varrho = 1.19 \text{ g/cm}^3$ ) corresponding to  $12 \text{ cm} \cdot 1.19 = 14.28 \text{ cm}$  (neglecting stopping power ratio effects). This is about the Bragg peak region of the carbon ions initially accelerated to 270.55 MeV/u. A schematic of the setup can be seen in Figure 4.30.

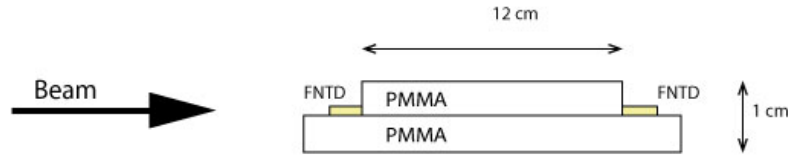


Figure 4.30: Setup for the imaging of grazing carbon ion tracks

#### Results: grazing carbon ion tracks

Here, FNTD imaging capabilities are used to point out qualitative features of irradiation with heavy charged particles. A stopping carbon ion can be seen in Figure 4.31a. Because of the sharp stop, it can be excluded that the ion merely leaves the focal plane of the microscope. In Figure 4.31b, a stack around the plane of Figure 4.31a is maximum projected to show how misleading images can be. One can see in the images, how the range of the secondary electrons is reduced for lower kinetic energies of the HCP projectiles. The stopping ion track shows no release of distinct electron tracks and the carbon ion tracks at the left and right border of Figure 4.31b show only short range  $\delta$ -electrons. A fragmentation can be seen in Figure 4.32. The direction of the projectile can easily be deduced from the forward scattering of the fragments. Light fragments and the deflected remainder of the projectile HCP can be differentiated by the ionization density in the tracks. Also clearly visible are the stochastic nature of the energy transfer of the primary particle and the  $\delta$ -electrons emitted from the HCP tracks. The Bragg peaks of the  $\delta$ -electrons can also be observed, as blobs at the end of the electron trajectories.

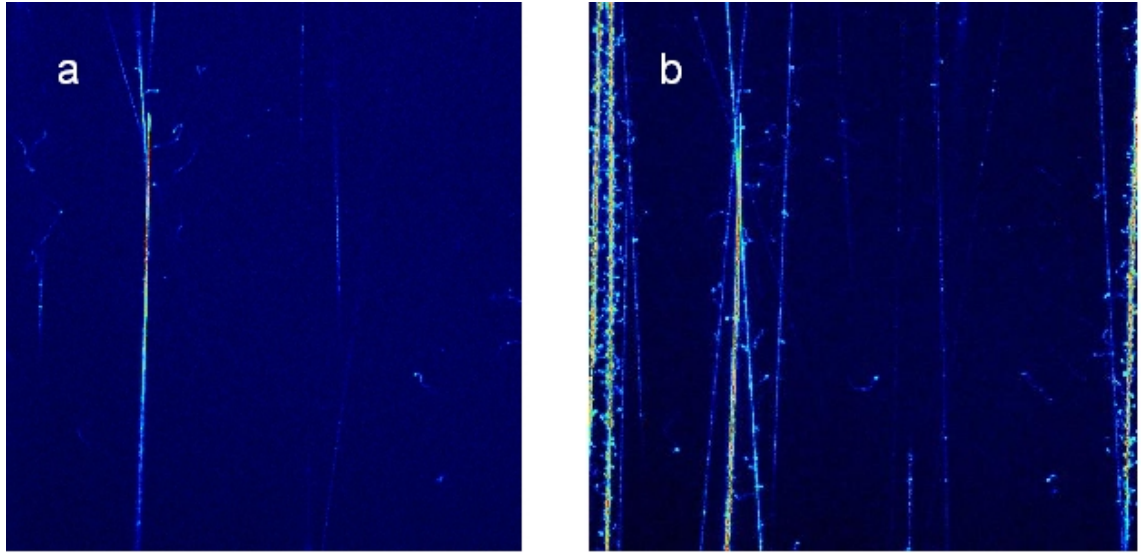


Figure 4.31: a) Image of a stopping carbon ion. b) Maximum projected image stack of 52 slices over 12.48  $\mu\text{m}$  of the same stopping carbon ion

#### Setup: carbon ions, frontal irradiation

Detectors were attached to a  $30 \times 30 \text{ cm}^2$ , 1 cm thick PMMA plate using double-sided adhesive tape. Positions were chosen on a 5 cm grid, avoiding direct neighborhood resulting in a minimal distance of the positions of about  $\sqrt{5^2 + 5^2} \approx 7 \text{ cm}$ . A sheet of paper was attached over the detectors as protective cover. Single spots of carbon ions were shot at the detectors. Kinetic energy of the carbon ions was 270.55 MeV per nucleon. From the available spot sizes, the largest one was chosen in order to have a sufficient homogeneity. The number of particles per spot were calculated to yield  $10^6$  particles per  $\text{cm}^2$  which is equal to 100 tracks per  $100 \times 100 \mu\text{m}^2$ , resulting in a sufficient density of tracks while averting track overlapping. The carbon ion beam had a full width half maximum (FWHM, equal to  $2\sqrt{2\ln 2}\sigma$  for Gaussian distributions) of 10.1 mm. Assumption for the calculation of the particle number per spot was a perfectly symmetric 2D-Gaussian distribution. Calculation lead to  $1.16 \cdot 10^6$  carbon ions per spot. Irradiation was performed without the use of a ripple filter, in the lowest intensity available, i.e.  $5 \cdot 10^6$  carbon ions per second.

#### Results: carbon ions, frontal irradiation

By maximum projecting a stack of images with 270 MeV/u carbon ions, the thin curling tracks of secondary electrons are made visible in Figure 4.33b.



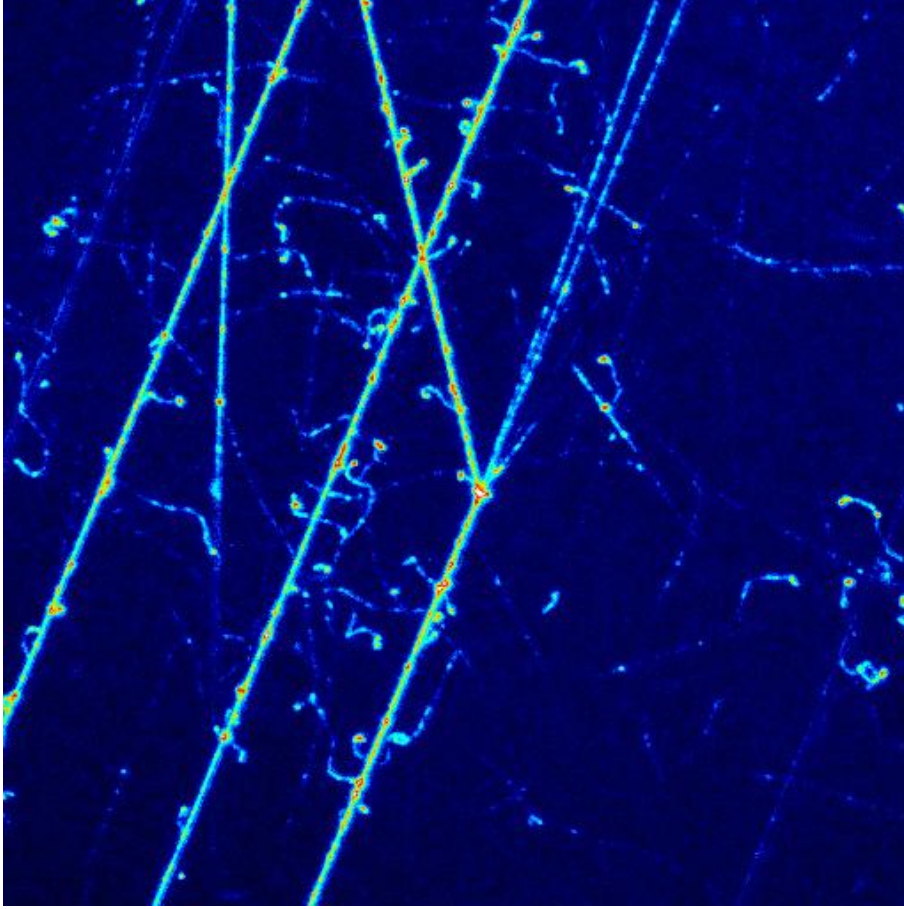


Figure 4.32: 270 MeV/u carbon ion fragmentation. Also,  $\delta$ -electrons are clearly visible. Image is a maximum projected stack of 13 slices,  $67.48 \times 67.48 \mu\text{m}^2$

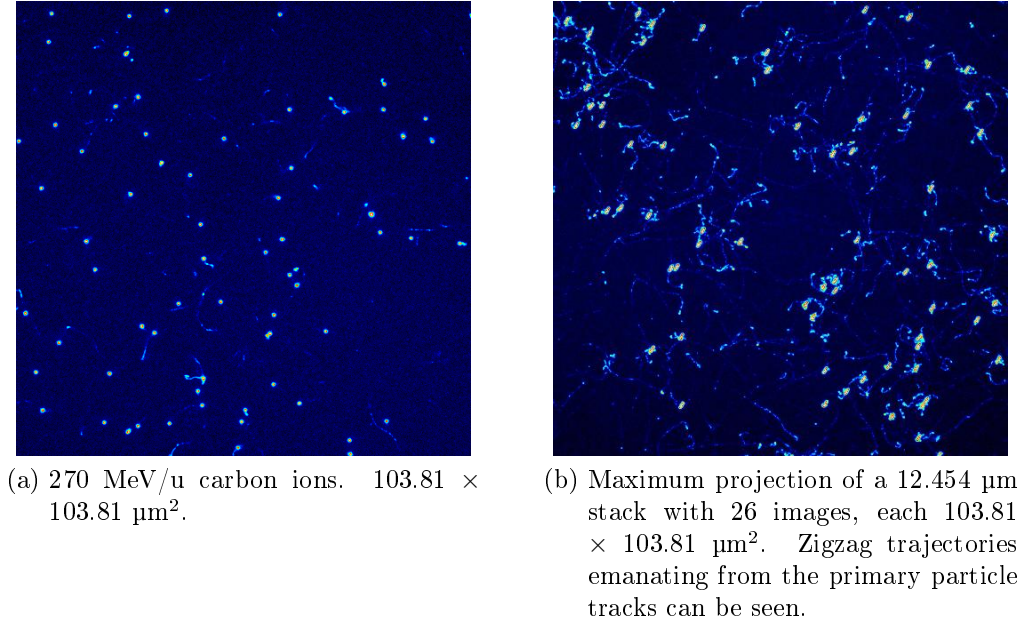


Figure 4.33

#### 4.5.4 Protons

##### Setup: protons

The setup for the proton irradiation is described in subsection 4.5.3. Kinetic energy of the protons was 142.66 MeV, the focus size of the proton beam was 15.2 mm FWHM. Calculation yielded  $2.62 \cdot 10^6$  protons per spot. The intensity used was  $2 \cdot 10^8$  protons per second.

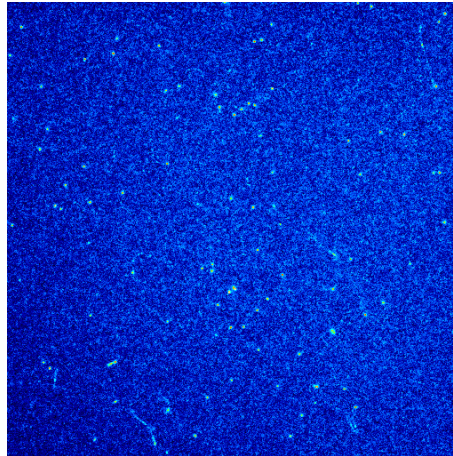


Figure 4.34: 142 MeV protons

### 4.5.5 Antiprotons

#### Setup: antiprotons

Detectors were attached to a PMMA holding device using Scotch<sup>TM</sup> adhesive tape. Orientation was chosen so that for each position (bragg peak and entrance channel) one detector's front surface was placed parallel and one perpendicular to the beam. Because neither spot size nor the number of particles per spot could be adjusted, the detectors had to be positioned off-axis in order to have low enough fluence to reduce track overlapping. In Figure 4.35, one can see the setup of attachment: FNTDs were placed  $\approx 2$  cm apart, the beam was directed between them. This distance was calculated based on the assumption of  $2.5 \cdot 10^7$  particles per spot and a  $\sigma$  of 7 mm. The displacement of the beam in y-direction was not corrected for.



Figure 4.35: FNTDs attached to a holding device for irradiation with antiprotons

For the detectors parallel to the beam, the 6 mm long side was oriented along the beam axis in order to have a longer range to follow tracks. This lead to the fact that the middle of the detectors for one beam position (peak/entrance channel) was displaced around half of the length of a FNTD, that is 3 mm.

#### Results: antiprotons

In Figure 4.36, antiproton tracks from the entrance channel can be seen, recorded perpendicular to the beam. Stray shots, not observable to this extend in proton beams can be seen. Because the difference in the kinetic energy between protons and antiprotons gives no explanation, it is suggested that the stray shots are tracks of pions produced mostly in the Bragg peak or in in-flight annihilations. In the Bragg peak (Figure 4.37), the abundance of stray shot particle tracks is considerably increased, presumably due to the vicinity of the annihilation vertices.

An antiproton coming to rest in the Bragg peak region and annihilating in the FNTD can be seen in Figure 4.38. Due to the evasion of annihilation products in all three dimensions, an image stack was maximum projected.

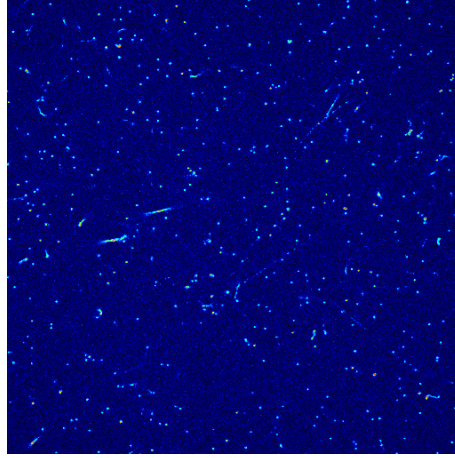


Figure 4.36: 127 MeV antiprotons. Stray shots from pions can be seen. Pions are produced both in the Bragg peak and—to less extend—in in-flight annihilations. Standard microscope settings.

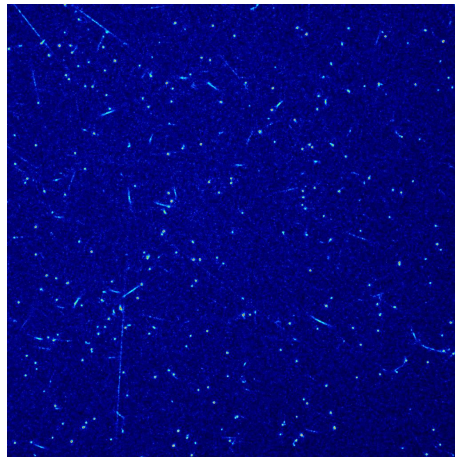


Figure 4.37: Image of antiproton tracks in the Bragg peak. In comparison to the entrance channel, the abundance of stray shots is increased.

## 4.6 Lateral beam quality change

### 4.6.1 Setup: lateral beam quality change

Light nuclear fragments and protons produced in nuclear reactions exhibit an increased lateral spreading in comparison to the primary particle beam due to the smaller mass. Proximal to the Bragg peak, in the central beam axis, the abundance of nuclear fragments is small in comparison to the primary particles. In order to investigate beam quality changes in lateral distance from the beam axis, a 430 MeV/u carbon ion beam was slowed down to 89 MeV/u by traversal of 24.8 cm of PMMA. The beam focus size was 3.4 mm FWHM. A single spot was delivered to the isocenter and FNTDs were attached to a  $30 \times 30 \text{ cm}^2$ , 1 cm thick PMMA plate by adhesive tape. Position of the FNTDs was 0, 6, 12 and 18 mm of the beam axis. The measurements were conducted for  $10^6$ ,  $10^7$  and  $10^8$  particles per  $\text{cm}^2$  in the spot peak to ensure enough tracks at the off-beam positions.

To estimate the spread of the carbon ion beam and of the protons produced in collisions a simple, analytical simulation was written in R (“11 - halo simulation.R”). For the carbon beam simulation, the initial beam was taken as monoenergetic and laterally perfectly gaussian. The range–energy relation was approximated by the power law for protons (see subsection 2.1.3) and the  $A/Z^2$  scaling. The power law is valid only for water—however, the  $\alpha$  coefficient has a known rough dependency on the material ( $\alpha \propto \sqrt{\bar{A}}/\rho$ , where  $\bar{A}$  is the mean atomic number and  $\rho$  the density). For PMMA, the difference in the coefficient adds up to 3.3 %. Fluence reduction with increasing penetration depth was approximated to be linear and not exponential. This approximation is motivated by the linear fluence reduction approximation done by [Bortfeld \(1997\)](#) for protons. It is ok for 270 MeV/u carbon ions but is a rough estimation for 430 MeV/u carbon ions. The coefficient for the linear fluence reduction was taken from TRiP data. Lateral beam spread was approximated as widening of a 2D-gaussian with standard deviation taken from the formula of the lateral scattering radius given in subsection 2.1.3. Because this formula gives only the spread at the end of the range for a given initial energy, a simple calculation was necessary to get the spread as a function of depth for a given initial energy. In this relation, again, the  $A/Z^2$ -scaled power law was used. The simulation of the relative fluence of a carbon ion beam can be seen in Figure 4.39a and logarithmically in Figure 4.39b. The normalization is such that the 2D integral over the initial beam profile is 1 (carbon ion).

For the proton beam halo, every node on the primary beam axis contributes a kernel. Each kernel is calculated with the same approximations as the carbon ion beam. The lateral width of each kernel consists of a pencil beam spreadening and the spread of the carbon ion beam at the corresponding node. Convolution of the two gaussian bell curves is done by  $\sigma^2 = \sigma_{pencil}^2 + \sigma_{primary}^2$ . After calculation, the kernel is weighted with the fluence of the carbon ion beam at the corresponding node in order to take into account the fluence reduction of the primary beam. Only first generation

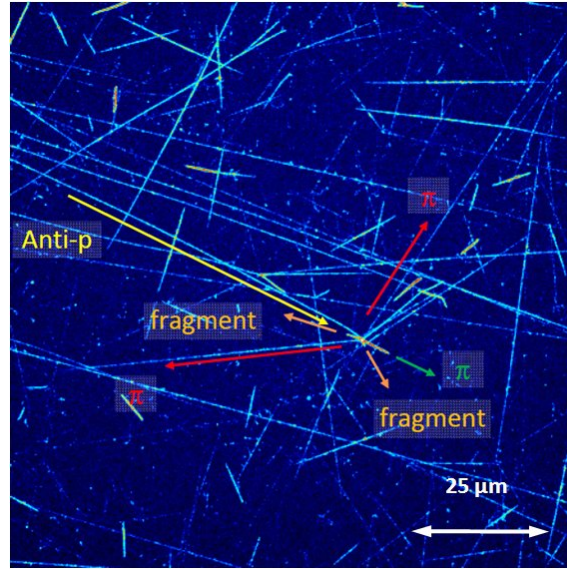
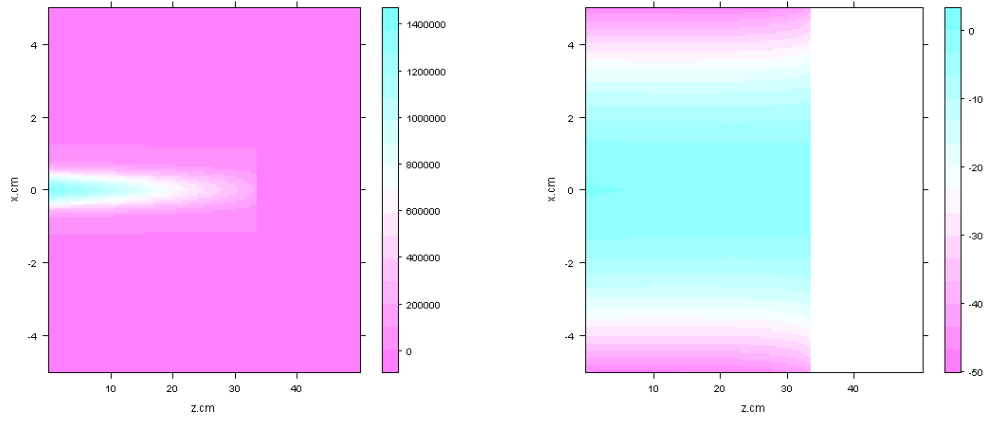


Figure 4.38: Antiproton annihilation event



(a) Simulated carbon ion beam in water, 430 MeV/u

(b) Simulated carbon ion beam in water, 430MeV/u, logarithmic. Note that  $\log(0)$  is displayed as blank and should not be confused with the white from the color key.

Figure 4.39



protons are simulated and their fluence reduction is neglected. Another neglect is that the crosssection for proton production is independent of the primary particle's energy. The normalization of the simulated proton halo is again such that the primary beam is normalized to 1.

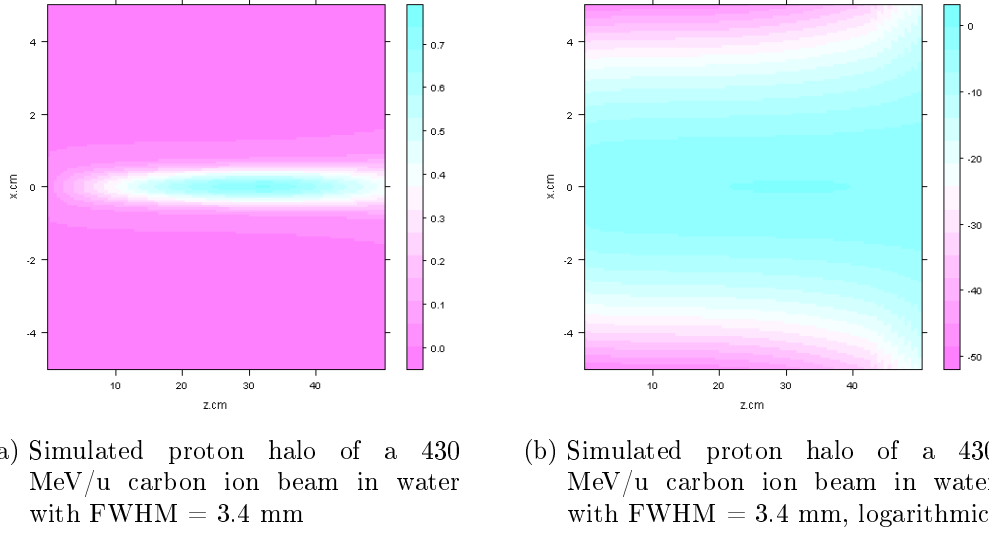


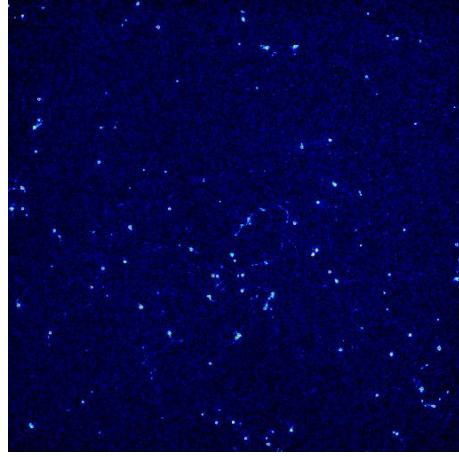
Figure 4.40

### 4.6.2 Results: lateral beam quality change

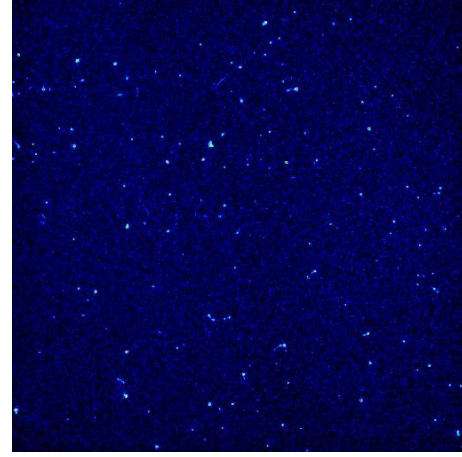
Images of the particle tracks from the different lateral positions can be seen in Figure 4.41. An image of the particle tracks on the on-axis position is shown in Figure 4.41a. Figures 4.41b to 4.41d show the tracks corresponding to the particle spectrum at 6–18 mm off-axis position. It can be seen that the particle tracks show a variation of size and fluorescence. At the outer positions, the particle spectrum seems to be dominated by low-LET radiation like protons.

## 4.7 Radial track profile

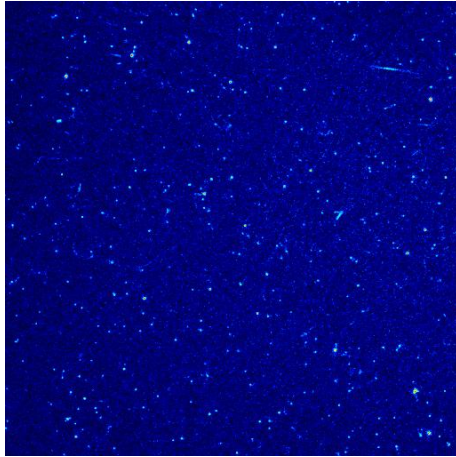
In order to investigate the track structure of carbon ions, the regions around the fluorescence maxima of a  $103.81 \times 103.81 \mu\text{m}^2$ ,  $2048 \times 2048$  pixels image were averaged. Tracks too near to the image border were omitted. In Figure 4.42, the corresponding surface plot is shown. Correction for intensity variations and background signal were adjusted to the image size by scaling the size of the structures to be filtered by the Fourier band pass filter. Structures of 256 pixels in  $512 \times 512$  pixels images correspond to structures of 1024 pixels in  $2048 \times 2048$  pixels images. The radial fluorescence distribution is shown in Figure 4.43.



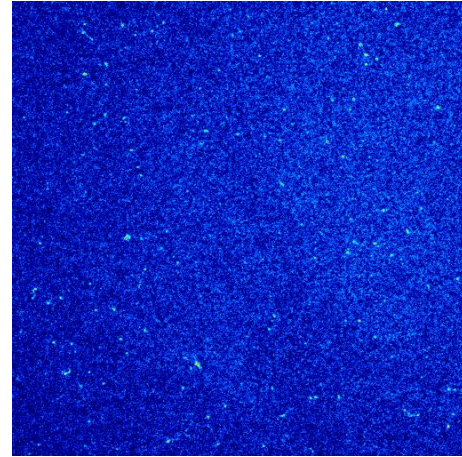
(a) The FNTD was placed on the beam axis. Fluence of  $10^6 \text{ cm}^{-2}$  in the middle of the spot.



(b) FNTD position: 6 mm off the beam axis. Fluence of  $10^7 \text{ cm}^{-2}$  in the middle of the spot.



(c) FNTD position: 12 mm off the beam axis. Fluence of  $10^8 \text{ cm}^{-2}$  in the middle of the spot.



(d) FNTD position: 18 mm off the beam axis. Fluence of  $10^8 \text{ cm}^{-2}$  in the middle of the spot.

Figure 4.41: Tracks of the particle spectrum of a 430 MeV/u carbon ion beam after traversal of 24.8 cm PMMA for different lateral distances from the beam axis. FWHM of the beam was 3.4 mm. Standard microscope settings.



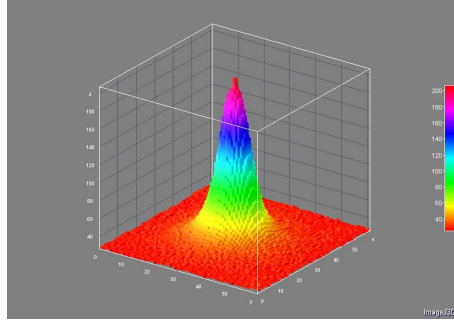


Figure 4.42: Carbon ion track, 270 MeV/u, average from 60 tracks

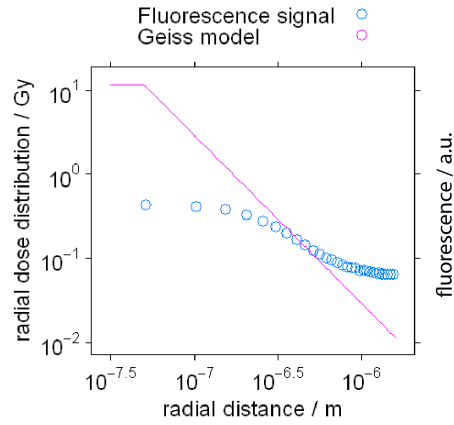


Figure 4.43: Radial fluorescence signal obtained from the data of Figure 4.42. For comparison, a Geiss model 270 MeV/u carbon ion track with  $r_{core} = 50$  nm is displayed. The datapoint from  $r = 0$  is put to a quarter of the pixel size, i.e. half the distance from the middle to the boundary of the  $r = 0$  pixel.

## 4.8 Fluence measurements

### 4.8.1 Setup: fluence measurements

Fluence measurements were conducted using the PTW PMMA slab phantom T2967. FNTDs were attached to a  $30 \times 30 \text{ cm}^2$  PMMA plate of 1.0 cm thickness with a horizontal deepening of .5 mm depth and 4 mm width using scotch<sup>TM</sup>tape. Orientation lines engraved into the holding plate helped to align the setup to the positioning laser. For the fluence measurements, no slabs were inserted into the beam upstream of the detector. The setup can be seen in Figure 4.44.

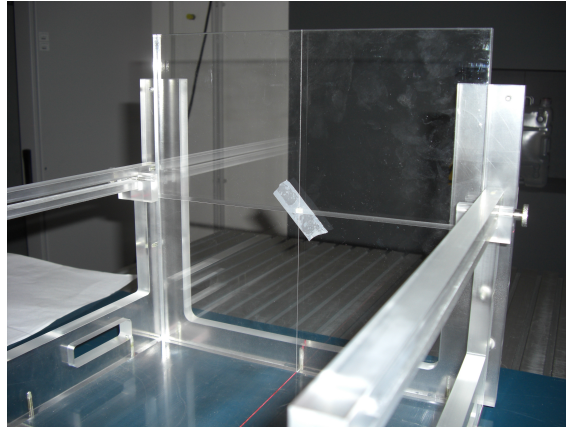


Figure 4.44: Setup of the fluence measurement. FNTD attached by adhesive tape to a PMMA plate.

Radiation fields included

- a  $4 \times 4 \text{ cm}^2$ , 142.66 MeV proton field with 2 mm spacing between 15.2 mm FWHM spots of 40086 protons each
- a  $4 \times 4 \text{ cm}^2$ , 270.55 MeV carbon ion field with 5 mm spacing between 10.1 mm FWHM spots of 500088 carbon ions each
- a  $4 \times 4 \text{ cm}^2$ , 430.10 MeV carbon ion field with 4 mm spacing between 9.8 mm FWHM spots of 319976 carbon ions each

The amount of particles per spot was calculated to yield a fluence of  $10^6 \text{ cm}^{-2}$  for protons and  $2 \cdot 10^6 \text{ cm}^{-2}$  for carbon ions. Also, simulations using R, superpositioning analytical Gaussian functions parameterized to represent the beam spots showed good homogeneity. These numbers were used as input for irradiation plans. For the carbon ion measurement, a ripple filter was inserted in the beam.

### 4.8.2 Results: fluence measurements

Fluence measurements were carried out using the *find maxima* routine included in ImageJ. The routine has a free parameter “noise tolerance” which enables the user to

Table 4.2: Fluence measurements. Measured number of local maxima vs. the number of tracks expected from the accelerator input  $\pm$  the poisson error and the deviation of the measurement in relation to the expectation.

particle type	kinetic energy	measured	expected	deviation
p	142.66 MeV/u	1588	$1724 \pm 42$	-7.9 %
C-12	270.55 MeV/u	3282	$3448 \pm 59$	-4.8 %
C-12	430.10 MeV/u	3046	$3448 \pm 59$	-11.7 %

define how much the peaks counted as local maxima have to tower above the noise. 4 % inhomogeneity is guaranteed from HIT. The expectation value  $\mu$  of a Poisson distribution with  $\Delta\mu/\mu = 4\%$  error can be calculated via  $0.04^{-2} = 625$ . To have the error contribution from track counting smaller than the error contribution from the accelerator output, an area of  $4 \times 4$  tiles of  $103.81 \times 103.81 \mu\text{m}^2$ , in the case of  $10^6 \text{ cm}^{-2}$  particles corresponding to  $\approx 170000$  tracks was imaged.

First, an additionally acquired single  $103.81 \times 103.81 \mu\text{m}^2$  image was subjected to the *find maxima* routine. The noise tolerance parameter was manually adjusted to just barely assign a local maximum to each track visible on the single image. Manual adjustment is relatively easy due to the preview option, marking each found local maximum in the image for a given noise tolerance value. Then the found noise parameter was applied to the  $4 \times 4$  tiles. The results can be seen in table 4.2.

Deviations were calculated from ideally expected fluences of  $10^6 \text{ cm}^{-2}$  for protons and  $2 \cdot 10^6 \text{ cm}^{-2}$  for carbon ions, corresponding to 1724 maxima for protons and 3448 maxima for carbon ions within an area of  $16 \cdot 103.81 \times 103.81 \mu\text{m}^2$ .

## 4.9 Beam quality measurement by fluorescence frequency distribution

A proton, a carbon ion and an alpha particle image corrected with the procedure described above is shown in Figure 4.46, 4.48 and 4.50, respectively. The corresponding background signals are displayed in Figures 4.47, 4.49 and 4.51. In Figure 4.45, the fluorescence frequency distribution is shown, a binned version is shown in Figure 4.52. The images used have a different number of particle tracks, Figure 4.53 shows the fluence corrected histogram. Both histograms are binned with a bin width of 5 counts for improved clarity. Fluence was obtained by the *find maxima* routine of ImageJ using the preview option.

It has to be kept in mind that the alpha particles were emitted from a source of finite dimensions which leads to non-colinear particle tracks, i.e. the particle traversals through the detector are not perpendicular to the surface and the focal plane of the microscope. Thus, firstly the alpha particle tracks imaged are not circular but ellipsoid and secondly the amount of  $\text{Al}_2\text{O}_3\text{:C,Mg}$  traversed up to the read-out plane

differs from track to track depending on the angle from the z-axis. Non-colinearity matters due to the non-sphericity of the microscope focal spot. The amount of traversed  $\text{Al}_2\text{O}_3\text{:C,Mg}$  matters because the plane read-out in is only a small margin away from the range of the alpha particles, and hence LET changes are large. The non-colinearity of the alpha particle tracks is demonstrated in Figure [4.29](#).

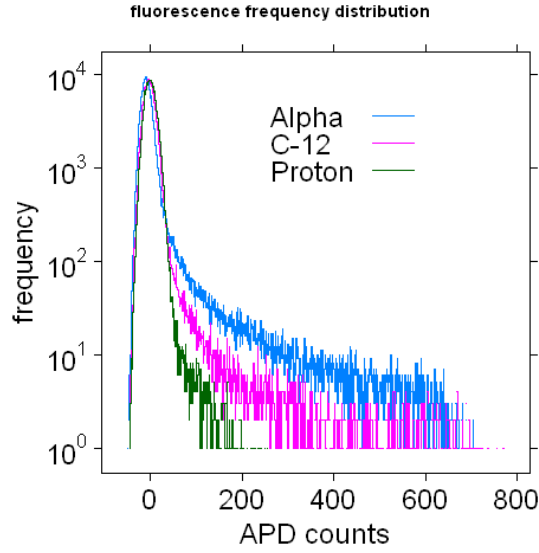


Figure 4.45: Fluorescence frequency distribution. Images background corrected.

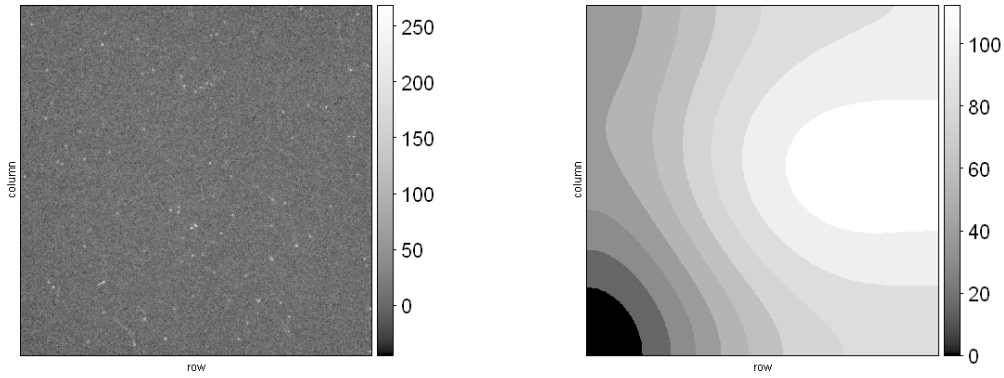


Figure 4.46: 142.66 MeV proton tracks, Figure 4.47: Background signal distribution of Figure 4.46  
 $103.81 \times 103.81 \mu\text{m}^2$

## 4.10 Neutron measurements

Neutron dosimetry has been a major application of track detector technology. In order to investigate the potential of FNTDs for neutron dose estimation, off-beam measurements were conducted.

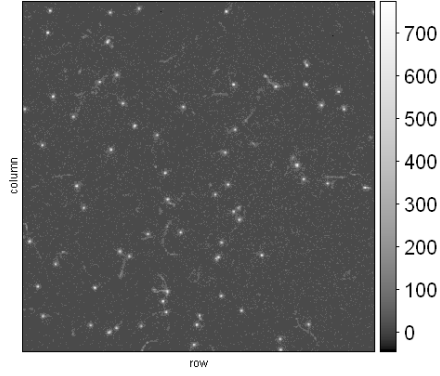


Figure 4.48: 270.55 MeV/u carbon ion tracks,  $103.81 \times 103.81 \mu\text{m}^2$

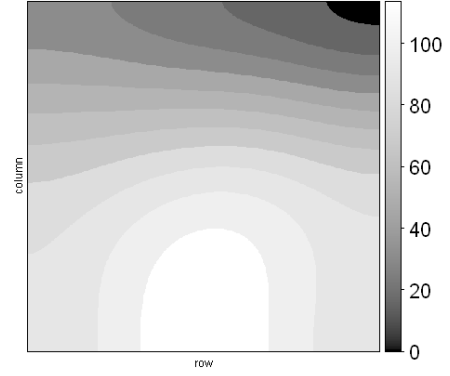


Figure 4.49: Background signal distribution of Figure 4.48

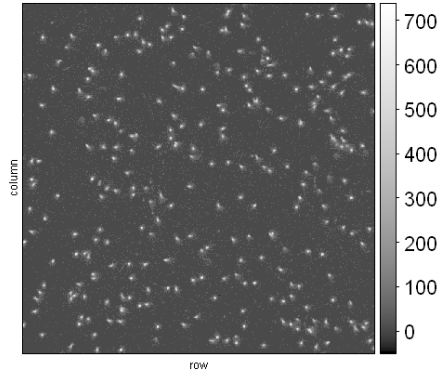


Figure 4.50: 0.7 MeV/u alpha particle tracks,  $103.81 \times 103.81 \mu\text{m}^2$

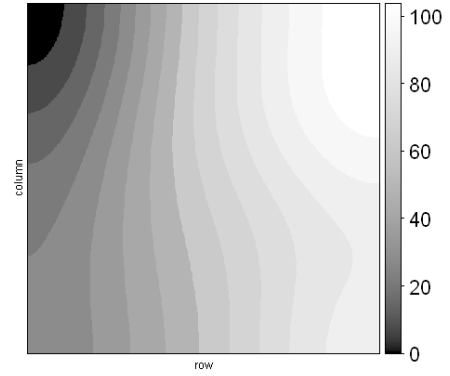


Figure 4.51: Background signal distribution of Figure 4.50

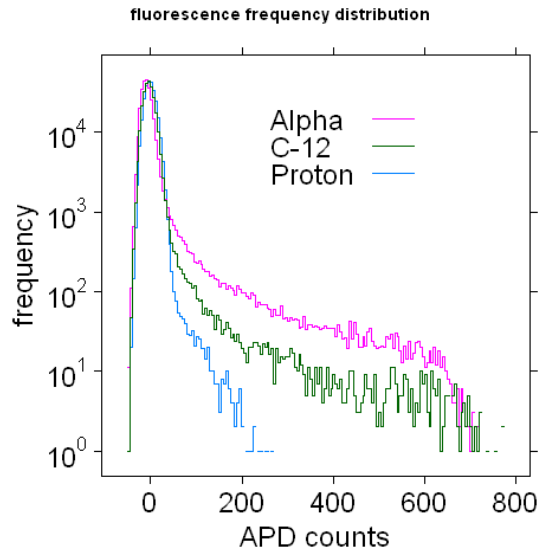


Figure 4.52: Fluorescence frequency distribution of background corrected 142 MeV protons, 270 MeV/u carbon ions, 1.4 MeV alpha particles, bin width of 5 counts

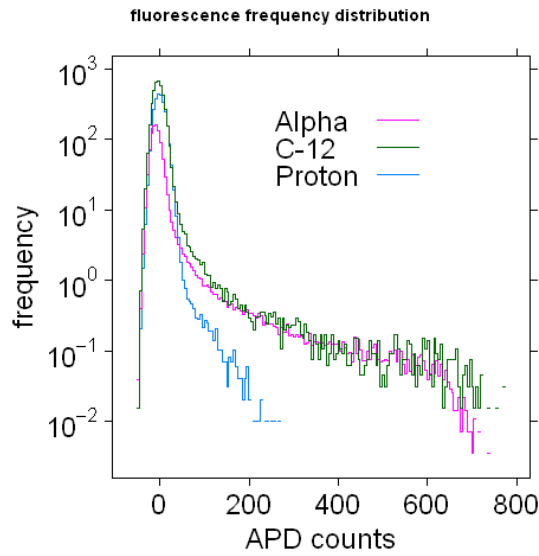


Figure 4.53: Fluence normalized fluorescence frequency distribution of background corrected 142 MeV protons, 270 MeV/u carbon ions, 1.4 MeV alpha particles, bin width of 5 counts

Table 4.3: Off-beam measurement. 430.10 MeV/u carbon ions sent through 24.8 cm PMMA and 88.83 MeV/u carbon ions free in air. The automatically counted fluorescence maxima are listed for different *noise tolerance* (nt) parameter settings of the counting routine.

Initial energy	radiator	nt = 80	nt = 100	nt = 120
430.10 MeV/u	y	77	53	46
430.10 MeV/u	n	84	58	49
88.83 MeV/u	y	250	144	92
88.83 MeV/u	n	176	104	57

#### 4.10.1 Setup: neutron measurements

To realize sufficient neutron production, a 430.10 MeV/u carbon ion beam with  $\text{FWHM} = 3.4$  mm was sent through 24.8 cm of PMMA. For comparison, also a 88.83 MeV/u carbon ion beam with  $\text{FWHM} = 9.8$  mm free in air was delivered. For both modalities, the a spot of  $10^9$  carbon ions was directed 10 cm away from the isocenter so that no primary particles or charged fragments reach the FNTDs. These were placed in the isocenter, attached to a  $30 \times 30$  cm<sup>2</sup> PMMA plate of 1.0 cm thickness using adhesive tape. For each modality, one measurement was conducted with the FNTD covered only by the attaching adhesive tape and another one with an additional polyethylen (PE) foil placed before the FNTD as a radiator. PE is rich in hydrogen and recoil protons released by neutron radiation cause tracks in FNTDs (Sykora et al. 2007, 2008b).

#### 4.10.2 Results: neutron measurements

Because of the low fluence,  $4 \times 4$  tiles each with  $103.81 \times 103.81$   $\mu\text{m}^2$ ,  $512 \times 512$  pixels were imaged. For different *noise tolerance* (nt) parameter values, local maxima were counted automatically (see Table 4.3). The parameter setting was varied due to the differences in the LET of the off-beam mixed particle field which inhibits an optimized adjustment. Variation of the nt parameter was in the region suitable for 142 MeV proton fluorescence maxima.

In the case of 430.10 MeV/u, our measurement yielded no difference in the off-beam particle fluence between use and non-use of the radiator. Poissonian error estimation of the fluence shot noise gives e.g.  $77 + \sqrt{77} > 84$  for the noise tolerance = 80 case. For 88.83 MeV/u on the other hand, there are consistently more local maxima counted with the radiator than without. Also consistently with and without the radiator, there are more maxima for the 88.83 MeV/u case than for the 430.10 MeV/u one.



# Chapter 5

## Discussion & Outlook

### 5.1 Literature review

After  $\text{Al}_2\text{O}_3:\text{C,Mg}$  was introduced as volumetric optical data storage (Akselrod et al. 2003) and its optical properties (absorption and excitation/emission spectra, fluorescence quantum yield, anisotropy and emission polarization) were thoroughly investigated (Sanyal and Akselrod 2005), application as nuclear track detector was proposed (Akselrod et al. 2006a). In this proposal, a confocal setup was presented and dependence on the doping concentration of the track fluorescence (290 MeV/u carbon ions) was shown as well as different peak fluorescence for different LETs (down to  $LET_\infty$  in water 0.5 keV/ $\mu\text{m}$ ). Nearly 100 % fluence detection was reported for 31 keV/ $\mu\text{m}$  Ne-20 ions. Thermal stability up to 600 °C and the non-destructiveness of the readout were shown in (Akselrod and Akselrod 2006). Detection of thermal neutrons using radiators made from  $^6\text{LiF}$  and  $^7\text{LiF}$  TLDs yielded a track density of 6100 vs. 670  $\text{mm}^{-2} \text{mSv}^{-1}$  whereas detection of fast neutrons from a AmBe source with a PE radiator yielded 21 tracks  $\text{mm}^{-2} \text{mSv}^{-1}$  (Akselrod et al. 2006b). This was confirmed in (Sykora et al. 2007) where a comparison with CR-39 plastic nuclear tracks detectors (12.1 tracks  $\text{mm}^{-2} \text{mSv}^{-1}$ ) was done and different radiators were tested (LiF, PE,  $^{10}\text{B}$ -loaded Teflon; in air and albedo configuration). The dependence of the fast neutron response on the incident angle and the reusability after thermal annealing to 680 °C was investigated in (Sykora et al. 2008b). No saturation in the track fluorescence amplitude plotted against  $Z/\beta$  was observed for a  $LET_\infty$  in water of 8767 keV/ $\mu\text{m}$  (Sykora et al. 2008a). Here,  $Z$  is the effective charge of the HCP. In (Sykora and Akselrod 2010b), a data processing method was developed to increase the dynamic range of gamma/x-ray response which is desirable for neutron/gamma separation at high gamma doses. Accounting for overlapping tracks, they extend the linear neutron dose response by two orders of magnitude, making the saturation dose 1000 times larger than for CR-39.

## 5.2 Background

### 5.2.1 Nature of the background signal

The investigation of the fluorescence measured from an unirradiated FNTD was crucial for establishing a correction protocol dealing with microscope-caused variations in the signal.

Large-scale variations can be seen in Figure 4.7a. This is due to spatial inhomogeneities in the read-out process caused by the scanning optics. Within the area reachable by the scanning mirrors, the detected background signal decreases with increasing distance from the central optical axis.

Track-shaped maxima visible in Figures 4.8, 4.7a and 4.9 might be caused by environmental radiation.

As can be seen in Figure 4.11, the shape of the frequency distribution is well described by a Gaussian. This allows for the definition of a mean background signal being useful and applicable for subtraction. The background signal being fitted to is not corrected for illumination variations because the background itself is the illumination correction for the particle irradiations.

The measurements of the relative background signal in Figure 4.12 and the relative track signal in Figure 4.13 show very similar patterns and values. This justifies the pixelwise scaling of images as used in the correction applied in sections 4.7 and 4.9.

### 5.2.2 Behavior of the background signal

The background signal as a function of depth and time was investigated in section 4.3.2. A peak in the fluorescence yield about  $\approx 15 \mu\text{m}$  from the FNTD surface is observed and proposed for optimal readout depth.

Temporal stability was demonstrated with a series of subsequent images for a timeframe of 4 min. This stability and the constancy of the signal after 120 readouts allows to regard the subsequent readouts independent from each other (i.e. optical bleaching by 2-photon absorptions is negligible), so that the dataset of the image series can be used to show significant deviations between different pixels. Because of this, the correction procedure for the microscope sensitivity as the largest contributor to signal variations (15–20 %, see section 4.2) has to be applied. However, there is no correction for doping inhomogeneities available yet.

### 5.2.3 Signal correction

Three signal correction methods have been presented. The most reliable and easy to use method of FFT band pass filtering is proposed. The local background assessment method, however, has potential superiority. Its resolution can be increased if the tiling is not done seamlessly but staggered. Pitch of 1 pixel is possible. The size of the detail being histogrammed and fitted to can be adjusted to the particle fluence

delivered. This means that for low fluences, smaller details could be used and for high fluences the detail size can be chosen to gather enough data for the fit routine.

After the sensitivity correction, the background subtraction of particle radiation images can be further improved, if not the mean value is subtracted but the background peak obtained from a fit. For low count numbers however, the procedure of inferring from the APD reading to the actual photon counts collapses and yields negative count values. A more appropriate—however time consuming—scheme that could be used employing Bayesian statistics was presented in (Greulich et al. 2006).

## 5.3 Response to gamma radiation

A FNTD x-ray response curve has been published by Sykora and Akselrod (2010b), showing saturation for 40 kV x-rays at  $H_p(10) \approx 20\text{-}30$  Sv. In Figure 4.25 no saturating behavior was observed for 20 Gy in water from 6 MV photons. The saturation limit for the microscope used in this thesis may be higher due to the higher spatial resolution. Still, saturation at higher doses cannot be ruled out from the data.

Sykora and Akselrod stated that “Tracks of individual secondary (or delta) electrons are in general invisible because of their low ionization density”. In this thesis, however, an increase of the density of single, small maxima of fluorescence can be seen (Figure 4.26). Because the density is steadily increasing with increasing absorbed dose, single secondary electrons are assumed to cause the maxima thus identified as electron tracks.

## 5.4 Imaging of particle tracks

The aim of the qualitative imaging was to illustrate the sensitivity and the possibilities for particle spectroscopy by demonstrating different particle track morphologies. In comparison to Figure 4.27, morphologically similar tracks are visible in Figure 4.33b. The curling and deflections of the electrons visible in Figures 4.33b and 4.32 cannot be seen in Figure 4.27, because Figures 4.33b and 4.32 are both projections of several images of a stack, whereas Figure 4.27 is a single image and thus only trajectories, deflections taking place in this plane are observable. The reported FNTD threshold for track detection is a LET in water of  $0.5\text{ keV}/\mu\text{m}$  (Akselrod et al. 2006a). However, the  $LET_{100\text{eV}}$  in water of 2 MeV electrons is  $0.102\text{ keV}/\mu\text{m}$  and of 0.5 MeV electrons  $0.117\text{ keV}/\mu\text{m}$ . This means either a significant improvement of the LET sensitivity range with our setup or that the tracks visible after Sr/Y-90 beta irradiation are not the primary tracks but the secondary “knock-out” electrons that exhibit a larger LET.

In Figure 4.31a, HCP tracks seem to be originating in the stopping carbon ion’s trajectory. However, as can be seen from Figure 4.31b, there is no fragmentation vertex observable. To the contrary, the tracks are from particles produced or deflected more upstream.

An actual fragmentation vertex can be seen in Figure 4.32. Furthermore, this figure features imaging of secondary electron Bragg peaks.

## 5.5 Lateral beam quality change

First investigations on lateral beam quality change show the potential of FNTDs to resolve the increased out-scattering of light fragments from the beam axis. Size and fluorescence amplitude indicate the particle spectrum in the penumbra to be dominated by low-LET particles like protons. Thorough evaluation would include a normalization concerning the number of primary particles in the beam spot, an application of the correction procedure established in subsection 4.3.3 and a normalization of the measured fluence.

## 5.6 Radial track profiles

The radial fluorescence signal of a mean carbon ion track in Figure 4.43 shows about the expected  $r^{-2}$  behavior for  $r > 10^{-6.5} \text{ m} = 320 \text{ nm}$ . The signal for radial distances under this limit is blurred due to the size of the focal spot and also quenched. For comparison, a simulated radial dose distribution (RDD) is plotted. 640 nm corresponding to the diameter for the radial distance limit is almost the wavelength of the illumination laser, so blurring due to the finite illumination and detection is very plausible. However, microscopy techniques that overcome the resolution limit imposed by diffraction (e.g. stimulated emission depletion microscopy, STED) are anticipated to give improved results (cf. Rittweger et al. 2009).

## 5.7 Fluence measurements

The fluence measurements of FNTDs in combination with automatic track counting showed deviations of up to 11 % from the expectation value. The Poisson error of the expectation value was about 2.4 % for all particle energies. Homogeneity up to deviations of 4 % is guaranteed from the beam delivery system. The sensitivity of FNTDs shown in particle track imaging, however, makes it hard to believe that HCPs might traverse FNTDs without leaving a track. Also, nearly 100 % detection efficiency was reported for 31 keV/ $\mu\text{m}$  Ne-20 ions (Akselrod et al. 2006a). Therefore, we think that deviations originate from beam spots being too far from each other. The spacing of the beam spots was chosen under the boundary condition of a fluence low enough to prevent overlapping tracks, and at the same time  $\geq$  particles per spot than the minimum number. Although simulations with analytical Gaussian fluence distributions for the beam spots indicated the distance between spots to be small enough for the measurement, we conclude with the advise that a future experiment on fluence detection makes use of the possibility to circumvent

the boundary condition on the minimum particle number per spot which is set in place for patient service.

## 5.8 Beam quality measurement by fluorescence frequency distribution

Beam quality measurements were conducted by evaluating the different fluorescence frequency distributions. It was confirmed that high-LET radiation yields a higher local fluorescence signal than low-LET radiation. Different fluences, however, make direct comparison difficult. The down-scaling of the background signal peak in the normalization of the fluorescence frequency distribution to fluence, on the other hand, internalizes this information on fluence. This side-effect of fluence normalization has not been exploited yet.

A further extraction of information from an image is to double-normalize the fluorescence frequency distribution. In this approach, information on the size of the particle tracks is gathered by thresholding and track counting. For different thresholds, the fluorescence distribution per particle track is normalized to the average track size. Because the behavior of the average track size with varying threshold value is based on the radial fluorescence signal, differential effects for different beam qualities are anticipated and were confirmed in preliminary investigations (not shown).

Variation of the stimulation laser intensity might offer another possibility for beam quality determination: Similar to the idea of high dynamic range (HDR) images in photography, where a combination of the information from images with different illumination enhances the dynamic range, here fluorescence yield saturation effects in high local dose regions might result in non-linearities. This non-linear behavior would be dependent on the LET and the radial dose deposition and thus imply information valuable for a future track to particle assignment.

The possibility to readout FNTDs in three dimensions could be of use to extract information on the radiation quality spectrum of mixed particle fields. Fluence averaged LET values could be calculated from images with particle tracks perpendicular to the focal plane and track length averaged LET values from image stacks of the same detector. The assumption that the beam quality does not change within a single focal plane can be considered valid. However, the evaluation of image stacks only yields truly track length averaged LET values for the case that the depth dimension of the stack is much larger than the dimensions of the track segments in which LET variations occur. If this condition is given at all, it would be around the Bragg peak. Still, the measurement of both track length and fluence averaged LET at the same time would be a feature unique to FNTDs with application especially in a future LET-painting hadron therapy.

## 5.9 Neutron measurements

The difference in the particle fluence 10 cm off the beam spot was measured for a 430 MeV/u carbon ion beam traversing 24.8 cm PMMA and a 88.83 MeV/u carbon ion beam traversing air both with and without a PE radiator. The reason why the setup without the range-shifting PMMA yielded more local fluorescence maxima—which are interpreted as particle tracks—is most probably the geometry of the setup: fast neutrons are moderated by the hydrogen-rich PMMA while thermal neutrons are screened.

For the 430 MeV/u setup, no difference was seen with radiator compared to the same setup without a radiator. The radiator consisted of a simple sheet of PE foil—it is possible that several layers or a thicker piece of PE have to be used. Use of high-density PE (HDPE) might additionally improve the setup. And, of course, the number of primary particles can be increased to have more statistically reliable results. The attachment of the FNTDs should preferably not counter the differential effect of radiator use/non-use by adhesive tape covering FNTDs. Furthermore it is possible that the result would be more meaningful if the number of primary particles actually delivered to the beam spot was fixed and not, as done so far, the number of primary particles exiting the beamline.

## 5.10 Summary and suggestions for further investigations

The task of this thesis was to integrate FNTD technology in a life science environment. A readout and correction protocol was established and issues of relevance were addressed: The response to gamma radiation up to 20 Gy in water was measured and no quenching was observed. Sensitivity was shown to be high enough to image single  $\delta$ -electrons from 270 MeV/u carbon ions and the change in beam quality lateral from the beam axis was resolved and qualitatively shown. Fluence measurements were conducted yielding satisfactory results and feasibility studies on beam quality monitoring and neutron halo measurements were conducted. With these investigations, the framework for the application of FNTDs in a medical research field was set.

In the following, an outline for possible further studies is given.

a) based on already acquired image data

- automatization of correction procedures (see section 4.3.3), improvement by using a fit to yield the value to subtract.
- automated correction on image data sets with different illumination power (e.g. comparison of background vs. track fluorescence).

- automated correction on image data sets with different pinhole size (e.g. comparison of background vs. track fluorescence).
  - automated correction on image data sets that are double-normalized as described in section 5.8.
- b) based on already conducted irradiations
- application of non-diffraction-limited microscopy, in particular for imaging of electron Bragg peaks and radial fluorescence distributions
  - readout of FNTDs used in the neutron experiment at shallow depths
- c) continuing the work with data from additional irradiations
- saturation with higher gamma doses
  - fluence measurement without patient service boundary conditions to allow fewer particles per spot in order to decrease the spot distance for the same  $10^6 \text{ cm}^2$  fluence.
  - off-beam measurements of neutrons with more primary particles in the spot and with a dedicated radiator
  - direct colocalisation radiobiology experiments with cells grown on FNTDs (see Figure 5.1)

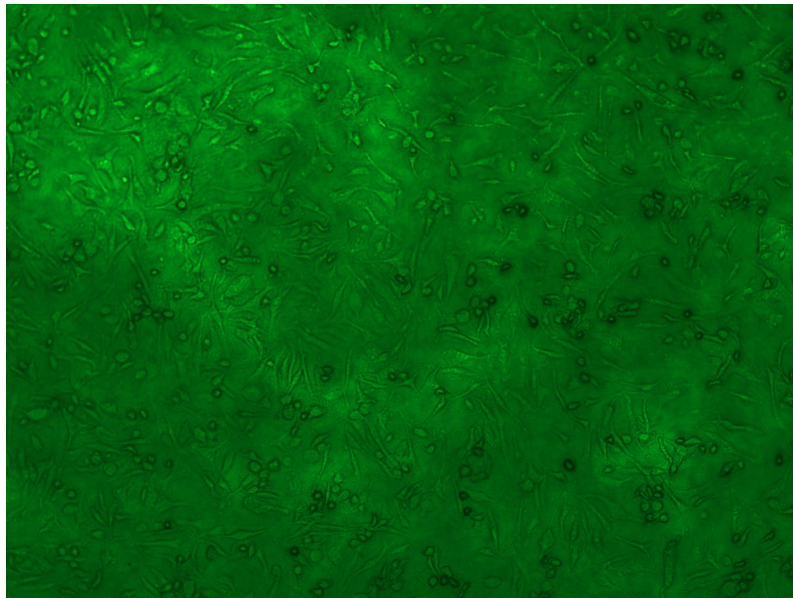


Figure 5.1: Human prostate carcinoma cells grown on a FNTD, imaged through a light microscope. Courtesy of Martin Niklas.





# Part I

## Appendix



# Appendix A

## List of Experiments

Irradiation	Comment	FNTD-ID
P, 142.66, FWHM=15.2 mm, N=2.62E6 particles/spot, no ripple filter		E41-1406
C, 270.55, FWHM=10.1 mm, N=1.16E6, no ripple filter		E41-1409
Co-60, 0.5 Gy in H <sub>2</sub> O, no built-up material, 30 × 30 cm <sup>2</sup> field, 50 cm SSD, parallel to surface		E41-1414
Alpha, Am-241		E41-1401
C, 270.55, FWHM=10.1 mm, N=1.16E6, no ripple filter, parallel to surface		E41-1411
C, 270.55, FWHM=10.1 mm, N=1.16E6, no ripple filter, parallel to surface, behind 12 cm PMMA		E41-1412
Antiprotons, 126 MeV, sigma 6–7 mm, 2–3 10 <sup>7</sup> particles/spill, off-axis, entrance channel		E41-1416
Antiprotons, 126 MeV, sigma 6–7 mm, 2–3 10 <sup>7</sup> particles/spill, off-axis, parallel to surface, entrance channel		E41-1417
Antiprotons, 126 MeV, sigma 6–7 mm, 2–3 10 <sup>7</sup> particles/spill, off-axis, at Bragg peak		E41-1418
Antiprotons, 126 MeV, sigma 6–7 mm, 2–3 10 <sup>7</sup> particles/spill, off-axis, fl., at Bragg peak	Annihilation	E41-1419
Unirradiated	Control	E41-1420
Co-60, 0.01 Gy		γ-1
Co-60, 0.03 Gy		γ-2
Co-60, 0.1 Gy		γ-3
Co-60, 0.3 Gy		γ-4

Appendix A List of Experiments

Co-60, 1 Gy		$\gamma$ -5
6 MV photons, 0.3 Gy		$\gamma$ -6
6 MV photons, 1 Gy		$\gamma$ -7
6 MV photons, 3 Gy		$\gamma$ -8
6 MV photons, 10 Gy		$\gamma$ -9
6 MV photons, 20 Gy		$\gamma$ -10
23 MV photons, 0.5 Gy	Thermally an- nealed prior to irradiation	E41-1403
P, 142.66, FWHM=15.2 mm, $4 \times 4$ cm <sup>2</sup> field, 2 mm spacing, N=40086 (1E6 cm <sup>-2</sup> ), intens. 2E8 /s		9
P, 221.06, FWHM=12.6 mm, $3 \times 3$ cm <sup>2</sup> field, 4 mm spacing, N=15998 (1E6 cm <sup>-2</sup> ), intens. 2E8 /s	Fluence	10
C, 270.55, FWHM=10.1mm, $4 \times 4$ cm <sup>2</sup> field, 5 mm spacing, N=500088 (2E6 cm <sup>-2</sup> ), with ripple filter		11
C, 430.10, FWHM=9.8 mm $4 \times 4$ cm <sup>2</sup> field, 4 mm spacing, N=319976 (2E6 cm <sup>-2</sup> ), with ripple filter		12
C, 88.83, FWHM=9.8 mm, N=5.44E6, no ripple filter, 0 cm PMMA	Beam quality	
C, 178.01, FWHM=10.8 mm, N=5.44E6, no ripple filter, 4.3 cm PMMA		31
C, 301.00, FWHM=10.0 mm, N=5.44E6, no ripple filter, 13.1 cm PMMA		33
C, 359.58, FWHM=9.8 mm, N=5.44E6, no ripple filter, 18.2 cm PMMA		35
C, 430.10, FWHM=9.8 mm, N=5.44E6, no ripple filter, 24.8 cm PMMA		8
P, 48.12, FWHM=32.7 mm, N=8.99E6, no ripple filter, 0 cm PMMA	Beam quality	13
P, 95.30, FWHM=19.1 mm, N=8.99E6, no ripple filter, 4.3 cm PMMA		30
P, 157.96, FWHM=14.4 mm, N=8.99E6, no ripple filter, 13.1 cm PMMA		32
P, 186.95, FWHM=13.2 mm, N=8.99E6, no ripple filter, 18.2 cm PMMA		34

P, 221.06, FWHM=12.6 mm, N=8.99E6, no ripple filter, 24.8 cm PMMA		6
C, 430.10, FWHM=3.4 mm, N= 654926, 24.8 cm PMMA, no ripple filter, at 0, 6, 12, 18 mm lateral	Lateral profile	14, 15, 16, 17
C, 430.10, FWHM=3.4 mm, N= 6549260, 24.8 cm PMMA, no ripple filter, at 0, 6, 12, 18 mm lateral		18, 19, 20, 21
C, 430.10, FWHM=3.4 mm, N= 65492600, 24.8 cm PMMA, no ripple filter, at 0, 6, 12, 18 mm lateral		22, 23, 24, 25
C, 430.10, FWHM=3.4 mm, N=1E9, 24.8 cm PMMA, with PE foil, spot at (- 100mm,0)	Neutrons	26
C, 430.10, FWHM=3.4 mm, N=1E9, 24.8 cm PMMA, without PE foil, spot at (- 100mm,0)		27
C, 88.83, FWHM=9.8 mm, N=1E9, 0 cm PMMA, with PE foil, spot at (-100mm,0)		28
C, 88.83, FWHM=9.8 mm, N=1E9, 0 cm PMMA, without PE foil, spot at (- 100mm,0)		29



# Appendix B

## Lists

### B.1 List of Figures

1.1	Depth dose curve of a 270 MeV/u carbon ion beam (black), relative to the entrance dose. Contribution of the primary HCP is red, respectively blue for secondary fragments (Schardt 2009) . . . . .	1
2.1	Confocal setup after (Fischer 1996) . . . . .	12
2.2	Airy pattern, (Wikimedia Commons 2009) . . . . .	14
3.1	The FNTDs used in this thesis had dimensions of $4 \times 6 \text{ mm}^2$ and a thickness of .5 mm . . . . .	16
3.2	Illustration of the $F_2^{2+}(2\text{Mg})$ defect, (Sanyal and Akselrod 2005) . . .	18
3.3	Electron avenues in $\text{Al}_2\text{O}_3:\text{C,Mg}$ : Electrons can recombine with electron-holes, get captured by deep traps, $F_2^{2+}(2\text{Mg})$ , $F_2^+(2\text{Mg})$ or $F^+$ defects (from the left to the right), (Sykora and Akselrod 2010a) .	18
3.4	Photoluminescence emission / excitation spectra of the same $\text{Al}_2\text{O}_3:\text{C,Mg}$ crystal a) as-grown, b) thermally annealed for 17 h at 600 °C, c) optically bleached with 260 nm and 325 nm light and d) irradiated with 100 Gy of x-ray radiation, (Sykora and Akselrod 2010a) . . . . .	19
4.1	. . . . .	28
4.2	. . . . .	29
4.3	. . . . .	29
4.4	Fluorescent cleaning residues on the FNTD surface . . . . .	30
4.5	Dirt on the FNTD surface absorbs light . . . . .	31
4.6	Proton irradiated FNTD; $4 \times 4$ tiles, each with $103.81 \times 103.81 \text{ }\mu\text{m}^2$ , $512 \times 512$ pixels; the tile grid is visible in the discontinuous pattern which indicates a sensitivity variation of the microscope . . . . .	32
4.7	. . . . .	32
4.8	Average of 35 images obtained from an unirradiated FNTD; $103.81 \times 103.81 \text{ }\mu\text{m}^2$ , $512 \times 512$ pixels and 50.42 $\mu\text{s}$ dwell time . . . . .	33
4.9	Typical “dark” image from an unirradiated FNTD; $103.81 \times 103.81 \text{ }\mu\text{m}^2$ , $512 \times 512$ pixels and 50.42 $\mu\text{s}$ dwell time. The mean value is $102.6 \pm 13.9$ . . . . .	33

4.10	Fluorescence frequency distribution of Figure 4.9: how many pixels with a given signal are in the image . . . . .	34
4.11	Fit of a gaussian bell curve to the background signal . . . . .	34
4.12	Map of the relative background fluorescence . . . . .	34
4.13	Map of the relative track fluorescence . . . . .	34
4.14	Background peak depth profile of an unirradiated FNTD . . . . .	35
4.15	Depth profile at the FNTD surface for different pinhole sizes. . . . .	36
4.16	Histograms of a time series. From bottom to top: Histogram of the fluorescence of the pixel with the minimal average signal, histogram of the pixel with the maximal average signal, histogram of all images of the series and the histogram of the summed up and normalized image of the series . . . . .	37
4.17	Developement of the minimal and maximal pixels over time . . . . .	38
4.18	The root mean square pixel-wise difference of a standard carbon ion image and the interpolated background against the ball radius parameter in pixel . . . . .	39
4.19	Downsampled relative difference of relative interpolated and relative measured background for protons . . . . .	40
4.20	Downsampled relative difference of relative interpolated and relative measured background for carbon ions . . . . .	40
4.21	Relative background obtained from Fourier band pass filter with suspension of structures larger than a) 64 pixels, b) 100 pixels, c) 200 pixels, d) 256 pixels, e) 300 pixels or f) 400 pixels. Data is corresponding to Figure 4.12 . . . . .	41
4.22	Map of the signal variation, obtained by local fits to Gaussian curves . . . . .	42
4.23	Setup of the irradiation at the Siemens Gammatron S . . . . .	43
4.24	Setup of the irradiation at the Siemens Primus . . . . .	44
4.25	Gamma response corrected . . . . .	45
4.26	FNTD after gamma irradiation with a) 0.01 Gy, b) 0.03 Gy, c) 0.1 Gy, d) 0.3 Gy and e) 1 Gy from the Siemens Gammatron S and f) 3 Gy, g) 10 Gy and h) 20 Gy from the Siemens Primus . . . . .	46
4.27	FNTD irradiated with Beta-particles from a Sr/Y-90 source. Though hard to track because of the low LET and the curling trajectories, single electron pathways can be seen. . . . .	47
4.28	Alpha particles. Ellipsiodity of the tracks is due to the divergence of the particles. . . . .	48
4.29	Non-colinearity of alpha particles emitted from a finite source in 3d view of an image stack . . . . .	48
4.30	Setup for the imaging of grazing carbon ion tracks . . . . .	49
4.31	a) Image of a stopping carbon ion. b) Maximum projected image stack of 52 slices over 12.48 $\mu\text{m}$ of the same stopping carbon ion . . . . .	50
4.32	270 MeV/u carbon ion fragmentation. Also, $\delta$ -electrons are clearly visible. Image is a maximum projected stack of 13 slices, $67.48 \times 67.48 \mu\text{m}^2$ . . . . .	51



4.33	52
4.34 142 MeV protons	52
4.35 FNTDs attached to a holding device for irradiation with antiprotons	53
4.36 127 MeV antiprotons. Stray shots from pions can be seen. Pions are produced both in the Bragg peak and—to less extend—in in-flight annihilations. Standard microscope settings.	54
4.37 Image of antiproton tracks in the Bragg peak. In comparison to the entrance channel, the abundance of stray shots is increased.	54
4.38 Antiproton annihilation event	56
4.39	56
4.40	57
4.41 Tracks of the particle spectrum of a 430 MeV/u carbon ion beam after traversal of 24.8 cm PMMA for different lateral distances from the beam axis. FWHM of the beam was 3.4 mm. Standard microscope settings.	58
4.42 Carbon ion track, 270 MeV/u, average from 60 tracks	59
4.43 Radial fluorescence signal obtained from the data of Figure 4.42. For comparison, a Geiss model 270 MeV/u carbon ion track with $r_{core} = 50$ nm is displayed. The datapoint from $r = 0$ is put to a quarter of the pixel size, i.e. half the distance from the middle to the boundary of the $r = 0$ pixel.	59
4.44 Setup of the fluence measurement. FNTD attached by adhesive tape to a PMMA plate.	60
4.45 Fluorescence frequency distribution. Images background corrected.	63
4.46 142.66 MeV proton tracks, $103.81 \times 103.81 \mu\text{m}^2$	63
4.47 Background signal distribution of Figure 4.46	63
4.48 270.55 MeV/u carbon ion tracks, $103.81 \times 103.81 \mu\text{m}^2$	64
4.49 Background signal distribution of Figure 4.48	64
4.50 0.7 MeV/u alpha particle tracks, $103.81 \times 103.81 \mu\text{m}^2$	64
4.51 Background signal distribution of Figure 4.50	64
4.52 Fluorescence frequency distribution of background corrected 142 MeV protons, 270 MeV/u carbon ions, 1.4 MeV alpha particles, bin width of 5 counts	65
4.53 Fluence normalized fluorescence frequency distribution of background corrected 142 MeV protons, 270 MeV/u carbon ions, 1.4 MeV alpha particles, bin width of 5 counts	65
5.1 Human prostate carcinoma cells grown on a FNTD, imaged through a light microscope. Courtesy of Martin Niklas.	73

## B.2 List of Tables

3.1 Excitation/emission bands of $\text{Al}_2\text{O}_3\text{:C,Mg}$	17
--	----

4.1	Sources and relevance of signal variations . . . . .	27
4.2	Fluence measurements. Measured number of local maxima vs. the number of tracks expected from the accelerator input $\pm$ the poisson error and the deviation of the measurement in relation to the expectation. . . . .	61
4.3	Off-beam measurement. 430.10 MeV/u carbon ions sent through 24.8 cm PMMA and 88.83 MeV/u carbon ions free in air. The automatically counted fluorescence maxima are listed for different <i>noise tolerance</i> (nt) parameter settings of the counting routine. . . . .	66

# Appendix C

## Bibliography

libamtrack project. <http://libamtrack.dkfz.org/>. 3.1.3

M. D. Abramoff, P. J. Magelhaes, and S. J. Ram. Image processing with ImageJ. *Biophotonics Int*, 11(7):36–42, 2004. 3.4, 4.3.3

Lewis E. Agnew, Tom Elioff, William B. Fowler, Richard L. Lander, Wilson M. Powell, Emilio Segrè, Herbert M. Steiner, Howard S. White, Clyde Wiegand, and Tom Ypsilantis. Antiproton interactions in hydrogen and carbon below 200 MeV. *Phys. Rev.*, 118(5):1371–1391, Jun 1960. doi: 10.1103/PhysRev.118.1371. 2.1.5

Steven P. Ahlen. Theoretical and experimental aspects of the energy loss of relativistic heavily ionizing particles. *Review of Modern Physics*, 52(1):121–173, Jan 1980. doi: 10.1103/RevModPhys.52.121. 2.1.3

G. M. Akselrod, M. S. Akselrod, E. R. Benton, and N. Yasuda. A novel Al<sub>2</sub>O<sub>3</sub> fluorescent nuclear track detector for heavy charged particles and neutrons. *Nuclear Instruments and Methods in Physics Research B*, 247:295–306, 2006a. 1, 3.1, 5.1, 5.4, 5.7

M. S. Akselrod and A. E. Akselrod. New Al<sub>2</sub>O<sub>3</sub>:C,Mg crystals for radiophotoluminescent dosimetry and optical imaging. *Radiation Protection Dosimetry*, 119: 218–221, 2006. 1, 3.1.3, 5.1

M. S. Akselrod, A. C. Lucas, J. C. Polf, and S. W. S. McKeever. Optically stimulated luminescence of Al<sub>2</sub>O<sub>3</sub>:C. *Radiation Measurements*, 29:391–399, 1998. 1

M. S. Akselrod, A. E. Akselrod, S. S. Orlov, S. Sanyal, and T. H. Underwood. Fluorescent aluminum oxide crystals for volumetric optical data storage and imaging applications. *Journal of Fluorescence*, 13:503–511, 2003. 1, 3.1, 5.1

M. S. Akselrod, R. C. Yoder, and G. M. Akselrod. Confocal fluorescent imaging of tracks from heavy charged particles utilising new Al<sub>2</sub>O<sub>3</sub>:C,Mg crystals. *Radiation Protection Dosimetry*, 119:357–362, 2006b. 5.1

H. Arendt and J. Hullinger, editors. *Crystal Growth in Science and Technology*. Plenum, New York, 1989. 3.1.1

- Frank Herbert Attix. *Introduction to radiological physics and radiation dosimetry*. John Wiley & Sons, New York, 1986. 2.1.3
- S. A. Baird, D. Berlin, J. Boillot, Jacques. Bosser, M. Brouet, J. Buttkus, Friedhelm Caspers, V. Chohan, Daniel Dekkers, T. Eriksson, R. Garoby, R. Gianini, Oswald Gröbner, J. Gruber, J. Y. Hémery, Heribert Koziol, R. MacCaferri, S. Maury, C. Metzger, K. D. Metzmacher, D. Möhl, H. Mulder, M. Paoluzzi, F. Pedersen, J. P. Riunaud, C. Serre, Daniel Jean Simon, G. Tranquille, Jan Willem Nicolaas Tuyn, and B. Williams. Design study of the antiproton decelerator: AD, 1997. URL <http://preprints.cern.ch/cgi-bin/setlink?base=preprint&categ=cern&id=PS-96-043>. 3.2.6
- W. H. Barkas and M. J. Berger. Studies in penetration of charged particles in matter. *National Academy of Sciences—National Research Council Publication No. 1133*, Nuclear Science Series Report 39, 1964. 2.1.3
- N. Bassler, M. H. Holzscheiter, H. Knudsen, and the AD4/ACE Collaboration. Cancer therapy with antiprotons. In Grzonka, D. et al., editor, *Low Energy Antiproton Physics—LEAP '05*, volume CP796 of *AIP Conference Proceedings*, pages 423–430. American Institute of Physics, 2005. 2.1.5
- E. V. Benton. A study of charged particle tracks in cellulose nitrate. Technical report, U.S. Navel Radiological Defense Laboratory TR-68-14, 1968. 1
- M. J. Berger, J. S. Coursey, M. A. Zucker, and J. Chang. Stopping-power and range tables for electrons, protons, and helium ions. URL <http://physics.nist.gov/PhysRefData/Star/Text/PSTAR.html>. 2.1.3
- H. Bethe. Zur Theorie des Durchgangs schneller Korpuskularstrahlen durch Materie. *Annalen der Physik*, 397:325–400, 1930. 2.1.3
- H. Bethe. Bremsformel für Elektronen relativistischer Geschwindigkeit. *Zeitschrift für Physik A Hadrons and Nuclei*, 76:293–299, 1932. ISSN 0939-7922. URL <http://dx.doi.org/10.1007/BF01342532>. 10.1007/BF01342532. 2.1.3
- N. Bohr. The penetration of atomic particles through matter. *Philosophical Magazine*, 6:518, 1915. 2.1.3
- T. Bortfeld. An analytical approximation of the bragg curve for therapeutic proton beams. *Medical Physics*, 24:2024–2033, 1997. 2.1.3, 4.6.1
- L. Bøtter-Jensen, S. W. S. McKeever, and A. G. Wintle. *Optically stimulated luminescence dosimetry*. Elsevier science B. V, 2003. 3.1
- J. D. Bowman, W. J. Swiatecki, and C.F Tsang. Abrasion and ablation of heavy ions. National Laboratory: Lawrence Berkeley National Laboratory LBNL Paper LBL-2908, 1973. 2.1.5

- Bundesamt für Strahlenschutz. Umweltradioaktivität und Strahlenbelastung. Jahresbericht 2008. Das Bundesministerium für Umwelt, Naturschutz und Reaktorsicherheit, Postfach 12 06 29, 53048 Bonn, December 2009. URL [http://www.bfs.de/de/bfs/druck/uus/JB\\_archiv.html/#2008](http://www.bfs.de/de/bfs/druck/uus/JB_archiv.html/#2008). 4.2.5
- Operating Manual LSM 710 and Confocor 3*. Carl Zeiss MicroImaging GmbH, 07740 Jena, Germany, 10 2008. 2.2, 3.3.1
- B.G. Cartwright, E.K. Shirk, and P.B. Price. A nuclear-track-recording polymer of unique sensitivity and resolution. *Nuclear Instruments and Methods*, 153(2-3):457 – 460, 1978. ISSN 0029-554X. doi: DOI:10.1016/0029-554X(78)90989-8. URL <http://www.sciencedirect.com/science/article/B73DN-473D859-W/2/983d59b6fbd736abcbfd5e4b81ee5170>. 1
- W. T. Chu, B. A. Ludewigt, and T. R. Renner. Instrumentation for treatment of cancer using proton and light-ion beams. *Review of Scientific Instruments*, 64: 2055–2122, 1993. 2.1.3
- J. Cugnon, S. Wycech, J. Jastrzębski, and P. Lubiński. Geometrical effects in antiproton annihilation on nuclei. *Physical Review C*, 63(2):027301–+, February 2001. doi: 10.1103/PhysRevC.63.027301. 2.1.5
- A. P. Fews and D. L. Henshaw. High resolution alpha particle spectroscopy using cr-39 plastic track detector. *Nuclear Instruments and Methods*, 197:517–529, 1982. 1
- S. K. Fischer. *Entwicklung eines konfokalen Laserscanning-Mikroskops zum Einsatz in der stereotaktischen Laser-Neurochirurgie*. PhD thesis, University of Heidelberg, 1996. 2.1, B.1
- R. L. Fleischer, P. B. Price, and R. M. Walker. Solid-state track detectors: applications to nuclear science and geophysics. *Annual Review of Nuclear Science*, 15: 1–28, 1965. 1
- L. Gray and T.E. Kalogeropoulos. Possible biomedical applications of antiproton beams: Focused radiation transfer. *Radiation Research*, 97:246–252, 1984. 2.1.5
- S. Greulich, H.-L. Harney, C. Wodaa, and G. A. Wagner. Agesgalore—a software program for evaluating spatially resolved luminescence data. *Radiation Measurements*, 41:726–735, 2006. 5.2.3
- K. Gunzert-Marx. *Nachweis leichter Fragmente aus Schwerionenreaktionen mit einem BaF<sub>2</sub>-Teleskop-Detektor*. PhD thesis, Technical University Darmstadt, 2004. 2.1.5
- K. Gunzert-Marx, D. Schardt, and R. S. Simon. The fast neutron component in treatment irradiations with <sup>12</sup>C beam. *Radiotherapy and Oncology*, 73 Supplement 2:S92–S95, 2004. 1

- T. Haberer, W. Becher, D. Schardt, and Kraft G. Magnetic scanning system for heavy ion therapy. *Nuclear Instruments and Methods in Physics Research A*, 330: 296–305, 1993. [3.2.5](#)
- E. Haettner. Experimental study on carbon ion fragmentation in water using gsi therapy beams. Master’s thesis, Technical University Darmstadt, 2006. [1](#)
- M. H. Holzscheiter, Jan Alsner, Angelo Angelopoulos, Niels Bassler, Gerd Beyer, Fred Currell, John De Marco, Michael Doser, Dragan Hajdukovic, Oliver Hartley, Joy Kavanagh, Kei Iwamoto, Oliver Jäkel, Ioannis Kantemiris, Helge Knudsen, Sandra Kovacevic, Bill McBride, Søren Pape Møller, Jens Overgaard, Jørgen Petersen, Osman Ratib, Giuseppe Schettino, David Timson, Brita Singers-Sørensen, Timothy Solberg, Sanja Vranjes, and Brad Wouters. Status report for experiment ad-4/ace biological effectiveness of antiproton annihilation. Technical Report CERN-SPSC-2009-002. SPSC-SR-039, CERN, Geneva, Jan 2009. [2.1.5](#)
- IAEA. Relative biological effectiveness in ion beam therapy. Technical Report 461, International Atomic Energy Agency, 2008. [2.1.6](#)
- ICRU. Linear energy transfer. Technical Report 16, International Commission on Radiation Units and Measurements, ICRU, 7910 Woodmont Avenue, Bethesda, Maryland 20814, USA, June 1970. [2.1.4](#), [3.2.3](#)
- ICRU. Stopping Powers and Ranges for Protons and Alpha Particles. Technical Report 49, International Commission on Radiation Units and Measurements, ICRU, 7910 Woodmont Avenue, Bethesda, Maryland 20814, USA, 1993. [2.1.3](#)
- ICRU. Fundamental quantities and units for ionizing radiation. Technical Report 60, International Commission on Radiation Units and Measurements, ICRU, 7910 Woodmont Avenue, Bethesda, Maryland 20814, USA, December 1998. [2.1.2](#), [2.1.3](#)
- ICRU. Prescribing, Recording, and Reporting Proton-Beam Therapy. Technical Report 49, International Commission on Radiation Units and Measurements, ICRU, 7910 Woodmont Avenue, Bethesda, Maryland 20814, USA, 2007. [2.1.6](#)
- J. Kiefer and H. Straaten. A model of ion track structure based on classical collision dynamics. *Physics in Medicine and Biology*, 31:1201–1209, 1986. [2.1.6](#)
- D. E. Lea. *Actions of Radiations on living Cells*. Cambridge University Press, London, 1946. [2.1.6](#)
- W. Markiel, H. Daniel, T. von Egidy, F. J. Hartmann, P. Hofmann, W. Kanert, H. S. Plendl, K. Ziöck, R. Marshall, H. Machner, G. Riepe, and J. J. Reidy. Emission of helium ions after antiproton annihilation in nuclei. *Nuclear Physics A*, 485: 445–460, August 1988. doi: 10.1016/0375-9474(88)90547-7. [2.1.5](#)

- Inokuti Mitio. Interactions of antiprotons with atoms and molecules. *International Journal of Radiation Applications and Instrumentation. Part D. Nuclear Tracks and Radiation Measurements*, 16(2-3):115 – 123, 1989. ISSN 1359-0189. doi: DOI:10.1016/1359-0189(89)90042-3. URL <http://www.sciencedirect.com/science/article/B6X49-479D7Y1-1B/2/371810a83a7d4802738e43d29630f980>. 2.1.5
- G. Molière. Theorie der streuung schneller geladener teilchen ii. *Zeitschrift für Naturforschung*, 3a:78–97, 1948. 2.1.3
- Nakamura K. et al. (Particle Data Group). Review of particle physics. *Journal of Physics G*, 37:075021, 2010. 2.1.5
- D. Polster, D. Hilscher, H. Rossner, T. von Egidy, F. J. Hartmann, J. Hoffmann, W. Schmid, I. A. Pshenichnov, A. S. Iljinov, Ye. S. Golubeva, H. Machner, H. S. Plendl, A. Grochulska, J. Jastrzebski, W. Kurcewicz, P. Lubinski, J. Eades, and S. Neumaier. Light particle emission induced by stopped antiprotons in nuclei: Energy dissipation and neutron-to-proton ratio. *Phys. Rev. C*, 51(3):1167–1180, Mar 1995. doi: 10.1103/PhysRevC.51.1167. 2.1.5
- L. I. Ponomarev. Molecular structure effects on atomic and nuclear capture of mesons. *Annual Review of Nuclear Science*, 23:395–430, 1973. 2.1.5
- R Development Core Team. *R: A Language and Environment for Statistical Computing*. R Foundation for Statistical Computing, Vienna, Austria, 2010. URL <http://www.R-project.org>. ISBN 3-900051-07-0. 3.4
- W. S. Rasband. <http://rsb.info.nih.gov/ij/>, 1997-2009. URL <http://rsb.info.nih.gov/ij/>. 3.4, 4.3.3
- E. Rittweger, K. Y. Han, S. E. Irvine, C. Eggeling, and S. W. Hell. STED microscopy reveals crystal colour centres with nanometric resolution. *nature photonics*, 3:144–147, 2009. 5.6
- S. Sanyal and M. S. Akselrod. Anisotropy of optical absorption and fluorescence in Al<sub>2</sub>O<sub>3</sub>:C,Mg crystals. *Journal of Applied Physics*, 98:033518–1 – 033518–12, 2005. 3.1.1, 3.2, 5.1, B.1
- Deepayan Sarkar. *Lattice: Multivariate Data Visualization with R*. Springer, New York, 2008. URL <http://lmdvr.r-forge.r-project.org>. ISBN 978-0-387-75968-5. 3.4
- D. Schardt. Physical characterization of ion beams for tumor therapy. NUFRA2009 International Conference on Nuclear Fragmentation, 2009. URL <http://fias.uni-frankfurt.de/historical/nufra2009/talks/schardt.pdf>. 1.1, B.1
- W. Schlegel and J. Bille, editors. *Medizinische Physik*, volume 2. Springer, Berlin Heidelberg, 2002. 2.1.4, 3.2.2

- S. R. Sternberg. Biomedical image processing. *Computer*, 16:22–34, 1983. ISSN 0018-9162. doi: <http://doi.ieeeecomputersociety.org/10.1109/MC.1983.1654163>. [4.3.3](#)
- A. H. Sullivan. A measurement of the local energy deposition by antiprotons coming to rest in tissue-like material. *Physics in Medicine and Biology*, 30:1297, 1985. [2.1.5](#)
- G. J. Sykora and M. S. Akselrod. Photoluminescence study of photochromically and radiochromically transformed  $\text{Al}_2\text{O}_3\text{:C,Mg}$  crystals used for fluorescent nuclear track detectors. *Radiation Measurements*, 45:631–634, 2010a. [3.1.4](#), [3.3](#), [3.4](#), [B.1](#)
- G. J. Sykora, M. S. Akselrod, M. Salasky, and S. A. Marino. Novel  $\text{Al}_2\text{O}_3\text{:C,Mg}$  fluorescent nuclear track detectors for use in passive neutron dosimetry. *Radiation Protection Dosimetry*, 126:278–283, 2007. [4.10.1](#), [5.1](#)
- G. J. Sykora, M. S. Akselrod, E. R. Benton, and N. Yasuda. Spectroscopic properties of novel fluorescent nuclear track detectors for high and low LET charged particles. *Radiation Measurements*, 43:422–426, 2008a. [5.1](#)
- G. J. Sykora, M. Salasky, and M. S. Akselrod. Properties of novel fluorescent nuclear track detectors for use in passive neutron dosimetry. *Radiation Measurements*, 43:1017–1023, 2008b. [1](#), [4.10.1](#), [5.1](#)
- Garrett J. Sykora and Mark S. Akselrod. Spatial frequency analysis of fluorescent nuclear track detectors irradiated in mixed neutron-photon fields. *Radiation Measurements*, 45(10):1197 – 1200, 2010b. ISSN 1350-4487. doi: DOI:10.1016/j.radmeas.2010.08.022. URL <http://www.sciencedirect.com/science/article/B6TVS-50X2NNX-1/2/07b469743dc6f72f78ace50113a2e97a>. PROCEEDINGS OF THE 11TH SYMPOSIUM ON NEUTRON AND ION DOSIMETRY, iThemba Laboratory for Accelerator-Based Sciences. [5.1](#), [5.3](#)
- Y.-S. Tsai. Pair production and bremsstrahlung of charged leptons. *Review of Modern Physics*, 46:815, 1974. [2.1.3](#)
- M. N. Varma, J. W. Baum, and A. V. Kuehner. Radial Dose, LET, and W for O-16 Ions in N<sub>2</sub> and Tissue-equivalent Gases. *Radiation Research*, 70:511–518, 1977. [2.1.6](#)
- U. Weber. *Volumenkonforme Bestrahlung mit Kohlenstoff-Ionen zur Vorbereitung einer Strahlentherapie*. PhD thesis, University of Kassel, 1996. [3.2.5](#)
- Wikimedia Commons. File:airy pattern.svg, 2009. URL [http://commons.wikimedia.org/w/index.php?title=File:Airy\\_Pattern.svg&oldid=18922188](http://commons.wikimedia.org/w/index.php?title=File:Airy_Pattern.svg&oldid=18922188). [Online; accessed 8-February-2011]. [2.2](#), [B.1](#)



Erklärung:

Ich versichere, dass ich diese Arbeit selbstständig verfasst habe und keine anderen als die angegebenen Quellen und Hilfsmittel benutzt habe.

Heidelberg, den 28. Februar 2011

.....



# Acknowledgments

I would like express my gratitude to Prof. Dr. Wolfgang Schlegel, head of medical physics in radiation oncology at the german cancer research center (DKFZ) for giving me the opportunity to work in his department.

For accepting me in the Heavy Ion Project and for his style in administrating and supervising the group, I want to thank Prof. Dr. Oliver Jäkel. I also want to thank Prof. Dr. Uwe Oelfke for being my second referee and for his lectures at the university that brought me to medical physics.

I want to thank Mark Akselrod, PhD and James Bartz from Landauer, Inc. for their confidence in me and the endowment of the detectors.

Furthermore I am happy about this opportunity to give my special thanks to Dr. Steffen Greulich for his ongoing support and the fruitful discussions. To the whole E0409, I am thankful for the inspiring atmosphere and the time spent at the dosatron.

Without the DKFZ light microscopy facility my work would not be possible, I am indebted to Dr. Felix Bestvater and Manuela Brom for their help.

Thanks goes to Dr. Michael Holzscheiter for his help at CERN. The support of Dr. Stephan Brons and Benjamin Ackermann with the irradiations at HIT is gratefully appreciated. I also thank Dr. Annette Kadereit from the luminescence lab of the department of geography of the University of Heidelberg for the possibility to use their alpha and beta sources.

Last but not least, I thank my family for their support and especially my parents and my sister for providing me the childhood I had.